Diss. ETH No. 26054

Novel Methods and Instrumentation for Scientifically Sound Assessment of MR Safety of Medical Implants

A dissertation submitted to the
ETH ZURICH

for the degree of
DOCTOR OF SCIENCES
(Dr. sc. ETH Zurich)

presented by
AIPING YAO
Master of Science, Chinese Academy of Science
born August 20, 1988
citizen of China

accepted on the recommendation of
Prof. Dr. Q. Huang, examiner
Prof. Dr. N. Kuster, Prof. Dr. T. Samaras , co-examiners

2019

-- 致我最亲爱的父母
和我深爱的那片黄土地

Contents

Summary **xiii**

Zusammenfassung **xvii**

Acknowledgments **xxiii**

I Introduction 1

1 Background, Motivation, and Objectives **3**
- 1.1 Background 3
  - 1.1.1 MRI Safety in the Absence of Implants 4
  - 1.1.2 MRI Safety with Implants Present 5
  - 1.1.3 RF Safety Assessment of AIMDs 9
- 1.2 Motivation 11
- 1.3 Objectives 13
- 1.4 Synopsis 13

2 Practical Considerations in Experimental Evaluations of RF-induced Heating of Leaded Implants **17**
- 2.1 Abstract 17
- 2.2 Introduction 18
- 2.3 Experimental Characterization of Implant RF-induced Heating 18
- 2.4 Experimental Radiated Testing of Implant RF-induced Heating 24
- 2.5 Summary 26

II Review of State-of-Knowledge 29

3 Electromagnetic MRI Safety with and without Implantable Metallic Devices: A Review 31
3.1 Abstract 31
3.2 Introduction 32
3.3 Standardization 33
3.4 Analysis of the PIMD/AIMD Environment 35
  3.4.1 The Static Magnetic Field (B_0) 36
  3.4.2 The Gradient Field (G) 36
  3.4.3 Radio Frequency Fields B_1 37
3.5 Brief Review of Risks without PIMD/AIMD 42
3.6 Review of Risks with PIMD/AIMD 45
  3.6.1 Mechanical Risks 45
  3.6.2 Risks Due to AIMD Malfunctions 46
  3.6.3 Risks Due to Thermal Effects 46
  3.6.4 Risks Due to Image Distortion 47
3.7 Discussion and Conclusions 48

III *in vitro* Experimental Methods 51

4 Novel Test Field Diversity Method for RF Transfer Function Validation Required for Demonstrating MRI Safety of Active Implantable Medical Devices 53
4.1 Abstract 53
4.2 Introduction 54
4.3 Methods 57
  4.3.1 Polarization Ellipse 57
  4.3.2 Incident Condition Definition 57
  4.3.3 Exposure Systems 59
  4.3.4 Tier 3 RF Transfer Function 60
  4.3.5 RF-Heating Derived from the AIMD Transfer Function 61
  4.3.6 RF-heating Measured from TFD Experiments 62
4.4 Results 63
4.5 Discussion 69
4.6 Conclusion 73

5 **Data-driven Experimental Evaluation Method for the Safety Assessment of Implants with Respect to RF-induced Heating During MRI** **75**
5.1 Abstract 75
5.2 Introduction 76
5.3 Motivation 77
5.4 Proposed Method 79
    5.4.1 Exposure Definition 79
    5.4.2 Data Acquisition 80
    5.4.3 Post-processing 82
5.5 Results 83
5.6 Conclusion 87

IV *in vivo* Human-RF Interaction Evaluation **91**

6 **Anatomical Model Uncertainty for RF Safety Evaluation of AIMD Under MRI Exposure** **93**
6.1 Abstract 93
6.2 Introduction 94
6.3 Method 95
    6.3.1 Anatomical Phantoms 95
    6.3.2 Simulation of the MRI Environment 96
    6.3.3 Evaluation 96
6.4 Results 101
    6.4.1 Anatomical Comparison 101
    6.4.2 Tier 1 and Tier 2 Evaluations 104
    6.4.3 Tier 3 Evaluation 105
    6.4.4 Tier 4 evaluation 112
    6.4.5 Discussions 112
    6.4.6 Conclusions 116

7 **Standardized, Validated and Effective Safety Assessment of Patients with Medical Implants under MRI Exposure Using A Comprehensive Data Library Combined with an Analytics Toolset** **119**
7.1 Abstract 120
7.2 Introduction 121
7.3 Methods 121

7.4 Results 124
7.5 Conclusions 125

V Determination of the *in vivo* Temperature Increase 129

8 Efficient and Reliable Assessment of the Maximum Local Tissue Temperature Increase at the Electrodes of Medical Implants under MRI Exposure 131

8.1 Abstract 131
8.2 Introduction 132
8.3 Method 134
  8.3.1 Deposited power-to-ΔT ($P2\Delta T$) factor 134
  8.3.2 Simulations 134
8.4 Parameter Study 135
  8.4.1 AIMD Modeling 136
  8.4.2 Piecewise Varying Tissue Distribution Modeling Along AIMD 138
  8.4.3 Electrode Embedded in Locally Spatially Inhomogeneous Tissues 138
  8.4.4 Validation in Detailed Anatomical Models in Clinically Relevant Scenarios 138
8.5 Results 140
  8.5.1 AIMD Modeling 140
  8.5.2 Tissue Distribution Simplification 143
  8.5.3 Electrode Embedded in Locally Spatially Inhomogeneous Tissues 145
  8.5.4 Validation in Anatomical Models 145
8.6 Discussion and Conclusions 146

VI Epilogue 151

9 Conclusions and Outlook on Related Future Research Topics 153

9.1 Outlook 155

VII Appendix 159

A Supporting Information of Chapter 4 161
- A.1 Overview 161
- A.2 TFD expsure 161
  - A.2.1 Experimental Setup 162
  - A.2.2 Numerical Modeling 162
- A.3 Local Enhancement Evaluation 163
  - A.3.1 Data acquisition system 163
  - A.3.2 Post-processing 163
- A.4 Tier 3 model 163

B Supporting Information of Chapter 5 165
- B.1 Overview 165
- B.2 Uncertainty Components of Table 5.1 165
  - B.2.1 Exposure Drift 166
  - B.2.2 Phantom 166
  - B.2.3 TSM 166
  - B.2.4 Data Acquisition 166
  - B.2.5 Truncated Boundary 166
  - B.2.6 Field Sensor Position 167
  - B.2.7 SAR_{HR} 167
  - B.2.8 Power Calculation 167
  - B.2.9 Co-registration 168

C List of Acronyms 169

D List of Symbols 171

E List of Publications 173
- E.1 Journal Publications 173
- E.2 Other Publications 174

Bibliography 193

Curriculum Vitae 213

Summary

Magnetic resonance imaging (MRI) is a medical diagnostic technique that produces detailed high-quality images of the anatomy with excellent soft tissue contrast. Further, functional MRI (fMRI) has emerged in recent years as another important diagnostic tool with large potential for assessing brain activity by measuring changes in blood flow. MRI scanners use strong static magnetic fields, magnetic field gradients, and radiofrequency (RF) fields to generate images of tissues and organs in the body. As these fields interact with human body, they pose a potential safety hazard to the patients.

Among the recognized safety hazards of MRI, radiofrequency (RF) induced tissue heating in the presence of conductive implants is the most publicized risk. Serious safety issues (e.g., irreparable tissue damage, implant device mulfunction) due to excessive heating are possible. Hence, patients with implants – in particular active implantable medical devices (AIMDs), such as cardiac pacemakers or deep brain stimulators (DBS) – are ineligible for MRI diagnostic procedures due to safety concerns related to possible interactions between the implant devices and the electromagnetic fields (EMF) generated during MRI. As a consequence, patients with medical implants can not benefit from MRI diagnostics, unless the AIMD has been shown to be ‘MRI Safe’ or has received ‘MRI conditional’ labeling.

The first technical specification, ISO/TS 10974, developed by a joint working group of the International Standard Organization /International Electrotechnical Commission (ISO/IEC)[1] describes preliminary procedures for the assessment of safety hazards, including those caused by RF-implant interaction. However, the specification has several gaps that need to be addressed before it can become an ISO/IEC standard. These include the following RF-related issues:

- to lower the uncertainty budget of the implant RF-heating model, highly accurate experimental methods and instrumentation with well-controlled exposure conditions need to be developed
- to minimize patient risk while avoiding overly restricted and conservative imaging conditions that misses vital diagnostic information, a comprehensive evaluation procedure for *in vivo* RF-human interaction need to be identified that takes various realistic clinical scenarios into consideration
- for the determination of the *in vivo* temperature increase, reliable and practical assessment methods should be developed. Tissue-specific thermogenic damage threshold values need to be provided in addition to guidance on how to evaluate application-specific risk factors for the determined *in vivo* temperature increase.
- the test methods described in the technical specification are primarily designed and intended to address risks related to 1.5 Tesla MRI scanners; practical considerations and limitations related to higher field-strength, in particular 3.0 Tesla, need to be addressed as well

The goal of this thesis is to close some of these major gaps. Chapter 2 provides an overview of the engineering issues in determining the coupling of the AIMD with the RF fields of the MRI that had not been solved prior to the start of this thesis. The review of the current state of knowledge of MRI safety is presented in Part II. The complex and hostile electromagnetic MRI environment causes a variety of potential adverse interactions of the implants with the EMF of the scanner, especially due to enhanced RF absorption around the implant, which is difficult to quantify and is poorly understood due to its complexity. To gain a better insight into the implant exposure environment, Chapter 3 not only provides a comprehensive review of the current knowledge about MRI safety, including up-to-date mechanisms responsible for the potential MRI safety of patients with and without implants, it also gain a full picture of the implant exposure environment by investigating the influence of potential clinical factors (e.g., patient anatomical features, imaging positions, exposure conditions) have on the implant RF exposure environment.

In vitro experimental methods to enable better and easier characterization of implant models are described in Part III. To demonstrate safety of an AMID during MRI, a numerical model of the implant's RF response is required. The model must be validated under a sufficient number of incident tangential electrical (E-) field conditions that span the entire range of *in vivo* exposures. In the past, such investigations have been very time consuming and have often resulted in limited exposure conditions for long AIMDs. The amplitude and phase of the tangential E-field along a lead path in a cylindrical phantom can be sufficiently varied by changing the polarization of the incident magnetic field of the RF birdcage coil. This allows the introduction of a novel test field diversity (TFD) method that provides well-defined diverse exposure conditions and yields an efficient and reliable validation of the AIMD model with low uncertainty. The TFD method is discussed in detail in Chapter 4. The proposed TFD method can be applied to evaluations with both 1.5 Tesla and 3.0 Tesla scanners. The steep spatial gradient (5 – 10 dB/mm) of the induced specific absorption rate (SAR) near the implant electrode poses a serious challenge in correct positioning of the sensor during the measurement of near-field SAR near the implant electrode; even a deviation of only 0.2 mm can result in an uncertainty of more than 2 dB. To lessen the strict positioning requirements for accurate near-field measurement and to reduce the uncertainties related to the *in vitro* experimental setup, an experimental evaluation method based on image co-registration algorithms is outlined in Chapter 5. The proposed method is successfully validated against a variety of implants, exposure levels, and data acquisition procedures. The uncertainty associated with the proposed method applied to estimation of implant power deposition is less than 1 dB; a large reduction from the 2 dB found for traditional methods.

Issues related to the evaluation of *in vivo* RF-human interaction are addressed in Part IV. Anatomical human phantoms of the Virtual Population (ViP) have been used for many years as a key component of realistic dosimetry studies. However, the uncertainties associated with population sampling and segmentation are difficult to quantify, and a benchmark has not yet been established. The objective of Chapter 6 is to establish, for the first time, uncertainties of *in vivo* RF induced fields during MRI associated with tissue assignment, segmentation quality, and consistency of the digital human phantoms. By evaluating the differences between two generations of the ViP phantoms – ViP 1.x vs. ViP 3.0 covering a targeted patient population – the anatomical uncertainty associated with tissue assignment and segmentation quality/consistency established for AIMD-heating is shown to be 0.6 dB. The RF-induced implant heating is a complex function of multiple factors, including, e.g., the MRI system, patient anatomy, imaging position, exposure conditions, etc., therefore, a comprehensive safety assessment cannot be derived from only a limited number of clinical scenarios. In Chapter 7, an *in silico* safety assessment trial that combines a data library with a data analytics toolset has been established for use in performing comprehensive evaluations in a timely and traceable manner. The established workflow provides not only relevant but also comprehensive, consistent, extendable, and traceable results that facilitate the establishment of a corroborated knowledge base built upon existing and emerging data. It also facilitates the exploratory analysis of data for identification of exposure conditions that maximize both image quality and patient safety.

Issues related to the determination of *in vivo* temperature increase are addressed in Part V. AIMD safety evaluation requires the assessment of RF-induced thermal hazards for exposed patients. Due to the complicated *in vivo* human anatomical features and the multi-scale structures – meters for the human body vs. millimeters for the AIMD structure – involved in the clinical scenarios, the determination of *in vivo* temperature increase is extremely time consuming and computationally expensive. In Chapter 8, we investigate the modeling features required for efficient and reliable conversion of locally deposited RF power at the AIMD electrode to the *in vivo* maximum local tissue temperature increase ($P2\Delta T$). The modeling requirements and the associated uncertainties are determined by parameter studies of different implant models, incident field conditions, electrode configurations, and tissue models. With the derived AIMD and tissue model simplifications, very simplified models of the leads under uniform exposure can be used to assess $P2\Delta T$, while the surrounding tissues need to be modeled in detail. With the proposed simplifications, the assessment effort of $P2\Delta T$is reduced by a factor of more than 10 times.

In summary, the work performed in this thesis improves and simplifies MRI safety assessment of medical implants through novel methods and models with well-controlled uncertainties under various clinical scenarios. It also provides essential information for bridging some of the identified knowledge gaps in the current safety guidelines for exposure of implants to RF fields in MRI.

Zusammenfassung

Die Magnetresonanztomographie (MRI) ist eine medizinische Diagnosemethode, die detaillierte und qualitativ hochwertige Bilder der Anatomie mit exzellentem Weichgewebekontrast liefert. In den letzten Jahren hat sich darüber hinaus das funktionelle MRI (fMRI), welches die Veränderungen des Blutflusses misst, zu einem wichtigen diagnostischen Instrument mit grossem Potenzial für die Beurteilung von Hirnaktivität entwickelt. MRT-Scanner verwenden starke statische Magnetfelder, Magnetfeldgradienten und Radiofrequenzen (RF), um Bilder von Geweben und Organen im Körper zu erzeugen. Da diese Felder mit dem menschlichen Körper interagieren, stellen sie ein potenzielles Sicherheitsrisiko für Patienten dar.

Hinsichtlich der anerkannten Sicherheitsrisiken des MRI zählt die durch RF hervorgerufene Gewebeerwärmung in der Nähe von leitfähigen Implantaten zum am häufigsten publizierten Risiko. Schwerwiegendee Sicherheitsprobleme (z.B. irreparable Gewebeschäden, Fehlfunktion des Implantats) durch übermässige Erwärmung können auftreten. Aufgrund der möglichen Wechselwirkungen zwischen dem Implantat und der elektromagnetischen Felder (EMF), die während des MRI erzeugt werden, sind Patienten mit medizinischen Implantaten – insbesondere aktiven implantierbaren medizinischen Geräten (AIMDs) wie Herzschrittmachern oder Tiefenhirnstimulatoren (DBS) – nicht für MRI-Untersuchungen zugelassen und können nicht von der MRI-Diagnostik profitieren, sofern sich das AIMD nicht als MR sicherërwiesen oder eine MR mit Einschränkungen”Kennzeichnung erhalten hat.

Die erste technische Spezifikation ISO/TS 10974, die von einer gemeinsamen Arbeitsgruppe der International Standard Organization/International Electrotechnical Commission (ISO/IEC) [1] entwickelt wurde, beschreibt vorläufige Verfahren zur Bewertung von Sicherheitsrisiken einschliesslich

derer, die durch die RF-Implantat Interaktion verursacht werden. Die Spezifikation hat jedoch mehrere Lücken, die behoben werden müssen, bevor es ein ISO/IEC-Standard werden kann. Dazu gehören folgende, mit den RF zusammenhängenden Probleme:

- um das Unsicherheitsbudget des RF-Heizmodells für Implantate zu senken, müssen hochpräzise experimentelle Methoden und Instrumente mit gut kontrollierten Versuchsbedingungen entwickelt werden
- um das Patientenrisiko zu reduzieren und gleichzeitig zu stark eingeschränkte und konservative Untersuchungsbedingungen, bei denen wichtige diagnostische Informationen fehlen, zu vermeiden, muss ein umfassendes Auswertungsverfahren, das verschiedene realistische klinische Szenarien berücksichtigt, für die *in-vivo*-Interaktion zwischen RF und Mensch ermittelt werden
- für die Bestimmung des *in vivo* Temperaturanstiegs sollten zuverlässige und praktische Bewertungssmethoden entwickelt werden. Zusätzlich zu Leitlinien, wie anwendungsspezifische Risikofaktoren für den ermittelten *in-vivo*-Temperaturanstieg bewertet werden können, müssen die gewebespezifischen thermogenen Schadensschwellenwerte angegeben werden
- die in der technischen Spezifikation beschriebenen Testmethoden sind hauptsächlich dafür ausgelegt, die mit 1,5-Tesla-MRI-Scannern zusammenhängen Risiken zu adressieren; praktische Überlegungen und Einschränkungen im Zusammenhang mit höheren Feldstärken, insbesondere 3T, müssen ebenfalls adressiert werden.

Das Ziel dieser Arbeit ist es, einige dieser grossen Lücken zu schliessen. Kapitel 2 gibt einen Überblick über die technischen Fragestellungen bei der Bestimmung der Kopplung des AIMD mit den in dem MRI verkommenden RF-Feldern, zu denen vor Beginn dieser Arbeit noch keine Lösungen vorhanden waren. Eine Übersicht über den aktuellen Kenntnisstand zur MRI-Sicherheit wird in Part II vorgestellt. Die komplexe elektromagnetische MRI-Umgebung mit sehr hohen Feldstärken verursacht eine Vielzahl von möglichen negativen Wechselwirkungen der Implantate mit den EMF des Scanners, insbesondere aufgrund der erhöhten RF-Absorption um das Implantat herum, die schwer zu quantifizieren und aufgrund ihrer Komplexität nur schlecht verstanden sind. Um einen besseren Einblick in die Expositionsumgebung des Implantats zu gewinnen, bietet Kapitel 3 nicht nur einen umfassenden Überblick über den aktuellen Wissensstand zur MRI-Sicherheit einschliesslich aktuell bekannter Mechanismen, die für die potenzielle MRI-Sicherheit von Patienten mit und ohne Implantat eine Rolle spielen, sondern zeigt auch eine Gesamtschau über die Expositionsumgebung des Implantats, indem der Einfluss von möglichen klinischen Faktoren (beispielsweise anatomischer Merkmale des Patienten, Bildgebungsposition, Expositionsbedingungen) auf die RF-Expositionsumgebung des Implantats untersucht wird.

In-vitro experimentelle Methoden zur besseren und einfacheren Charakterisierung von Implantat Modellen werden in Part III beschrieben. Um die Sicherheit eines AIMD während eines MRI zu demonstrieren, ist ein numerisches Modell der RF-Reaktion des Implantats erforderlich. Das Modell muss mit einer ausreichenden Anzahl von einfallenden tangentialen elektrischen (E-) Feldbedingungen validiert werden, die sich über den gesamten Bereich von *invivo* Expositionen erstrecken. In der Vergangenheit waren solche Untersuchungen sehr zeitaufwändig und führten häufig zu limitierte Expositionsbedingungen für lange AIMDs. Die Amplitude und Phase des tangentialen E-Felds entlang des lead path in einem zylindrischen Phantom können durch Änderung der Polarisation des einfallenden Magnetfeldes der HF-Birdcage-Spule ausreichend variiert werden; dies ermöglicht die Einführung einer neuen Testfeld-Diversity-Methode (TFD), die genau definierte unterschiedliche Expositionsbedingungen bietet sowie eine verbesserte und verlässliche Validierung des AIMD-Modells mit geringer Unsicherheit ermöglicht. Die TFD-Methode wird ausführlich in Kapitel 4 diskutiert. Das vorgeschlagene TFD-Verfahren kann bei 1.5 Tesla und 3.0 Tesla Scannern angewendet werden.

Der steile räumliche Gradient (5 – 10 dB / mm) der induzierten spezifischen Absorptionsrate (SAR) in der Nähe der Implantatelektrode stellt eine grosse Herausforderung hinsichtlich der genauen Positionierung des Sensors bei der Messung der SAR im Nahfeld dar; sogar eine Abweichung von nur 0,2 mm kann in eine Unsicherheit von mehr als 2 dB resultieren. Um die strengen Positionierungsanforderungen für eine genaue Nahfeldmessung zu mindern und die mit dem experimentellen *in vitro* Versuchsaufbau einhergehenden Unsicherheiten zu verringern, wird in Kapitel 5 eine datengesteuerte experimentelle Auswertungsmethode, die auf Bildregistrierungsalgorithmen basiert, dargestellt. Die vorgeschlagene Methode wird erfolgreich gegen eine Vielzahl von Implantaten, Expositionsniveaus und Datenerfassungsverfahren validiert. Die mit dieser Methode zur Abschätzung der Energieaufnahme in der Nähe des Implantats verbundene Unsicherheit beträgt weniger als 1 dB; eine starke Abnahme gegenüber den 2 dB, die für traditionelle Methoden gefunden wurden.

Probleme im Zusammenhang mit der Bewertung der Interaktion zwischen RF und dem Menschen *invivo* werden in Part IV behandelt. Anatomische menschliche Phantome der Virtual Population (ViP) werden seit vielen Jahren als Schlüsselkomponente für realistische Dosimetriestudien verwendet. Allerdings sind die mit der Bevölkerungsstichprobe und -segmentierung verbundenen Unsicherheiten schwer zu quantifizieren, und bislang wurde noch kein entsprechender Richtwert aufgestellt. Das Ziel von Kapitel 6 besteht darin, erstmalig die Unsicherheiten der *in vivo* RF-induzierten Felder, die mit der Gewebezuordnung, der Segmentierungsqualität und der Konsistenz der virtuellen menschlichen Phantome zusammenhängen, während des MRI zu ermitteln. Durch Auswertung der Unterschiede zwischen zwei Generationen der ViP-Phantome – ViP 1.x vs. ViP 3.0, die jeweils eine bestimmte Patientenpopulation abdecken – kann gezeigt werden, dass die mit der Gewebezuweisung und der für die AIMD-Erwärmung ermittelte Segmentierungsqualität/-konsistenz verbundene anatomische Unsicherheit 0,6 dB beträgt.

Die RF-induzierte Implantaterwärmung ist eine komplexe Funktion mehrerer Faktoren, einschliesslich z. B. des MRI-Systems, der Anatomie des Patienten, der Bildgebungsposition oder der Expositionsbedingungen, weshalb eine umfassende Sicherheitsbewertung nicht aus einer nur begrenzten Anzahl klinischer Szenarien abgeleitet werden kann. Kapitel 7 fasst eine *insilico* Sicherheitsbewertungsstudie zusammen, die eine Datenbibliothek mit einem Datenanalyse-Toolset kombiniert, um umfassende Auswertungen zeitnah und nachvollziehbar durchzuführen. Der etablierte Workflow liefert nicht nur relevante, sondern auch umfassende, konsistente, erweiterbare und nachvollziehbare Ergebnisse, die den Aufbau einer bestätigten Wissensbasis aufgrund bestehender und neu aufkommender Daten erleichtern. Es fördert ausserdem die explorative Analyse von Daten zur Identifizierung von Expositionsbedingungen, was sowohl die Bildqualität als auch die Patientensicherheit maximiert.

Probleme im Zusammenhang mit der Bestimmung des *invivo* Temperaturanstiegs werden in Part V behandelt. Die Sicherheitsbewertung von AIMD erfordert die Beurteilung der RF-induzierten thermischen Gefahren für exponierte Patienten. Aufgrund der komplizierten anatomischen Merkmale des Menschen *in vivo* und der Multi-Skalen-Strukturen – Meter für den menschlichen Körper vs. Millimeter für die AIMD-Struktur – in klinischen Szenarien ist die Bestimmung des Anstiegs der *in vivo* -Temperatur extrem zeitaufwändig und rechnerisch teuer. Kapitel 8 gibt einen Überblick über die Modellierungsmerkmale, die für eine effiziente und zuverlässige Umwandlung der lokal abgelagerten RF-Leistung an der AIMD-Elektrode in den maximalen lokalen Gewebetemperaturanstieg *in vivo* ($P2\Delta T$) erforderlich sind. Die Modellierungsanforderungen und die damit verbundenen Unsicherheiten wurden durch Parameterstudien mit verschiedenen Implantatmodellen, Einfallsfeldbedingungen, Elektrodenkonfigurationen und Gewebemodellen bestimmt. Mit den daraus abgeleiteten AIMD- und Gewebemodellsimplifizierungen können vereinfachte Modelle der Leads unter einheitlicher Exposition zur Beurteilung von P2T verwendet werden, während die umligenden Gewebe im Detail modelliert werden müssen. Mit den vorgeschlagenen Vereinfachungen wird der Bewertungsaufwand $P2\Delta T$um mehr als das Zehnfache reduziert.

Zusammenfassend lässt sich sagen, dass die im Rahmen dieser Dissertation durchgeführten Arbeiten mit Hilfe von neuartigen Methoden und Modellen mit gut kontrollierten Unsicherheiten in verschiedenen klinischen Szenarien die MRI-Sicherheitbewertung von medizinischen Implantaten verbessert und vereinfacht. Sie liefert ausserdem wichtige Informationen, um einige der bestehenden Wissenslücken in den aktuellen Sicherheitsrichtlinien hinsichtlich der Exposition von Implantaten mit RF-Feldern im MRI zu schliessen.

Acknowledgments

It feels just like yesterday that I came to Switzerland and join in IT'IS Foundation as a Ph.D student. I have to say, it is not an easy journal, but it has been one of the most valuable and extraordinary time during my academic life. Because of the challenging work I was working on and most of important, the people I am working with.

My deepest gratitude goes to my group leader, Dr. Earl Zastrow and the director of the IT'IS Foundation, Prof. Niels Kuster, for giving me the chance take part in this venture. I would especially like to thank Dr. Earl Zastrow for her rigorous scientific attitude, outstanding professional knowledge, and also for her support as a friend. I would also like to especially thank Prof. Niels Kuster for reviewing my publications and providing me with invaluable comments and suggestions, thank his 'always to be the best' requirement towards every students.

This thesis would not have been successful without the excellent academic environment I found myself in. I would like to express my gratitude to Prof. Qiuting Huang for accepting me as his Ph.D student and being part of ETH Zurich. Thanks to Prof. Theodoros Samaras for accepting to be part of my jury and reviewing my thesis.

Over the years at IT'IS, I have had the chance to work with the most wonderful co-workers at Z43, I would like to thank all friends and colleges working in this big family, they incredibly enriched my life at Z43 and supported me in many ways. Thanks to Manuel Murbach for giving advice on scientific work. Thanks to Esra Neufeld from time to time lightening me in the dark with his acute scientific instinct. Thanks to Myles Capstick for his valuable guidance as an engineering. Thanks to the girls in my office (Maria Cabanes, Ilaria Liorni, and Nassim Nasseri) for their encouragement and sharing experience. Thanks to Sven, Beyhan Kochali, and Andrea

Tonini for their brain and muscle support in yellow chamber. Thanks for Pat, Sabine,Tolga and Ingmar for careful review of my papers. Thanks to Yijian Gong for sharing the Ph.D experience with me. Thanks to Jacqueline Pieper for her support in administration management.

Thanks to the S4L team for their efficient technical support: Benjamin Drayer, Cosimo Fortunato, and Sylvain Reboux. We have learned a lot from each other. Thanks to Erdem Ofli for providing support and always be a big brother. Thanks to Bryn Lloyd for the help in virtual population. Thanks to Theodoros Samaras for reviewing the paper and give comments. Thanks to my 'China workshop' team Nik, Mark, Erdem and Maxwell, I have learned a lot for you and had a great time every year.

Over the years, I had the opportunity to work with collaborators from all over the world. Thanks to Elena Lucano for collaborations. Thanks to Juan for his patients and sharing of knowledge. Thanks to Walfang Kainz from FDA for the support in virtual population related work. Thanks to Quirino Balzano for his kindness and wisdom.

My life in Switzerland will not be the same without my friends believing me and supporting me in good and bad times. I would like to thank Elliott Zastrow, who treat me as his little sister and is always there supporting me. Thanks to Bizzy, the most sweet and smart princess I ever seen. Thanks to Ferenc Muranyi for his generosity and encouragement. Thanks to Emilio Cherubini for his slow style of optimistic. Thanks to Eugene Grobbelaar for the fun he brought to every party. Thanks to Saskia for her gentleness. Thanks to Juliet for her strong heart. Thanks to Parisa for her openness.

Besides, I would also like to thank for the most beautiful and amazing music from Chopin, where I could always found inner peace.

My deepest thankfulness belongs to my dearest family—my parents, my sister, and my husband, for their unshakable support, encouragement and love.

Part I

Introduction

Chapter 1

Background, Motivation, and Objectives

1.1 Background

The fundamental principle of magnetic resonance imaging (MRI), the nuclear magnetic resonance (NMR) phenomenon, was discovered independently by Edward M. Purcell and Felix Bloch [2] in the late 1940s. NMR phenomenology is based on the propensity of some atomic nuclei (e.g., ^{1}H) to possess an inherent angular momentum, which causes a magnetic moment to be generated due to the charged particles in the nucleus. The time-dependent behavior of nuclear moments under the external static and time-dependent magnetic fields can be described by the Bloch equation[2]. In MRI, pulses of radiofrequency (RF) waves are used to excite the nuclear spin energy transition, thereby generating a detectable RF signal, which then applies magnetic field gradients that localize the signal in space. The first MRI, depicting two tubes of water, was published by Paul Lauterbur in 1973, followed by an image of a mouse thoracic cavity in 1974. The term MRI is preferred over NMR imaging as it avoids negative associations patients may have with the word ‘nuclear’ [3]. It is further sensible to use a term that distinguishes MRI from the NMR spectroscopy methodologies used in chemical analysis.

1.1.1 MRI Safety in the Absence of Implants

MRI, which enables the generation of high-quality images of the inner tissues of the human body without ionizing radiation, has become a widely used medical diagnostic technique. Figure 1.1 shows the fundamental components of an MRI system, comprising the strong static magnetic field (B_0) for alignment of the spins, pulsed gradient magnetic fields (G) for applying spatially and temporally different effective magnetic fields, and a pulsed RF field for the spin nutation at the Larmor resonance frequency. Apart from some specialized areas, such as RF hyperthermia, there is no other modality whereby patients are exposed to such high static, low-frequency (kHz), and RF (MHz) fields. The complex environment of electromagnetic fields (EMF) to which patients are exposed during an MRI procedure has raised questions about MRI safety since the 1970s [4, 5, 6, 7].

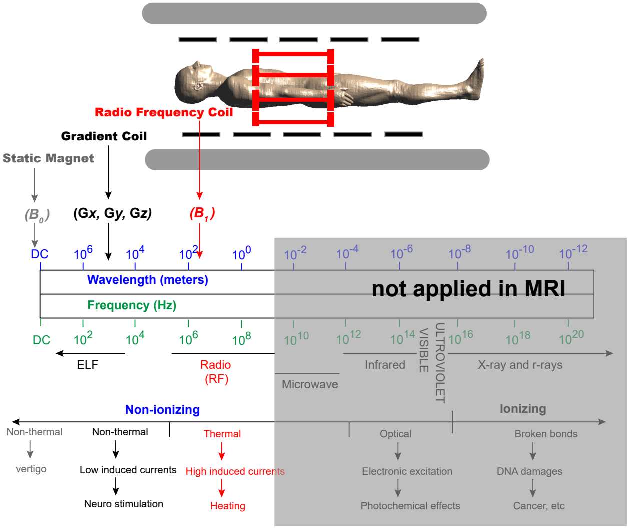
Radio Frequency Coil
Gradient Coil
Static Magnet
(B_0)
(Gx, Gy, Gz)
(B_1)
DC
10^6
10^4
10^2
10^0
10^{-2}
10^{-4}
10^{-6}
10^{-8}
10^{-10}
10^{-12}
Wavelength (meters)
Frequency (Hz)
not applied in MRI
DC
10^2
10^4
10^6
10^8
10^{10}
10^{12}
10^{14}
10^{16}
10^{18}
10^{20}
ELF
Radio
(RF)
Microwave
Infrared
VISIBLE
ULTROVIOLET
X-ray and r-rays
Non-ionizing
Ionizing
Non-thermal
vertigo
Non-thermal
Low induced currents
Neuro stimulation
Thermal
High induced currents
Heating
Optical
Electronic excitation
Photochemical effects
Broken bonds
DNA damages
Cancer, etc

Figure 1.1: Fundamental components of an MRI system with the corresponding wavelengths and frequencies of the magnetic fields generated by these components.

Potential hazards intrinsic to MRI environments – including, e.g., static vertigo induced by the static field B_0, peripheral nerve stimulation induced by the high switching rate of the gradient fields, tissue heating induced by RF fields, etc. – have been widely acknowledged [8, 9, 10, 11, 12, 13, 14, 15]. Guidelines and safety standards relating to interactions of EMF with humans have existed since 1998 [16, 17], and different exposure limits are recommended for the general public than for those under working conditions. As a compromise between risk and benefit in MRI, the standardized exposure limits established for patients approach the physiological limits and are much higher than levels of exposure considered safe for the general public and occupational exposure levels, i.e., 50 times higher than for the general public and 10 times higher than the occupational limits. MRI-related patient safety standards have been considered by several organizations, including the U.S. Food and Drug Administration (FDA) [18], the International Commission on Non-Ionizing Radiation Protection (ICNIRP) [19], and the International Electrotechnical Commission (IEC) [20]. In the international standard codified in IEC 60601-2-33, one of the most common product standards complied with by MRI manufactures, the temperature limits are set at 38°C in the head, 39°C in the trunk, and 40°C in the extremities. Despite the uniquely high exposure to EMF during MRI, most of the potential hazards for patients are avoided or mitigated when proper procedures and guidelines [21, 22, 23, 24, 20] for MRI safety are followed.

1.1.2 MRI Safety with Implants Present

As the population of patients with chronic diseases – e.g., Parkinson's disease, heart disease, chronic pain, etc. – has rapidly increased, the number of patients implanted with medical devices has also constantly and rapidly grown and now comprises several million patients worldwide [25]. The variety of implantable medical devices currently being marketed is large and includes both passive implants – such as metal screws, stents, and artificial hips – and active implants, such as pacemakers and deep brain and spinal cord stimulators. As shown in Figure 1.2, the typical active implantable medical device (AIMD) includes a signal generator that houses the controlling electronics and one or more conductive leads that transfers the treatment signal to the relevant tissues, e.g., the right ventricle for a pacemaker. Due to the complex electrical structure and components of AIMDs, we focus in this work mainly on the safety problems imposed by AIMDs.

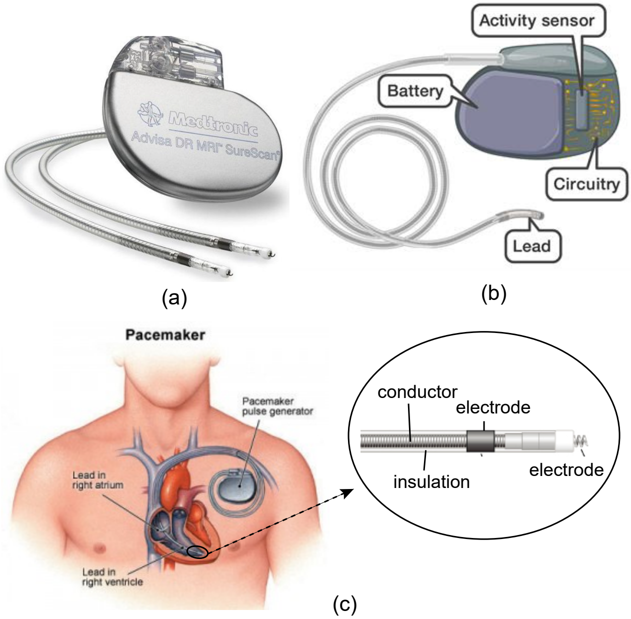
Medtronic
Advisa DR MRI SureScan
Activity sensor
Battery
Circuitry
Lead
Pacemaker
Pacemaker pulse generator
Lead in right atrium
Lead in right ventricle
conductor
electrode
insulation
electrode

(a) (b)

(c)

source: https://intensivecarehotline.com/pacemaker/

Figure 1.2: An example AIMD: (a) the Medtronic pacemaker; (b) the basic components of the pacemaker; and (c) a typical *in vivo* position of the pacemaker and the structure of the lead.

The various potential problems that exist for a patient with an AIMD undergoing an MRI procedure include mechanical movement or dislodgment through force or torque induced by the magnetic field [26, 27], damage to the electrical circuitry of the device through exposure to EMF during the operation of the MR system [28, 29], and heating of the device and adjacent tissue through absorption of RF energy. Aside from any direct harm caused by MRI-induced effects on the AIMD itself, the electrically conductive material of the AIMD may generate distortions in the MRI scan. Such distortions are caused by the disruption of the homogeneity of the local magnetic field, which leads to a change in the position-frequency relationship that is crucial for accurate reconstruction of the image [30]. Figure 1.3

demonstrates image artefacts caused by a cochlear implant with and without a magnet [31].

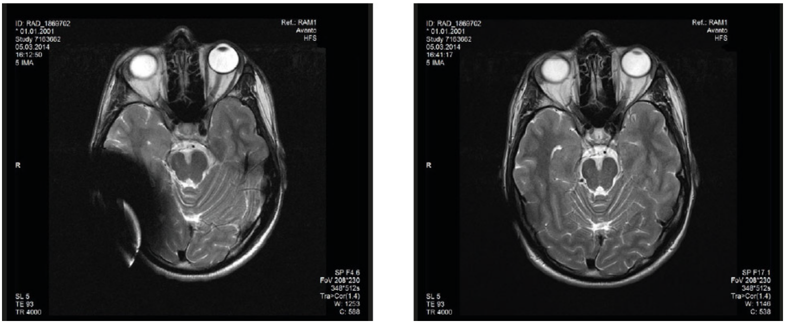
ID: RAD_1869702
* 01.01.2001
Study 7163662
05.03.2014
16:12:50
5 IMA
Ref.: RAM1
Avanto
HFS
R
SL 5
TE 93
TR 4000
SP F4.6
FoV 208*230
348*512s
Tra>Cor(1.4)
W: 1253
C: 588
ID: RAD_1869702
* 01.01.2001
Study 7163662
05.03.2014
16:41:17
5 IMA
Ref.: RAM1
Avanto
HFS
R
SL 5
TE 93
TR 4000
SP F17.1
FoV 208*230
348*512s
Tra>Cor(1.4)
W: 1146
C: 538

Source: Medical Procedures for MED-EL CI Systems. https://s3.medel.com/documents/AW/AW33290_50_Manual_Medical_Procedures_CI_Systems_EN-english-US.pdf

Figure 1.3: Image artefacts (axial view) caused by the presence of a cochlear implant during a spin echo pulse sequence in a 1.5 T MRI scanner (left image) compared to image artefacts resulting after the magnetic implant was replaced with a non-magnetic spacer (right image).

Among these safety hazards, the RF-induced heating inside a patient with an active implantable medical device is one of the most serious safety concerns, due to the potential for highly concentrated *in vivo* local tissue heating near the implant electrode. The repeated RF pulses used for signal induction in MRI can generate strong electric fields inside the body and lead to high local deposition of energy density in the tissue surrounding the conductive ends, e.g., electrodes, of the implant leads. The amount of RF-induced tissue heating can potentially be significant for elongated implants such as cardiac pacemakers, defibrillators [32, 33], and neuro stimulators [34, 35], and the high local levels of deposited power may consequently cause irreversible damage to tissue. The magnitude of RF-heating depends on a multitude of variables specific to the MRI system (e.g., RF-coil design and manufacturer's power calculation algorithm [36]), the implant (e.g., geometrical built and location [33, 37]), and the patient imaging conditions (e.g., patients anatomy, posture, and position with respect to the RF-coil[38]).

The severity of the risk to the patient caused by RF-induced heating is difficult to generalize with thermal metrics alone. For example, although substantial tissue heating in the vicinity of a cardiac rhythm device has been reported during MRI scanning [32], the results of several recent studies demonstrate that MRI scanning of patients with implants can be safe [39, 40]. On the other hand, while substantial tissue heating in the vicinity of a cardiac pacemaker can be tolerated and does not cause consistently detectable histological alteration [32], a relatively small temperature increase of brain tissue induced by a deep-brain stimulator may be detrimental. Figure 1.4 shows an example of a brain lesion caused by an inappropriate setting during an MRI scan of a patient implanted with a deep brain stimulator (DBS) for Parkinson's disease labelled as 'MRI conditional'. Therefore, extreme precautions must be taken to carefully limit the RF exposure in patients with implanted AIMDs, and the guidelines of the implant manufacturers must be followed strictly.

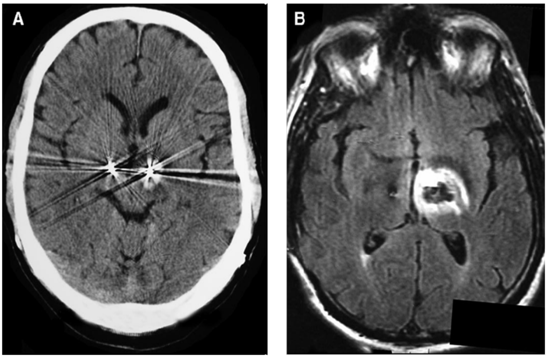

[redacted]

Source: J.M. Henderson, et al., "Permanent Neurological Deficit Related to Magnetic Resonance Imaging in a Patient with Implanted Deep Brain Stimulator Electrodes for Parkinson's Disease: Case Report ", Neurosurg., 57(5), 2005

Figure 1.4: CT scan images of patient implanted with a DBS revealing the lesion – caused by the interaction between the RF field inside the MRI and the DBS inside the patient's brain – surrounding the left electrode of the DBS [34].

1.1.3 RF Safety Assessment of AIMDs

Because of the established potential hazards, introduced in Section 1.1.2, millions of patients with implanted AIMDs are excluded from the benefits of safe MRI diagnoses. On the other hand, MRI scans are recommended for more than 40% of patients with implant devices [41]. Implant manufactures have exerted tremendous effort to the development of AIMDs labelled 'MRI safe' or 'MRI conditional', and there is, consequently, a large demand for the advancement of methodologies that enable trustworthy assessment of AIMD safety during MRI.

As *in vivo* assessment within the patient is generally not feasible, *in silico* trials and animal experiments are often used as a proxy to allow assessment of implant safety without posing potential health risks to patients. Unfortunately, both of these approaches have limitations. The computational resources required for *in silico* trials to resolve the multi-scale structures during full-wave modeling of clinical scenarios are so extremely demanding as to preclude the possibility of performing the safety evaluations through *in silico* trials alone. Animal experiments, on the other hand, are very costly – which limits the number of experiments that can be performed – and the exposure conditions are difficult to control, which leads to high experimental uncertainty. Clinical trials are, thus, under consideration as a potential alternative to provide a clear path to safety assessment. However, clinical trials of a limited number of scenarios are unlikely to provide sufficient data to ensure safety for all potential clinical scenarios. At a minimum, a comprehensive safety evaluation must take a significant number of cases of relevant RF exposures into consideration and provide a concrete method for RF characterization of implants.

In consideration of these practical limitations and restrictions of *in silico* and clinical trials, technical specification ISO/TS 10974 for AIMDs in MRI has been developed by a joint working group of the International Standard Organization (ISO) and the IEC [1] to provide guidance for the safety evaluation of AIMDs. According to ISO/TS 10974, a comprehensive assessment of RF-induced heating for patient with AIMD can be performed in a progressive manner by first estimating the RF power deposition near the AIMD, then converting the power deposition to an *in vivo* temperature increase.

Four tiered approaches for determining RF power deposition around the AIMD electrode are proposed in Clause 8 of the ISO/TS 10974 [1]. The four tiers are arranged in order of increasing complexity of evaluation methodology, as well as increased accuracy of the resulting estimation:

- Tier 1, the most conservative approach to the determination of power deposition, requires no electromagnetic (EM) modeling — the maximum induced electrical field is used as the incident field.
- Tier 2 relies on EM modeling of the interaction of RF fields with human tissue to evaluate the electric field in the implant volume of interest, and the maximum electric field within the volume of interest is used as the incident field.
- Tier 3 involves EM modeling to determine the tangential electric field (E_{tan}) along AIMD routing tracks, which is used as the incident field.
- Tier 4 involves concurrent modeling of human and AIMD models for the relevant RF exposure conditions and results in the smallest amount of overestimation.

Tiers 1 and 2 can be used to assess only electrically short AIMDs due to phase effects, as described in Annex K of [1], while Tier 4 requires the use of extremely expensive computational resources to carry out concurrent modeling of a human, on the scale of meters, and AIMDs on the millimeter scale. Tier 3, however, is based on a synergy of *in vitro* experimental testing and *in silico* analysis to enable assessment of patient risk due to RF-implant interaction during MRI. Tier 3 is designed to significantly reduce the numerical complexity of multi-scale full-wave evaluation in Tier 4, thus increasing the assessment efficiency sufficiently that it can be applied to a wide range of clinical scenarios. The biggest advantage of the Tier 3 approach is that it separates implant-RF interactions – characterized by the AIMD RF transfer function – from human-RF interactions – characterized by the B_1-induced tangential electrical field along the AIMD routings inside the human body. The combination of these two parts can provide an estimation of the local power deposition in tissues due to the AIMD. The evaluation of implant-RF interactions is often conducted through *in vitro* experiments, while the evaluation of human-RF interactions is accomplished through *in silico* modeling.

1.2 Motivation

In recent decades, comprehensive research efforts and implant development have led to a lowered risk for unintended coupling of the conductive implants with the RF fields. Several products have been approved by the FDA or European Medical Agency (EMA) for clinical use[42, 43]. The first device to be officially labelled ‘MRI conditional’ by the EMA was released in 2008, and the first FDA-approved device followed in 2011. However, reports of several patient tissue damage cases associated with AIMDs during MRI [32, 34] reinforces the realization that caution is required when imaging patients with biomedical implants or devices. Thus, it is important that MRI compatibility be demonstrated by proper procedures as defined by the standards or a recognized authorization body such as the FDA or EMA[25].

Although the procedure for testing RF-induced heating inside patients with AIMDs is provided in the technical specification [1], the characterization method and uncertainty control must be designed and determined by practitioners. The rapid expansion of the types and models of AIMDs – with varied and complex structures – being introduced on the market complicates the process of being able to provide up-to-date device information to ensure that the evaluation of the device is as thorough as possible. Furthermore, when the literature indicates that an implant or device is MRI safe, the thoroughness and competence of the assessment result should also be considered with respect to the MRI system, pulse sequence, and examination setup used. Given the relative risks posed by the large number of implantable electronic devices, MRI systems, and pulse sequences, the establishment of an effective pre-MRI evaluation is critical for the safety of all individuals with AIMDs entering the MRI environment.

As the implant RF-heating model is derived from *in vivo* experimental characterization and validation tests, to improve the accuracy of the implant model, both measurement accuracy and the exposure conditions of the *in vitro* radiated tests must be well-characterized and well-controlled to minimize the uncertainty and errors due to the experimental design.

The extreme field gradients generated near the implant electrode (5 – 10 dB/mm) are one aspect of the major limitations of the measurement accuracy; with a sensor position error of 0.2 mm, the uncertainty caused by the sensor position can be more than 2 dB. Another limitation comes from the exposure field diversity achievable during the radiated test. Although several phantom and implant routing combinations to achieve the exposure field diversity are recommended in the current guidelines, the feasible field diversity is still limited by the meter-scale implant structure and finite test phantom volume. If, during the design of the implant routings, we take into consideration the phantom boundary reflection and adjacent implant segments coupling effects, the available implant routing and phantom combinations for the exposure diversity will be greatly restricted. These practical experimental limitations need to be considered and addressed with *in vitro* experimental evaluation methods. Sufficient diversity and high accuracy must be established to enable accurate characterization of AIMD RF-heating models.

The *in vivo* power deposition inside patients with implantable medical devices during MRI depends not only on the characteristics of the implant but also on the *in vivo* exposure environment caused by the interaction of RF-fields with human tissues. Anatomical human phantoms are a key component of dosimetric studies designed to investigate how the absorption of EMF by the human body impacts the assessment of implant safety [44, 45]. It is important to note, however, that uncertainties related to the anatomical phantoms are difficult to quantify, and that a benchmark does not yet exist. Therefore, questions related to the uncertainty due to the limitations posed by the phantoms with respect to population sampling, segmentation, tissue parameters, and discretization must be addressed and clarified. While the latter two factors can be easily evaluated through a sensitivity analysis, the first two are difficult to quantify, as the number of samples and the level of segmentation cannot be easily increased or varied; the workload involved in data acquisition, segmentation, model generation and validation is extremely high, requiring at least one person-year for each new model. On the other hand, the *in vivo* RF-human interaction depends on many clinical factors, including the MRI scanner technology (e.g., RF coil and pulse sequence design), patient anatomy (e.g., patient size, body mass index), imaging position, exposure level, etc. Therefore, a comprehensive safety assessment cannot be derived from limited scenarios possible in a clinical trial, and it is important that a comprehensive evaluation of different clinical factors be performed in a timely and traceable manner. It is, therefore, necessary to take these various clinical factors into consideration when the RF-induced fields inside the human body are investigated and analyzed.

The ultimate goal when evaluating RF-induced heating in a patient is to determine the degree of potential tissue damage, for which the temperature increase is the most logical metric. Given the *in vivo* power deposition, the estimation of temperature increase in the tissue is achieved by converting local *in vivo* power deposition into *in vivo* temperature changes, for which thermal simulation algorithms can be used. However, the complicated *in vivo* tissue environment inside human body and the multi-scale structure – meter scale for human body and millimeter scale for AIMD structures – involved in the clinical scenarios make computations extremely time consuming and expensive. A more efficient way to derive the *in vivo* thermal response of an AIMD is needed.

1.3 Objectives

The goal of this thesis is to develop better, easier, and more comprehensive evaluation methods for RF-induced heating inside a patient with an AIMD during MRI exposure. The problem definition is divided into three parts : (1) *in vitro* experimental methods used for accurate characterization and validation of an AIMD RF-heating model; (2) evaluation of *in vivo* RF-human interaction; and (3) determination of *in vivo* temperature increase. To address these problems, it is necessary to identify the practical experimental limitations and quantify the related uncertainties inherent in the *in vitro* experimental testing, develop an experimental evaluation method to reduce the inaccuracy caused by the specific absorption rate (SAR) and the high temperature gradients near the implant electrodes, formulate experimental methods for the characterization and validation of the RF-heating model under diverse and well-controlled exposure conditions, quantify the contribution of the anatomical uncertainty due to the segmentation in the phantom to the evaluation of *in vivo* AIMD power deposition, investigate the *in vivo* implant exposure environment with various clinical scenarios taken into account towards providing the workflow for timely and traceable evaluation of a wide range of patient exposure scenarios, and derive procedures for simplification of implant and tissue models to enable more efficient conversion of *in vivo* power deposition to *in vivo* temperature increase.

1.4 Synopsis

This thesis is organized into six parts.

- Part I — Introduction

  - Chapter 2: Practical Considerations in Experimental Evaluations of RF-Induced Heating of Leaded Implants: an overview of the engineering issues in determining the coupling of the AIMD with the RF fields of the MRI are provided, the related uncertainties are quantified.

- Part II — Review of State-of-Knowledge: A comprehensive review of the current knowledge about the MRI safety is provided

  - Chapter 3: Electromagnetic MRI Safety with and without Implantable Metallic Devices: A Review: to better understand the potential adverse interactions of the MRI scanner with the implant, the complex and hostile electromagnetic environment has been summarized. The influence of patient anatomy, imaging position, and exposure conditions have on the implant *in vivo* exposure environment in MRI has been investigated.

- Part III — *In Vitro* Experimental Methods: *in vitro* evaluation methods to allow accurate characterization and validation of RF-implant models under diversified and well-controlled exposure conditions are proposed

  - Chapter 4: Novel Test Field Diversity Method for RF Transfer Function Validation Required for Demonstrating MRI Safety of Active Implantable Medical Devices: a carefully designed test setup is introduced for an efficient and reliable method to characterize the AIMD RF-heating model by means of test-field-diversity testing; the proposed method provides diverse incident conditions to the implant under test while preserving the fidelity of the incident conditions; the implementation of the proposed test-field-diversity method is applied to a 90-cm-long spinal cord stimulator lead in both 1.5 T and 3.0 T MRI-exposure systems
  - Chapter 5: Data-Driven Experimental Evaluation Method for the Safety Assessment of Implants with Respect to RF-Induced Heating During MRI: a new, data-driven experimental method is proposed to reduce the inaccuracy of the available methods caused by the high spatial gradients of SAR distribution near the

    electrodes of AIMDs; the proposed method increases the accuracy over that of traditional methods through the use of simple numerical modeling and imaging co-registration algorithms to overcome the stringent requirements on sensor positioning

- Part IV — *In Vivo* Human-RF Interaction Evaluation: the uncertainty related to the impact of anatomical segmentation on the determination of *in vivo* power deposition is characterized and quantified to establish a workflow for thorough assessment based on a comprehensive *in vivo* data library

  - Chapter 6: Anatomical Model Uncertainty for RF Safety Evaluation of AIMD Under MRI Exposure: to quantify the uncertainty associated with tissue assignment and segmentation quality and consistency of digital human phantoms, we used two generations of virtual population phantoms (ViP 1.x and ViP 3.0) to assess AIMD-related risk during MRI: the RF-induced 10g-averaged E-fields, the tangential E-field distribution along AIMD routings, and the estimated *in vivo* power deposition are determined for five phantoms available from both ViP 1.x and ViP 3.0.
  - Chapter 7: A Comprehensive Data Library Combined with an Analytics Toolset for Standardized, Validated, and Effective Safety Assessment of Patients with Medical Implants during MRI Exposure: the RF-induced heating in a patient implanted with an AIMD is a complex, multi-factor function; to enable a comprehensive safety assessment in a timely and traceable way, we established a standardized and effective safety assessment workflow based on a comprehensive data library combined with an analytics toolset

- Part V — Determination of the *In Vivo* Temperature Increase: implant and tissue model simplifications that enables accurate conversion of *in vivo* power deposition to *in vivo* temperature rise for AIMDs exposed to MRI environment are established.

  - Chapter 8: Efficient and Reliable Assessment of the Maximum Local Tissue Temperature Increase at the Electrodes of Medical

    Implants under MRI Exposure: to enable efficient and accurate conversion of *in vivo* power deposition into *in vivo* temperature increase, implant and tissue model simplifications for the derivation of the *in vivo* thermal response of AIMDs are proposed; the feasibility and efficiency of the proposed simplification has been validated for two common clinical scenarios

- Part VI — Epilogue: conclusions and outlook
    - Chapter 9: Conclusions and Outlook on Related Future Research Topics
- Part VII — Appendices: includes supporting information for chapters 3 and 4, lists of acronyms, symbols, tables, and publications
    - Appendix A Supporting Information for Chapter 4
    - Appendix B Supporting Information for Chapter 5
    - Appendix C List of Acronyms
    - Appendix D List of Symbols
    - Appendix E List of Publications

Chapter 2

Practical Considerations in Experimental Evaluations of RF-induced Heating of Leaded Implants

2.1 Abstract

[1]This study illustrates some practical considerations to accommodate the non-ideality of experimental conditions needed in the Tier 3 assessment of RF-induced heating of leaded implants. The method, based on Tier 3 safety assessment during MRI exposure of ISO/TS 10974, is currently used for the rapid modeling of RF-implant interactions. We summarize the theoretical accuracy of Tier 3 method and the practical considerations for its actual implementation.

---

[1] This Chapter has been published in [46]

2.2 Introduction

The Tier 4 method [1] requires the direct modeling of electromagnetic field (EMF) interactions of the implant under clinical MRI conditions, which can be achieved by computational electromagnetic (CEM) modeling of the implant integrated within the human body under MRI-based RF exposure. Tier 4 remains the only method whereby RF-implant interactions within a complex anatomy are not compromised by any simplifying assumptions. Although the Tier 4 method is intuitively simple, it is computationally demanding — especially for leaded implants. The spatial resolution of the numerical model is usually dictated by the smallest geometry within the computational domain. For the case of RF-implant interactions during MRI exposure, submillimeter resolution is often required to resolve the geometrical features of the implant. Such fine resolution, also extended to the RF-coil and the patient anatomy, would render the size of the whole computational domain exceedingly large.

The Tier 3 method of [1] is designed to alleviate the computational burden inherent in Tier 4 evaluation. Simplifying assumptions regarding RF-implant interactions inside the complex human anatomy are introduced to enable the separation of this computationally large problem. Tier 3 method involves a separate evaluation of (a) RF-induced heating characteristics of the implant and (b) RF exposure of patients undergoing MRI; these are combined to provide an estimate of the local power deposition in tissues by the implant. Implementation of the Tier 3 method was demonstrated in several studies [47, 48, 38]. The evaluation of (a) is often conducted experimentally, while the evaluation of (b) is accomplished through *in silico* trials. Therefore, *in vitro* experiments are an intrinsic part of Tier 3 evaluation. Here, we summarize some of the difficulties encountered during experimental implementation tests of (a) and their mitigation strategies.

2.3 Experimental Characterization of Implant RF-induced Heating

Piece-wise excitation (πX) is a Tier 3-compliant method that can be used to characterize RF-induced heating of medical implants. The characterization is based on the technique proposed in [49] where a transfer function, henceforth referred to as the πX model, $h(l)$, is defined as the relationship between the locally induced electric field around an electrode pole and excitation along length l of the implant. Figure 2.1 depicts a schematic of the method.

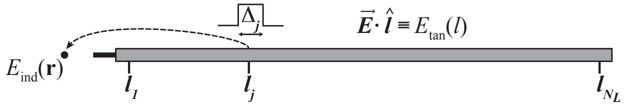
Δ_j
$\vec{E}\cdot\hat{l} \equiv E_{\text{tan}}(l)$
$E_{\text{ind}}(\mathbf{r})$
l_1
l_j
l_{N_L}

Figure 2.1: Schematic of the piece-wise excitation method. $\hat{\boldsymbol{l}}$ is the unit tangential vector to the implant at length l.

The tangential component of the local incident electric field, E_{tan}, is coupled with the implant at length l and the induced electric field around a region of high-heating (e.g., in the vicinity of stimulating electrodes) at point $\boldsymbol{r}$, $E_{\text{ind}}(\boldsymbol{r})$, is evaluated. Therefore, the total induced power of the tip electrode (P_{TIP}), attributed to E_{tan} coupling along the entire implant of length L can be estimated from the relation:

$$P_{\text{TIP}} = W_0\Big(\sum_{j=1}^{N_L} h(l_j)E_{\text{tan}}(l_j)\Delta_j\Big)\Big(\sum_{j=1}^{N_L} h(l_j)E_{\text{tan}}(l_j)\Delta_j\Big)^* \tag{2.1}$$

where W_0 is the P_{TIP} of an implant for $E_{\text{tan}} = 1V/m$.

The most evident simplifying assumption in the derivation of a Tier 3 model is that the complex tissue composition is approximated with a tissue-simulating medium (TSM). In practice, Tier 3 model is often derived from *in vitro* experiments with the implant submerged in a TSM-filled test phantom. We shall demonstrate our considerations during the design of the experimental system using two generic implants. The generic implants are 400-mm and 800-mm long insulated wires comprising a 1.5-mm diameter conductor with a 0.5-mm thick insulation layer. The insulation is removed at one termination, leaving a 10-mm long exposed conductive tip. To derive the πX model, each generic implant is placed in a homogeneous TSM-filled phantom and local excitation tracks along the length of the leaded implant, similar to the schematic of Figure 2.1. In this study, the dielectric properties of the TSM are similar to those specified in [1]. We shall illustrate the evaluation at 64 MHz (1.5 T MRI). Figure 2.2 depicts our experimental system

(πX), designed to derive a Tier 3 model of RF-induced implant heating.

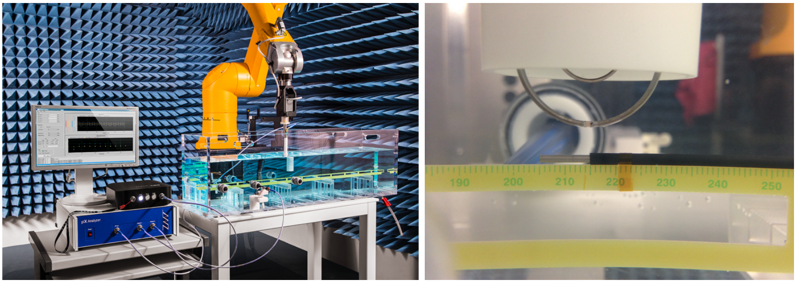

(a) (b)

Figure 2.2: The experimental system for deriving πX models of implant RF-induced local power deposition. (a) The πX system. (b) Close-up of the local excitation source and the exposed 10-mm conductive tip of the 800-mm implant.

The TSM has an attenuation constant of α = 0.082 Np/cm (α = 0.72 dB/cm). Our first prototype of the πX system comprised a 20 Liter (L) homogeneous TSM-filled phantom and the implant is placed at 6 cm away from all boundaries; we anticipated that with such extreme loss of the TSM, the finite boundaries would insignificantly affect the πX models derived with experimental system. However, we found that the πX models noticeably deviate from the numerical solution, derived from full-wave CEM simulations assuming implant immersion in an unbounded medium. The simulations are performed with SEMCAD X (SPEAG, Zurich), a platform based on the finite difference time-domain method [50]. It will be shown that this oversight substantially affects the prediction of the power deposition of the implants, calculated by the πX models. The πX systems was revised to include a 70 L homogeneous TSM-filled phantom with the distance between the implant and all boundaries of 12 cm. In Figure 2.3, we compare the πX models derived from full-wave CEM simulations, the experimental system with 20 L phantom, and the experimental system with 70 L phantom. It is clearly shown that the πX models derived from the revised experimental setup converge to the numerical solutions.

For each implant, the induced power deposition at the conductive tip of

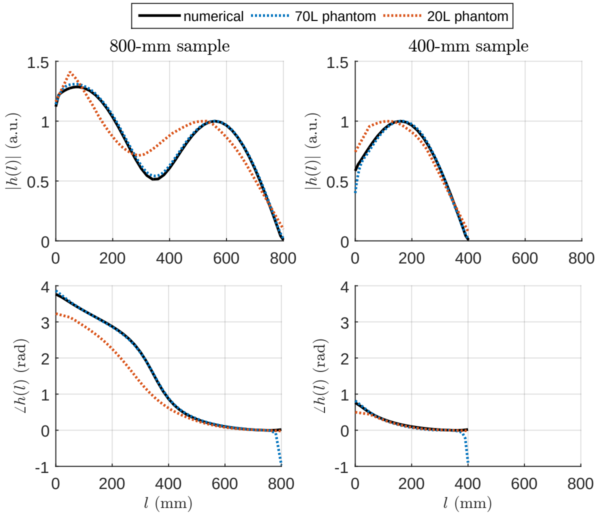

Figure 2.3: The πX models of the 400- and 800-mm implants, derived from numerical simulations with unbounded medium (black solid), the experimental system with 20 L phantom (orange dotted), and the experimental system with 70 L phantom (blue dotted). Up: magnitude of the models; Down: phase of the models;

the implants from approximately 40 different exposures are computed from direct modeling of the implant-RF interactions via full-wave CEM simulations. The power deposition of the two implants are compared with the values predicted by the πX models, numerically derived from CEM and the πX models, experimentally derived from the two versions (20 L and 70 L TSM-filled phantoms) of the πX system. Same RF exposure conditions as those considered in the direct implant-RF modeling, are used for the πX predictions. The considered exposure conditions are shown in Figure 2.4. Figure 2.5 illustrates the power deposition of each generic implant under different RF exposures, obtained from (a) direct modeling of implant-RF interactions via full-wave CEM simulations; (b) Equation 2.1 with numerically-derived πX model; (c) Equation 2.1 with πX model experimentally-derived in 20 L phantom; and (d) Equation 2.1 with the πX model experimentally derived in 70 L phantom. For the short implant (400 mm), the estimated P_{TIP} obtained with both experimental systems are within 1 dB of those obtained from direct CEM modeling and numerically-derived πX model; whereas for the long implant sample (800 mm), the estimated P_{TIP} obtained with the experimental system with 20 L phantom is significantly below (more than 5x) those obtained from direct CEM modeling and the numerically-derived πX model.

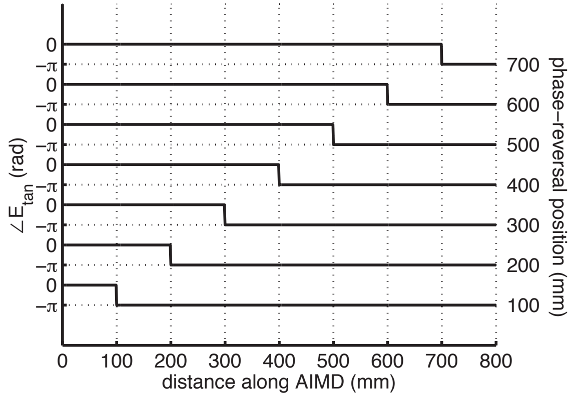

(a)

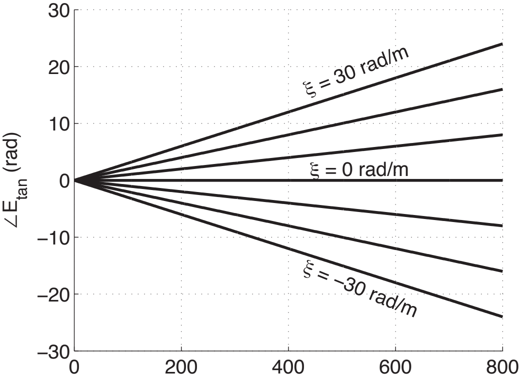

(b)

Figure 2.4: Phase distribution along the length of the implants of the exposures used in the calculation of power depositions from the πX models. $|E_{\text{tan}}(l)|$ is always unity. (a) Phase- reversal exposure. (b) Linear-phase exposure.

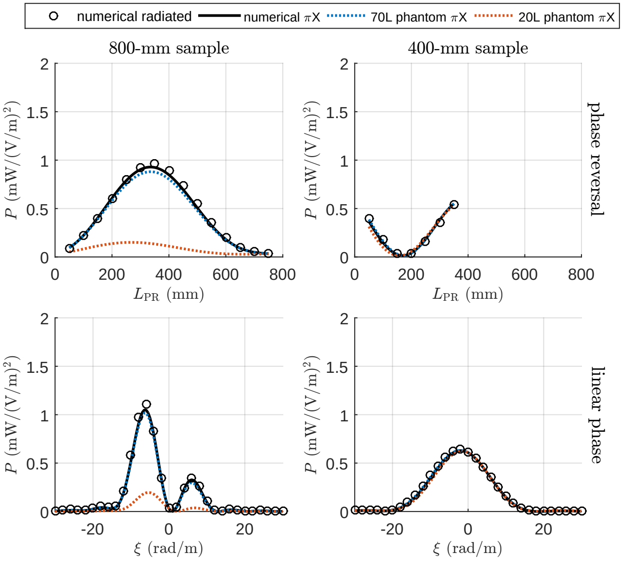

Figure 2.5: The power deposition of each generic implant per unit $|E_{\text{tan}}(l)|$ obtained from the direct implant-RF modeling ('o' makers), the numerically-derived πX model (black solid), the experimentally-derived model in 20 L phantom (blue dotted), and the experimentally-derived model in 70 L phantom (orange dotted).

2.4 Experimental Radiated Testing of Implant RF-induced Heating

Experimental radiated immunity test is also an integral part of RF-induced heating evaluation. For example, it is needed for the validation of an implant model. A radiated immunity test generally comprises a TSM-filled phantom where the implant is submerged and an RF exposure source. For leaded implants, the RF-induced heating is dominated by the coupling of the implant with the tangential component of the electric fields along its length, $E_{\text{tan}}(l)$. Therefore, different exposure conditions can be carefully designed by adjusting the implant routing paths within the phantom. Several examples are provided in [1].

Despite that the provisional guidelines may suggest, the experimental uncertainty of the exposure design must still be carefully investigated before its experimental implementation. Here, we demonstrate the design of a phase-reversal exposure condition which is commonly used in the radiated test of leaded implants. Figure 2.6 illustrates two example experimental setups to achieve phase-reversal RF-exposure to the implant. The leaded implants are bent at the phase-reversal position and the different segments of the implants are separated by a finite distance.

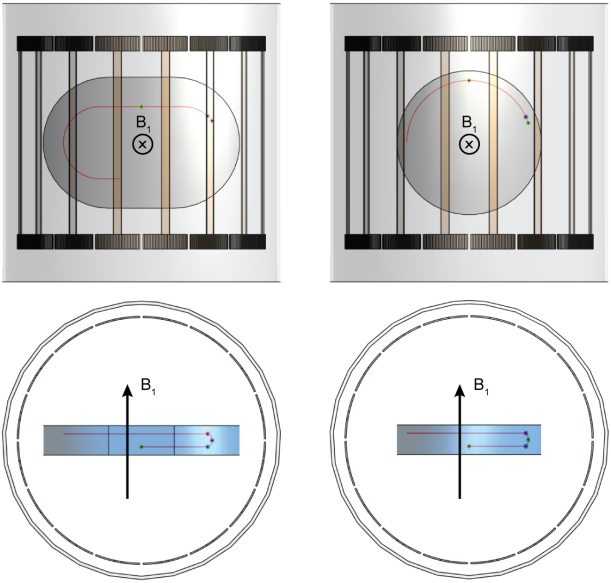

Figure 2.6: Two examples of radiated test experimental setup providing a phase-reversal incident condition to the implant. The implant routing paths are shown as red solid lines. The phase distribution of $E_{\tan}(l)$ of the phase-reversal incident conditions are illustrated in Figure 2.4a

In practice, this separation distance is limited to a small value to accommodate the finite size of the experimental phantoms. Depending on the electrical properties of the implants, the presence of the adjacent lead segment may have appreciable effects on P_{TIP}. We investigated this affect using full-wave CEM simulations of two 400-mm insulated wires positioned parallel to each other with a separation distance, d and are immersed in unbounded medium (ϵ_r = 78 and σ = 0.47 S/m). The implants are exposed to incident TEM waves with the electric fields polarized in the direction of the long axes of the leaded implants and the propagation vector perpendicular to the common plane of the implants' axes. Figure 2.7 illustrates P_{TIP} as a function of the separation distance, d. The results indicate that the scattering from the adjacent segment of a leaded-implant caused by a phase-reversal experimental configuration may significantly affect P_{TIP} when $d < 10\,\text{cm}$.

2.5 Summary

We have demonstrated that the experimental assessment of RF-induced heating of implant must be conducted under carefully designed test setup. Examples of two types of experimental evaluations were provided. First, we showed that the πX models obtained with an unoptimized experimental system (20 L phantom) lead to a significantly different prediction of the RF-induced heating of implants and the power deposition was estimated to be significantly less than the direct implant-RF CEM simulations and the numerically-derived πX models for the 800-mm implant. Alternatively, the estimated power deposition evaluated from the πX model obtained with the optimized experimental system (70 L phantom) has excellent agreement with those obtained from numerical solutions. Second, we demonstrated that radiated test configurations specified by provisional guidelines may not be suitable for all implants and their practical performance must be investigated prior to their implementation.

It is essential that the accuracy of the experimental methods and the instrumentation be assessed *prior to* their application to evaluated implant RF-induced heating performance. Admittedly, some inherent experimental uncertainties cannot be avoided, which is why optimizing the *in vitro* investigation is necessary to minimize the experimental uncertainties and to dismiss any potential false assumptions.

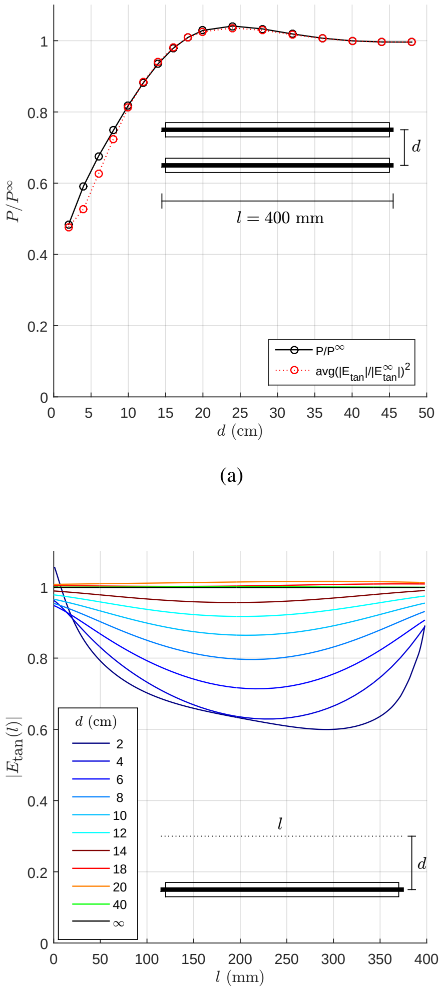

(a)

(b)

Figure 2.7: (a) P_{TIP} as a function of separation distance, d. The estimated power is illustrated with respect to P_{TIP} when only 1 lead is present, P_{∞}, is shown in black. The $|E_{\tan}(l)|$, averaged over the length of the implant, with respect to the average $|E_{\tan}(l)|$ when only 1 lead is present, E_{∞}, is plotted in red. (b) Estimated $|E_{\tan}(l)|$ to the lead due to the presence of a neighboring parallel lead at distance, d.

Part II

Review of State-of-Knowledge

Chapter 3

Electromagnetic MRI Safety with and without Implantable Metallic Devices: A Review

3.1 Abstract

[1] The image quality of magnetic resonance imaging is directly related to the strength, uniformity and quality of the static magnetic, low-frequency gradient and radiofrequency (RF) fields generated in the field of view by the scanner. The gradient fields can cause unwanted nerve stimulation and the RF fields localized thermal heating. The fields can also interact with implanted medical devices; potentially causing harm by displacement forces, localized temperature increase near the implant or malfunctions of active implants. Here, we provide a comprehensive review of the strength and distributions of the fields and the associated risks for the patients as a function of patient anatomy, imaging position, and exposure condition. In cases where the published data was insufficient, additional simulations were per-

---

[1] This Chapter has been published in [51]

formed. The review also includes a critical evaluation of the MRI safety related standards. All results can be directly applied by researchers and practitioners for specific hazard identifications.

3.2 Introduction

The discourse on safety of magnetic resonance imaging (MRI) exposure is long-lasting and started in the 1970s [4, 5, 6, 7]. After the U.S. Food and Drug Administration (FDA) reclassified MRI scanners from class III to class II devices in the late 1980s, market adoption accelerated and today there are approximately 50,000 scanners installed worldwide. The potential hazards intrinsic to the MRI environment have been evaluated and acknowledged [8, 9, 10, 11, 12, 13, 14, 15]. To avoid or mitigate adverse events, adequate MRI procedures and safety guidelines have been established [21, 22, 23, 24, 20]. Unfortunately, there are still numerous documented cases of accidents involving MRI scanners that have resulted in personal injury and even death, some of them due to metallic implant devices inside the human body [52, 53, 54, 55, 35]. Various additional potential hazards exist for a patient with conductive passive and active implantable medical devices (PIMD and AIMD) undergoing MRI scanning as they may strongly couple with the EM fields during the scan. Potential hazards include mechanical movement or dislodgment due to magnetic field induced forces and torques [15, 56]; damage to the circuitry of the device due to exposure to the EM [57]; and heating of the device and adjacent tissue due to radiofrequency (RF) energy absorption [29, 58, 30, 59]. Apart from the direct harm occurring during the scan, the MRI image can also be distorted around implants [60], compromising the accurate diagnostics and subsequent medical decisions. Ensuring a safe scanning environment is a continuous challenge for MRI radiologists and technicians as they have to weigh the benefit of a superior diagnostic against the risk assessments provided by both, MR scanner and PIMD/AIMD manufacturers. Although the potential safety issues and information for different implant types has been summarized and discussed [15, 25], the amount of biomedical implants and devices is steadily increasing; many of which have not been adequately tested with respect to MRI safety. Furthermore, the potential hazards of an implant depend on a variety of parameters, such as the MR system, patient anatomy, implant location, imaging position, exposure level, configuration, and duration. The exposure environment of the PIMD/AIMD thus needs to be investigated thoroughly to better understand the relative risks posed to the patient.

This review starts by outlining the standardization framework before providing a comprehensive overview of the EM fields relevant for the safety assessment of both patients with and without PIMD/AIMD. In cases where information in the literature on the RF fields was insufficient, additional simulations were performed to augment the knowledge of the EM field distributions. The discussions provide guidelines how the risks of different scanning conditions can be evaluated.

3.3 Standardization

MRI guidelines and safety standards have existed for many years. The three most influential documents covering patients without implants are (i) IEC 60601-2-33 [20], (ii) ICNIRP 2004 [19](with amendment of 2009), and (iii) FDA 2014 [18]. All of them involve very similar limitation approaches. The major differences are the head-averaged specific absorption rate (SAR) limit (i,iii: 3.2 W/kg; ii: 3.0 W/kg), the local SAR limit averaged over 10 g of tissue in the controlled mode (i: 20 and 40 W/kg; ii: 10 and 20 W/kg; iii: no explicit limits given), and the averaging time (i,ii: 6 min; iii: 10 and 15 min). Further, the latest edition of (i) does not apply the local SAR limit to volume coils, which effectively permits local SAR values far beyond 40 W/kg in case of body coils [61, 62]. Manufacturers generally comply with the most comprehensive product standard of IEC (i). Since 2015, IEC includes a so called ‘Fixed Parameter Option (FPO:B)’, designed for the compliant scanning of patients with implants. Yet, the main focus still remains on patients without implants.

As conductive PIMD/AIMD couple with the fields, which generally results in locally enhanced fields, additional safety evaluations must be performed when scanning patients with metallic implants. Two safety evaluations methods are currently applied ASTM F2182-11a [63] for PIMD and the more advanced methods of IEC/TS 10974 [1] for AIMD.

The ASTM F2182-11a [63] provides guidelines to assess tissue-heating near PIMD during exposure to the RF field in MRI. It is a primarily experimental assessment of the implant heating within a test phantom. While this is the most widely accepted safety assessment method for PIMD today, it is a greatly simplified proxy for the implant exposure in the patient. First, the test electric (E)-field in the phantom does not reflect the actual fields in the patient. Second, the permittivity and conductivity of the phantom material may substantially differ from actual tissue, especially for implants inside bone or fat (the surrounding tissue defines the electric lengths of the implant). Finally, larger implants may not properly fit the phantom, and are exposed to a non-uniform E-field, where the lateral decay-rate towards the front and back is depending on the scanner geometry.

Figure 3.1 illustrates the differences between a real patient and the homogenous test phantom as defined by the ASTM standard test method. The normalization to 2 W/kg phantom-averaged SAR results in much smaller delivered power than for a heavy patient. The local SAR can be seven times higher in the patient, and the square of the induced E-field more than 50 times higher. For typical implant routings inside the torso (such as pacemakers, evaluated later in this review), the average incident E-field remains below 150 V/m, which is similar to the field level in the ASTM phantom. However, for orthopedic implants (trajectories on the femur, ulna and clavicle were evaluated), the incident E-field can exceed 200 V/m. As these high E-fields tend to occur in fat-tissue (illustrated in Figure 3.1 for the thigh), it does not lead to high local incident SAR values, because of the low conductivity in fat. Therefore, relating the local incident SAR inside the ASTM phantom to the *in vivo* SAR (as suggested in 9.1 of the ASTM test method [63]) is a questionable approach, considering tissues can have very different dielectric parameters than the ASTM phantom material. In conclusion, even though the risk assessment using the ASTM is conservative for most PIMD, the risk might be underestimated for some implants. This underestimation could be addressed by introducing additional evaluations steps for high field implant locations, similar to those developed in IEC/TS/SD 10974.

The more recently developed standard IEC/TS/SD 10974 for AIMD overcomes the shortcomings of ASTM F2182-11a [63] and considers the actual induced fields in patients. The working group developing this standard assembles the expertise of the International Organization for Standardization (ISO) TC150/SC6 on AIMD and IEC SC62B MT40 on MR equipment for medical diagnosis. IEC/TS 10974 includes a Tier 4 approach that allows simplified evaluations for short implants while also including the most elaborated evaluations for complex AIMD. To eliminate the major shortcomings of the older ASTM standard, the same or an adopted approach could also be applied to PIMD.

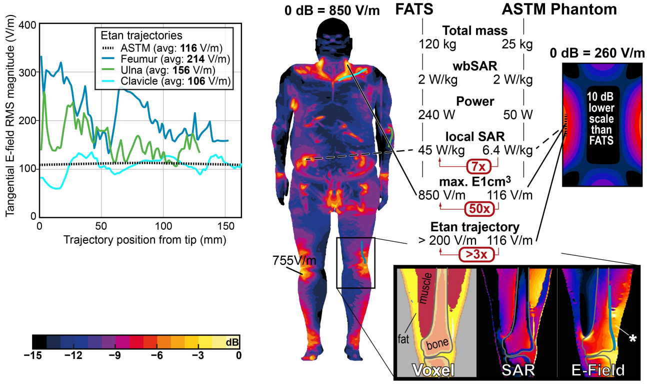

Figure 3.1: Induced E-field comparison (E1cm^3) between FATS (maximum intensity projection for all imaging positions) and the ASTM phantom (slice view at the vertical center, where the implant is placed). When both are normalized to a wbSAR of 2 W/kg, the local SAR is about a factor 7 higher in FATS, the maximum E1cm3 about a factor 7 in field (factor 50 in power). This large difference in the E-field is at least partially due to high E-fields in fat-tissues. Due to the low electric conductivity of fat, the difference is not reflected in the local SAR. When evaluating the tangential E-field (E_{tan}) along three orthopedic implant trajectories (evaluated for one imaging position each), E_{tan} can be considerably higher than in ASTM testing (factor $>$ 3 in power). Note the factor 3.3 (10 dB) difference in the scale normalization. The box illustrates the thigh region, where SAR is typically highest in muscle, but the E-field in fat ($*$).

3.4 Analysis of the PIMD/AIMD Environment

The fundamental components of the MRI system are usually composed of three parts: the strong static magnetic field (B_0), three orthogonal pulsed gradient magnetic fields (G_x, G_y, G_z) and the pulsed modulated radiofrequency magnetic fields (B_1). All three field components will be reviewed in the following paragraphs. In cases where the available data was considered insufficient, this information was added through additional simulations.

3.4.1 The Static Magnetic Field (B_0)

B_0 is a component of the MRI system that is continuously present. Most clinical scanners use superconducting magnets with cylindrical bores. 1.5 Tesla (T) and 3 T are the most commonly used scanners, with a few 7 T systems now approved for clinical use in humans [64]. A smaller number of ultra-high field MR systems in the range of up to 10.5 T are used in research institutions worldwide. The static magnetic field has the highest patient accessible magnitude at the iso-center of the MRI scanner, and the greatest patient accessible gradient usually at the edge of the MRI scanner bore, typically around 2 – 4 T/m.

3.4.2 The Gradient Field (G)

G in three orthogonal directions (x, y, and z-axis) are used for spatial MRI signal encoding. For a supine patient position, the x-axis would go from left to right, the y-axis would go from front to back, and the z-axis would go from head to feet. For applications that requires high-speed imaging (e.g., for functional MRI), higher gradient field change-rates are required. These time-varying fields will lead to induced E-fields and resulting currents within the body. For typical clinical MRI systems, the gradient field strengths are about 15 – 50 mT/m with maximum slew rates of 100 – 200 T/m/s within the field of view (FOV). Gradient fields in ultra-high field systems can be as high as 100 mT/m with slew rates of 800 T/m/s. Gradient coils are designed to generate highly linear gradients within the FOV around the iso-center of the scanner. Typical frequencies of these gradient fields are around 1 kHz, the spectral content of the gradient pulses can vary from 100 Hz – 10 kHz depending on the different sequences.

The induced E-field and current density strongly depend on the body geometry, the direction of the field gradient, and the distribution of tissue conductivity within the human body; various studies show that the y-gradient coil induces the largest E-fields in the body [65, 66]. The induced E-field shows a strong correlation with the local value of resistivity, and the induced current density exhibits strong correlation with the local tissue conductivity [66]. Therefore, people with high body mass index (BMI) and tissue with low conductivity (e.g., fat) tend to show the highest values of induced E-fields. Spatial discontinuities of the induced E-field will occur at the boundaries between tissues with different conductivity. Regions with high current density tend to occur in tissue with high conductivity (e.g., muscle).

3.4.3 Radio Frequency Fields B_1

The *in vivo* induced RF fields depend on many factors, such as the human anatomy, imaging positions, and RF coil geometry and design. In general, large patients with a high BMI, and imaging position around the abdomen tend to have higher induced E-fields inside the body. The RF coil length has a higher influence on the induced E-field than the coil diameter.

Field Level at the Exposure Limits

B_1 is applied at the Larmor frequency, which is proportional to the static magnetic field of the MR system. With about 43 MHz/T, the RF frequency is typically 64 MHz and 128 MHz at 1.5 T and 3 T, respectively. In conventional cylindrical bore systems, the main body coil is usually a birdcage coil designed to achieve a spatially uniform B_{1+} field (the rotational component of the B_1 field) in the FOV.

When investigating whole-body and local SAR without implants, the variation seen between different patients is a function of their anatomy and imaging position, with a strong influence of the trunk dimension on the induced eddy currents [67].

The current limitation scheme in the safety standard IEC 60601-2-33 [20] is based on separate limits in head-SAR (hdSAR), whole-body averaged SAR (wbSAR) and partial-body averaged SAR (pbSAR). As illustrated in Figure 3.2, hdSAR is typically reached first in head and neck imaging, wbSAR from neck to knee, and pbSAR for below the knee. For the depicted normal operating mode, pbSAR is less relevant than in first level controlled mode, where pbSAR is often reached already from below the pelvis [62]. In this review, we focus our evaluations on the normal operating mode for circular polarization (CP), as MRI examinations for patients with PIMD/AIMD are typically limited to this configuration.

Figure 3.3 shows the allowed $B_{1+,\,\mathrm{rms}}$ values for the normal operating mode. $B_{1+,\,\mathrm{rms}}$ was derived by spatially averaging B_{1+} over the central axial slab of the patient, as suggested in the IEC standard [20]. The root-mean-square (rms) refers to the temporal average over the pulsed RF sequence of the scanner. In leg imaging, especially below the knees, very large $B_{1+,\,\mathrm{rms}}$ values of up to μT (1.5 T) and 10μT (3.0 T), respectively, would be allowed

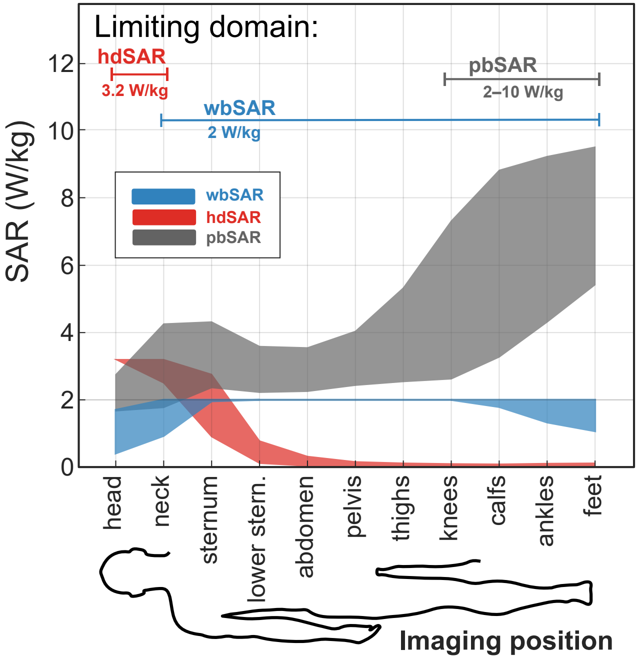

Figure 3.2: Total minimum-maximum spread of SAR levels reached in the normal operating mode for Virtual population (ViP) model FATS (obese phantom) and THELONIOUS (child phantom), at 1.5 T and 3 T in more than seven different body-coil geometries, covering all major MRI bore sizes. The hdSAR limit is always reaches first in head imaging; the wbSAR is always reached first from sternum to knee imaging. In the neck imaging position, the limit for either hdSAR or wbSAR can be reached first, depending on the patient and body-coil geometry; the same applies to imaging below the knees for wbSAR and pbSAR. The actual pbSAR limit is between 2–10 W/kg, depending on the exposed partial body mass. Exposure is in CP only (no RF shimming).

by the standard. However, most manufacturers are not exploiting this region due to RF amplifier limitations and safety considerations. Clinical experience shows that scans with $B_{1+,\,\mathrm{rms}}$ values above 6 μT (1.5 T) and above 3 μT (3 T) can typically not be configured on human scanners. The AIMD-specific FPO:B mode [20] defines a maximum $B_{1+,\,\mathrm{rms}}$ of 3.2 μT at 1.5T. Implant manufacturers typically label their implants to the maximally allowed SAR, but $B_{1+,\,\mathrm{rms}}$ labeling is becoming more frequent as well.

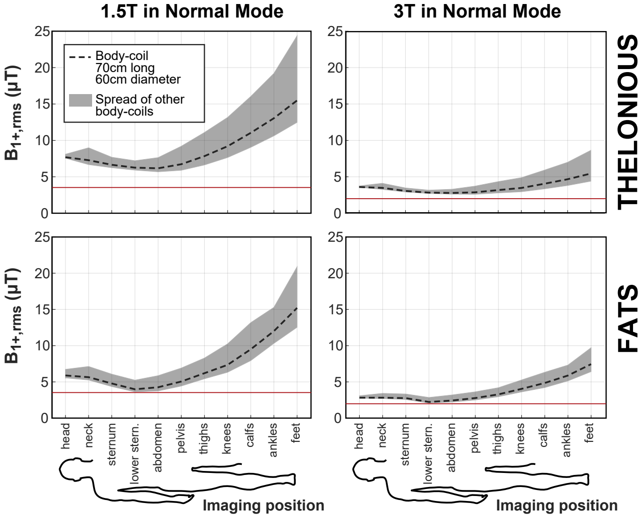

Figure 3.3: Total minimum-maximum spread of allowed $B_{1+,\,\mathrm{rms}}$ values to reach the normal operating mode limit for FATS and THELONIOUS at 1.5 T and 3 T in seven different body-coil geometries. The body-coil with 70 cm length and 60 cm diameter is indicated as dashed line, as we performed other evaluations with this geometry only. The spread includes coil lengths between 40–70 cm, with diameters between 60–75 cm. A minimum of 3.5μT (1.5 T) and 2μT (3.0 T) can be applied regardless of model, imaging position, and body-coil geometry, in the normal operating mode (red horizontal lines).

Induced E-field as Incident Field for the PIMD/AIMD

The heating around PIMD/AIMD predominantly depends on the induced tangential E-field along the implant (E_{tan}). Instead of performing simulations with the implant present — which results in divergently many placement and configuration permutations — the exposure can be approximated by decomposition into (i) the incident field to the implant, without the implant present, and (ii) the local field enhancement near the implant as a function of this incident field. This approach is used in Tier 1–3 of the technical specification ISO10974 [1], while the full simulation including the implant is called 'Tier 4'. The incident field for two different anatomical models is illustrated in Figure 3.4. The visualization shows the E-field averaged over cubes of 1 cm^3 (E1cm^3), which results in a reasonable distribution given that the heating-relevant implants are larger than 1 cm. A maximum intensity projection has been chosen to visualize all 'hotspots' in a single plane, and to combine various imaging positions. For example, the 'upper torso' in Figure 3.4 shows the maximum E-fields for the imaging positions from upper sternum to upper abdomen, vertically projected through the anatomical model.

In addition to the incident E-field distribution, the E_{tan} average along typical AIMD trajectories are shown in Figure 3.5. The evaluated routings are shown in Figure 3.4 for a deep brain stimulator (DBS), a pacemaker (PM), and a spinal cord stimulator (SCS).

From Figure 3.4 we can visually estimate that the AIMD routings for the PM and SCS are only marginally exposed for head/neck and leg imaging. DBS routings on the other hand have low E-fields in lower torso and leg. This visual estimation is confirmed by the actual E_{tan} evaluations of the three implant-categories in Figure 3.5.

When diverging from circular polarized (CP) to elliptical or linear polarization (as typically applied in 2-port RF shimming at 3 T), the maximally induced E1cm^3 magnitude can change by up to about ± 3 dB (approximately factor 1.4 in E-field), similar to the evaluation for the 10g-average SAR [62]. As the E_{tan} along the trajectories of PIMD/AIMD includes more localized and directional E-field components, the difference between CP and RF-shimming can be up to +6 dB (factor 2 in E-field, as shown in Figure 3.5), or—in the case of favorable RF shimming—mitigated by -30 dB (factor 33 in E-field; factor 1000 in induced power). To avoid the potential +6 dB enhancement, most implant manufacturers restrict the RF exposure to circular polarization in their PIMD/AIMD labeling.

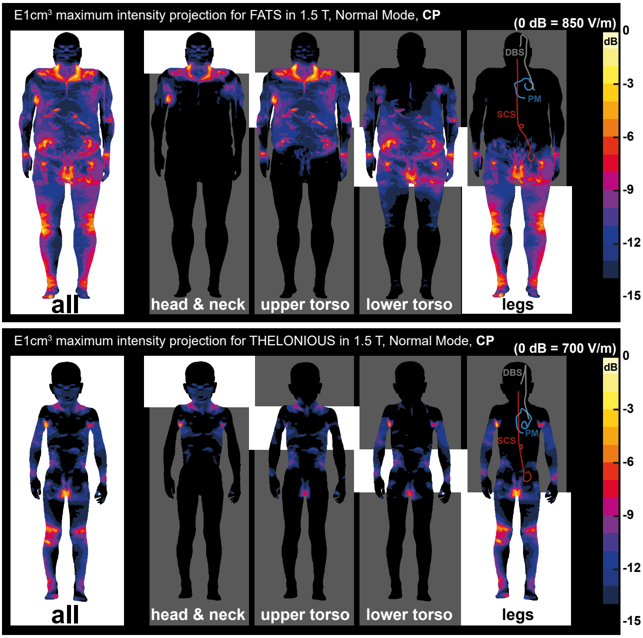
E1cm³ maximum intensity projection for FATS in 1.5 T, Normal Mode, **CP**
(0 dB = 850 V/m)
dB
0
-3
-6
-9
-12
-15
DBS
PM
SCS
all
head & neck
upper torso
lower torso
legs
E1cm³ maximum intensity projection for THELONIOUS in 1.5 T, Normal Mode, **CP**
(0 dB = 700 V/m)
dB
0
-3
-6
-9
-12
-15
DBS
PM
SCS
all
head & neck
upper torso
lower torso
legs

Figure 3.4: Maximum intensity projection of the induced E-field averaged over 1 cm^3 for FATS (top) and THELONIOUS (bottom). The maximum is projected orthogonal to the depicted plane and for the various imaging positions highlighted in white. Typical routings or AIMDs (DBS, PM, SCS) are shown on the very right images. Note the different dB-scale-reference for FATS and THELONIOUS.

Typical Hotspot Locations

The induced Eddy currents increase with radial distance from the patient center, and are altered by local anatomical features such as dielectric contrasts between different tissues or constrictions. We identified seven typical E-field hotspots, where substantial field enhancements occur due to the intrinsic human anatomy. The seven locations can be further classified to four

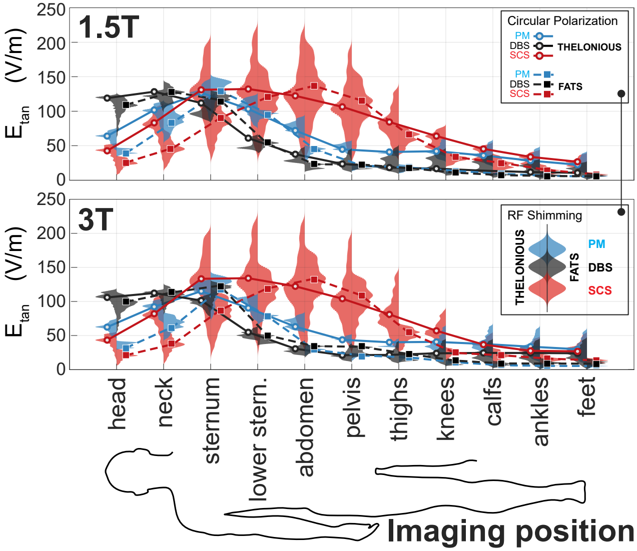

Figure 3.5: Tangential E-field (E_{tan}) magnitude average along the predefined implant routings shown in Figure 3.4. The patches show histograms obtained for different exposure polarizations (RF shimming), the lines represent the corresponding value obtained with CP exposure. All values normalized to the normal operating mode. The worst-case polarization typically shows up to a doubled E_{tan} compared to CP.

underlying patterns of (i) lateral enhancement due to higher lateral Eddy currents, (ii) dielectric contrast, (iii) anatomical body-constrictions, and (iv) tissue-constrictions around bones. Figure 3.6 illustrates these hotspot locations.

3.5 Brief Review of Risks without PIMD/AIMD

The complex EM exposure of patients during MRI scans is one of the highest people of the general population may be exposed to. Other high-field medical applications include targeted tissue heating (e.g., EM dia- and hy-

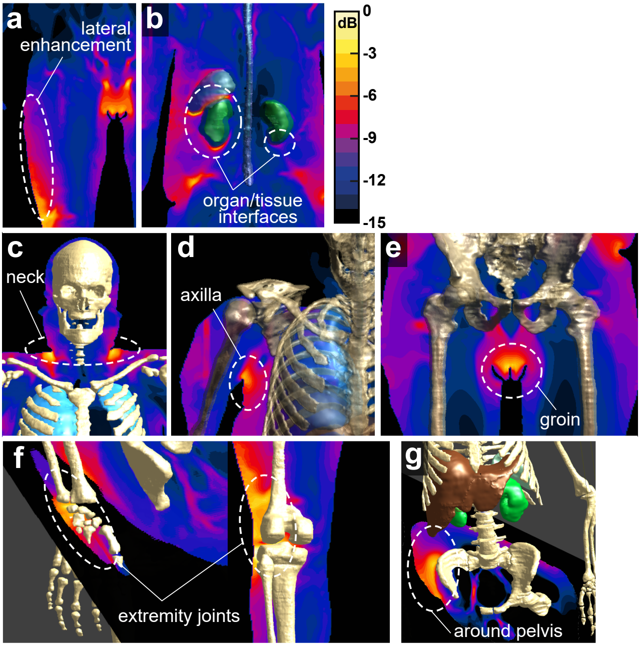
a
lateral enhancement
b
organ/tissue interfaces
dB
0
-3
-6
-9
-12
-15
c
neck
d
axilla
e
groin
f
extremity joints
g
around pelvis

Figure 3.6: Seven identified typical E-field hotspot locations. *Lateral Enhancement:* (a) shown for the thighs, exists also for the lateral torso and arm. *Dielectric contrast:* (b) pronounced effect around the inner organs. *Anatomical body-constrictions:* (c) around the neck towards the shoulders, (d) axilla, and (e) groin. *Tissue constriction around bones:* (f) shown for the wrist and knee, also exists in the other extremity joint of the elbow and ankle, (g) around the pelvis bone.

perthermia) or nerve excitations (e.g., transcranial magnetic stimulation). The accepted field levels in MRI are about 10 times higher than the limits in occupational exposures, and 50 times higher than general public exposure limits [16]. Risk-Benefit considerations based on clinical indications resulted in standardized exposure limits close to physiological limits. Thus, even in the absence of PIMD/AIMD and in full compliance with the standardized limits, MRI may result in risks to the patient having special health conditions with potentially compromised thermoregulation abilities (e.g., diabetes).

Static fields can induce vertigo, nausea, and a metallic taste in the mouth [20], but are generally well tolerated by living matter. The highest risk are ferromagnetic objects that are drawn into the MRI bore, potentially injuring the patient.

The switching rates of the gradient fields can induce peripheral nerve stimulation (PNS). The limit for the first level controlled operating mode is set at the threshold for PNS. Thus, the patients may report some sensations of pressure, tingling, or muscle twitching. However, the threshold for potentially fatal cardiac stimulations is consistently higher than for PNS, and the gradient fields therefore do not pose significant risks.

The RF exposures from the B_1 field may lead to considerable thermal load with the risk of (i) systemic core-temperature heating and (ii) localized heating or burns. The risk is typically higher in tall and obese patients as they have a smaller surface-to-weight ratio with subsequently lower heat-dissipation ability for the same whole-body averaged exposure, and the localized exposure is higher due to the higher body-cross-section [67]. In addition, local contact-burns can occur for highly localized field enhancements. This usually originates from incorrect placement of the patient, by forming so-called ‘RF-loops’ (e.g., hand-hip touching, or ankle touching), or by placing parts of the patient in direct contact to the inner bore-surface near capacitive elements of the body-coil.

Despite the very high EM exposures during MRI imaging, the history of use for patients without PIMD/AIMD within the past 30 years has proven MRI to be a remarkably safe modality, with only a few incidents per million scans [68]. Human thermoregulation has strong capacities to counteract the thermal load of MRI examinations [69]. It also should be pointed out that all MRI manufactures have implemented additional safety margins such that the actually reached systemic and local exposures in the patient are considerably lower than defined by the standard. Thus, the history of safe use only reflects the actual exposure levels, which are presumably more than 30% lower than the guideline limits.

3.6 Review of Risks with PIMD/AIMD

Most PIMD/AIMD today are non-ferromagnetic, e.g., made from titanium or stainless steel (which is usually non-ferromagnetic, despite the high iron-content). Ferromagnetic implants would experience very strong torque and displacement forces by the static magnetic field. This section therefore focuses on the potential risks posed from non-ferromagnetic or slightly ferromagnetic materials. Table 1 summarizes the MRI-related hazards, as addressed by the technical specification ISO/TS 10974 [1].

Table 3.1: Potential patient hazards and corresponding test methods list in ISO/TS 10974 [1]. In this review, we classify the hazard into mechanical, malfunction, and thermal, and add the image distortion as a potential indirect harm.

Category	General hazard	Test method	Clause
Thermal	Heat	RF field-induced heating of the AIMD (device and electrodes)	8
		Gradient field-induced device heating	9
Mechanical	Vibration	Gradient field-induced vibration	10
	Force	B_0-induced force	11
	Torque	B_0-induced torque	12
Malfunction	Extrinsic electric potential (unintended stim)	Gradient field-induced lead voltage	13
	Rectification (unintended stim)	RF field-induced rectified lead voltage	15
	Malfunction	B_0-induced device malfunction	14
		RF field-induced device malfunction	15
		Gradient field-induced device malfunction	16

3.6.1 Mechanical Risks

Translational and torque forces can be exhibited on non-ferromagnetic metallic implants by the static magnetic field (B_0) through induced Eddy currents, known as the ‘Lenz effect’ [70, 71]. Any change in magnetic flux density through a metallic loop causes induced currents, which result in a force opposing to the applied force. This can be felt as a sort of ‘nertia’, counteracting rapid motion. The translational force is highest, where a strong B_0 gradient exists (near the magnet portal). The torque force, in contrast, is highest in an area with the strongest B_0 (near the center of the magnetic bore). Eddy current torque has been reported for metallic heart valves [70], but it is not believed to pose an MRI safety issue for most other PIMD/AIMD.

Mechanic vibrations can be caused by the gradient fields (G), with vibration-frequencies in the kHz region. This cannot result in any direct mechanical damage to the patient's tissues or organs, but could trigger device malfunction [27], as discussed later in this review.

3.6.2 Risks Due to AIMD Malfunctions

The complex EM fields of the MR system can interfere with AIMD and cause malfunction or change operational functions. The B_0 field could interact with device switches, alter the sensed electrocardiogram, e.g., of defibrillators, or saturate transformer core materials. The pulsed gradient field (G) could also interact with device switches, and additionally lead to inappropriate sensing and triggering because of the induced voltages. The latter is also true for the pulsed RF fields (B_1), which can be de-modulated by non-linear electronic elements, which results in signals in the kHz-region [28, 72, 73, 74].

A particular concern arises for AIMD deliberately tuned to receive RF radiation. One example is the cochlear hearing restoration implant [75, 76], where the auditory input is transmitted as RF signal. The significant coupling between the MRI RF field and such implants raises the possibility of very high currents being generated in implant with deleterious effects to the implant and injury to the patients [25].

3.6.3 Risks Due to Thermal Effects

Local tissue heating is a well-known safety concern for people with implants undergoing MRI. Dempsey et al [77] reviewed numerous reported burn injuries sustained during MRI and addressed the underlying heating mechanisms possibly causing these events. A permanent injury caused by a deep brain stimulator during MRI is documented [77], and reports on increased pacing thresholds in patients with pacemakers after MRI indicate local tissue heating and scar formation around the lead tip [78, 79].

A potential heating hazard may originate in some cases from gradient (G)-induced heating [80]. Simple direct electromagnetic induction causes Eddy currents in conductive loops, which subsequently results in device heating, especially in large pulse generator devices of AIMD or orthopedic metallic meshes, which encompass large 2D loops.

The major concern, however, is generally associated with RF-induced heating [77, 81]. AIMD with elongated isolated lead structures can become resonant resulting in large currents on the lead [82], high localized power depositions in the tissues at the electrodes or considerable voltages at the lead terminals. In IEC 10974, the piece-wise excitation methodology[49, 83] was developed to determine the deposited power at the electrodes or at terminals inside the pulse generators for any excitation. Other mechanisms for electrically short implants have been proposed and numerically validated [84], where the metallic implant acts as short-circuit between the two endings of the implant.

The amount of actual power deposition in tissue depends on many clinical factors such as patient anatomy; imaging position; lead configuration, position, and orientation; exposure level in terms of the E-field amplitude and phase along the implant; RF frequency; and tissue properties at the implant ending. The resulting temperature increase also depends on e.g., the thermal tissue properties, rate of blood perfusion, and RF absorption distribution. Careful selection of the clinical exposure scenario and proper RF-shimming [48] can substantially reduce potential heating hazards in the patient.

Lastly, the actual thermal tissue damage is not only a function of the reached temperature, but also of the exposure time. The thermal dose (for example assessed via cumulative equivalent minutes at 43°C, CEM43 [85]) correlates best with tissue damage. However, due to the highly localized exposure around PIMD/AIMD, the heating can be orders of magnitude higher than for patients without implants. The initial temperature increase over several degrees Celsius can be too fast ($< 2\,\mathrm{min}$) for local thermoregulation to initiate, which allows even higher temperatures to be reached than for slower heating profiles.

3.6.4 Risks Due to Image Distortion

In addition to the direct harm caused by the electrical medical device, the MR image may be distorted by electrically conductive materials. This is caused by the disruption of local B_{1+} field homogeneity. The degree of the image distortion depends on the magnetic susceptibility, configuration and position of the device, as well as the MR sequence used and strength of the magnetic fields in the MR system. The image distortion can considerably affect the diagnostic accuracy of MRI, particular if the medical device is implanted close to the area of interest (e.g., in cardiac or breast imaging).

3.7 Discussion and Conclusions

This paper provides a comprehensive review about the induced fields and the associated risks in patients with PIMD/AIMD undergoing MRI scans, including current standards. It specifically illustrates the typical hotspot regions, which may help to assess the safety for specific high-exposure implant locations. Figure 3.4 allows to quickly assess potentially harmful implant locations and configurations, and identify safe patient imaging positions, when a problematic implant has a certain distance to the region of interest. For example, in all leg imaging positions (Figure 3.4 on the very right), any pacemaker or DBS devices are essentially not exposed, while the SCS routing still encompasses some high-field regions. This is confirmed by the E-field average evaluated in Figure 3.5. The actual magnitude for a specific routing may still be considerably lower than seen in Figure 3.4, because E_{tan} only considers one spatial component and the routing does not necessarily encompass the highest values shown in the maximum-intensity projection.

We have also compared the induced fields considered for the ASTM test method compared to the more advanced IEC/TS 10974. It has been shown that the fields induced in the ASTM phantom have very little correlation with the fields induced in patients but is historically applied as a conservative testbed for PIMD. Figure 3.1 also shows that it not conservative in all cases. The scaling of the results to the local SAR in patients is also questionable for low conductivity tissues. All listed shortcomings could be overcome if the concept developed for IEC/TS 10974 would be adopted for PIMD.

Restriction to CP prevents a potential +6 dB enhancement originating from RF shimming, which is therefore often required by the implant label. On the other side, it also prevents a potential mitigation by using a favorable RF shimming configuration. The identified hotspot locations may serve as initial assessment of implant safety. If the target site of an implant is close to such a region, refined safety considerations may be necessary.

Over the last decades, considerable efforts have been put into understanding the interaction between implanted medical devices and the hostile electromagnetic environment inside MRI scanners. Several implants have received FDA or EMA labeling as MR conditional devices. As both the

MR technology and biomedical implant devices are being further developed, new potentially hazardous situations in patients with implants may arise, e.g., due to multi-transmit or high-field scanners. On the other hand, implant specific scanning protocols may be utilized that can substantially reduce the induced current on the implants. In view of the growing complexity and legacy of some devices, it is important to simplify and clarify the MR labeling of medical implants, to support MRI radiologist and operators in reducing the potential risks for patients.

Part III

in vitro Experimental Methods

Chapter 4

Novel Test Field Diversity Method for RF Transfer Function Validation Required for Demonstrating MRI Safety of Active Implantable Medical Devices

4.1 Abstract

[1] **Purpose**: Radio frequency (RF) safety of elongated active implantable medical devices (AIMD) during magnetic resonance imagining (MRI) requires an RF response model of the implant. The model must be validated in a sufficiently large set of incident tangential electrical field (E_{tan}) condi-

---

[1] This Chapter has been published in [86]

tions that provide diversified exposure. Until now, this procedure was very time consuming and often resulted in poorly defined E_{tan} conditions. In this paper, we propose the novel test field diversity (TFD) validation method providing more diverse exposure conditions of high fidelity, thereby decreasing the number of implant routings to be tested.

Methods: The TFD method is based on the finding that the amplitude and phase of E_{tan} along a single lead path in a cylindrical phantom can be sufficiently varied by changing the polarization of the incident 64 and 128 MHz magnetic field inside standard test birdcages, respectively. The method is validated, an uncertainty budget is developed, and its benefits are demonstrated.

Results: First, the numerically determined field conditions were experimentally verified. The RF transfer function of a 90 cm long spinal cord stimulator was successfully validated using the TFD approach and excitation conditions that cover a $>$10 dB dynamic range of enhancement factors (for identical trajectory-averaged incident field strength).

Conclusion: The new TFD method yields an improved and reliable validation of the AIMD model with low uncertainty, i.e., $<$1.5 dB, for 1.5 and 3.0 Tesla evaluations, respectively. The results demonstrate that the test configurations can be further reduced without compromising the rigidness of the validation.

4.2 Introduction

To assess the risk of the radiofrequency (RF) electric (E) field induced in patients with active implantable medical device (AIMD) during magnetic resonance imaging (MRI), a four tiers approach has been defined in ISO/TS 10974 [1, 87]. The four tiers are designed such that the resulting overestimation of the local deposited power (or temperature rise) in tissue, due to the presense of an AIMD electrode, is decreased with increasing tier number. However, tiers with higher numbers requires a more and more complex and elaborated evaluation. For example, Tier 1 and Tier 2 represent the least complex test methods, but are based on the local maximum absolute exposure and produce the most conservative results. They are, therefore, only suitable for electrically short implants for which an overestimation of the risk is acceptable. The highest tier, Tier 4, requires the full simulation of all relevant clinical scenarios (including modeling of the patient, RF coils, and AIMD) and, accordingly, provides the most accurate estimation. Even today, Tier 4 is computationally expensive, as most commercial leads require μm discretization in a computational domain of several meters (i.e., days of simulation time for one clinical scenario using high performance computers). Therefore, this approach is practical only for very short (e.g., cochlea implants) or passive implants in limited clinical scenarios. On the other hand, the *in vitro* investigation of AIMD with long leads experimentally [88, 33, 37, 89] is cumbersome and does not take into consideration the inhomogeneity of the human body tissues. Therefore, the only practical tier for the evaluation of AIMD with elongated leads is currently Tier 3.

Tier 3 is designed to alleviate the computational burden of Tier 4 by splitting the evaluation into two steps. In the first step, the entire range of *in vivo* exposure conditions of the AIMD in patients is obtained *in silico*, i.e., by simulations. For typical implants, such as pacemakers or spinal cord stimulators, this includes millions of individual exposure conditions composed of combinations of RF coils that represent all installed geometries, polarizations of the magnetic field, varying patient anatomies in different postures and imaging positions, as well as clinical lead trajectories. These exposure conditions are evaluated as tangential electric fields ($E_{\text{tan}}(l_1)$) along the implant length. In the second step, the AIMD RF transfer function model for each electrode of the AIMD [49] is created independently according to Tier 3 [1]. The transfer function describes the scaling amplitude and phase of the E-field in the tissue close to an electrode of the implant for very local piecewise tangential field excitations along the AIMD (Section 8.4). The combination of both the exposure condition E_{tan} and the AIMD RF transfer function, together with knowledge about the local tissue properties, enables the determination of the local power deposition or local temperature increase. As the results directly depend on the quality of the AIMD RF transfer function, its conclusive and robust validation plays a key role for the reliable and accurate power deposition estimation.

To date, validation tests generally comprise a test phantom filled with tissue simulating medium (TSM) in which the AIMD is submerged. To achieve multiple distinct E_{tan} characteristics, different combinations of phantoms and implant routings are commonly used during the validation process [1, 90], the objective of which is to verify by measurements the values of local deposited power as estimated with the AIMD RF transfer function model. However, the number of achievable distinct sets of incident fields E_{tan} is limited, due to the long AIMD length ($>$50 cm) and the limited phantom size. Moreover, the separation distance from the phantom walls and between AIMD segments needs to be considered to minimize the influence from phantom boundary reflections and scattering at adjacent AIMD lead segments [46]. These considerations add constraints on the implant placement during the test procedure and reduce the achievable diversity of E_{tan} (e.g., less than four distinct E_{tan} are available for an AIMD with a lead length of 90 cm under circularly polarized exposure). In addition, testing time and characterization efforts increase with the number of test configurations for methods using different combinations of phantoms and routings (more than one hour per test configuration). Furthermore, remounting of the implant during each test configuration introduces extra positioning uncertainties.

In order to achieve an improved scheme for the AIMD RF transfer function validation, we propose a way of gaining E_{tan} diversity through manipulation of the RF coil exposure instead of the implant geometry. In this paper, the test field diversity (TFD) method is applied to long AIMDs (Section 8.4) to establish a set of transfer function validation tests that benefits from high test condition diversity and fidelity along the AIMD. The TFD derives directly from the idea of RF shimming [91] used to control the electric field distribution inside a birdcage RF coil. The incident field distribution can also be manipulated using more sophisticated and difficult to implement techniques, like the employment of passive scatterers, such as passive resonant RF coils, that could be placed at various locations around the phantom or dielectric shimming [92, 93].

4.3 Methods

The TFD method is designed to validate an independently determined AIMD RF transfer function with a minimal physical set of routings inside a phantom filled with TSM, by changing the polarization of the incident field radiated from the MRI birdcage test system (i.e., diversifying the exposing E_{tan}).

Parameters used to characterize the field polarization ellipse are introduced in Section 4.3.1. The incident condition definition is explained in Section 4.3.2. A dedicated exposure setup for validation has been established and is described in Section 4.3.3. Section 4.3.4 summarizes the application of the TFD method for the validation of an implant RF transfer function, using a 90 cm spinal cord stimulator lead as an example implant under test (IUT).

4.3.1 Polarization Ellipse

The polarization state of any electromagnetic wave can be represented as a tilted ellipse with different ellipticity (roundness) and tilt angle. Figure 4.1(a) illustrates a typical elliptical polarized magnteic field ($\vec{H}$) in right-hand rotation, where two parameters (ϵ and τ) are defined to characterize the ellipticity and tilt angle of the field polarization [94]. The ellipticity (ϵ) is defined as:

$$\epsilon = \alpha \cdot arccot(AR) \tag{4.1}$$

where AR is the axial ratio of the polarization ellipse, defined to be the ratio of the major axis (signed) magnitude of the polarization ellipse to the minor axis one. α indicates the rotation of the polarization ellipse, $\alpha = 1$ for left-hand rotation, $\alpha = -1$ for right-hand rotation. For instance, for left-hand circularly polarized fields, ϵ = 45°; for right-hand polarized fields, ϵ = -45°; for linear polarized fields, ϵ = 0°. Figure 4.1(b) illustrates the polarization states of electromagnetic (EM) fields in the (ϵ,τ) space.

4.3.2 Incident Condition Definition

Based on the superposition principle of the Maxwell equations the combined magnetic field for birdcage RF coils with N individual channels can be expressed as:

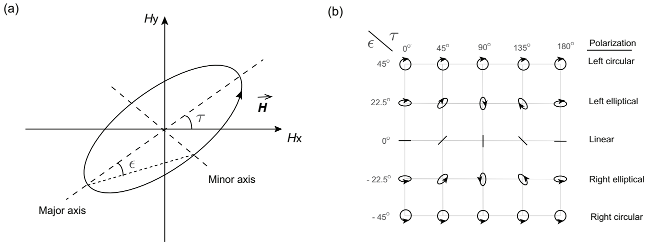
(a)
Hy
$\vec{H}$
Hx
τ
ε
Minor axis
Major axis
(b)
ε τ
0°
45°
90°
135°
180°
Polarization
45°
Left circular
22.5°
Left elliptical
0°
Linear
- 22.5°
Right elliptical
- 45°
Right circular

Figure 4.1: (a) The polarization ellipse of the magnetic fields $\vec{H}$, $\vec{H}$ can be decomposed to two orthogonal component of $\vec{H}_x$ and $\vec{H}_y$. ϵ and τ are two parameters used to characterize the ellipticity and tilt angle of the ellipse. (b) Selected polarization states of $\vec{H}$ fields as a function of ϵ and τ.

$$\vec{H}_{total} = \sum_{0}^{N} (\vec{v}_i)\vec{H}_i \tag{4.2}$$

where $\vec{v}_i$ and $\vec{H}_i$ are the complex driving coefficient and magnetic field of channel i, respectively. For RF coils with two orthogonal channels (channel x and channel y):

$$\vec{H}_{total} = \vec{v}_x\vec{H}_x + \vec{v}_y\vec{H}_y \tag{4.3}$$

For tangential E-fields along a certain implant $\vec{E}_{\text{tan,x}}$ and $\vec{E}_{\text{tan,y}}$ (for the x and y channels) the total tangential E-fields can be expressed as:

$$\vec{E}_{\text{tan,total}} = \vec{v}_x\vec{E}_{\text{tan,x}} + \vec{v}_y\vec{E}_{\text{tan,y}} \tag{4.4}$$

However, to ensure that RF-heating enhancement factors remain comparable (a requirement when selecting diversified $\overline{E_{\text{tan}}}$ exposure conditions), the exposure magnitude is scaled such that $|\vec{E}_{\text{tan,total}}| = 1$, namely,

$$\vec{E}_{\text{tan,total}} = (\vec{v}_x\vec{E}_{\text{tan,x}} + \vec{v}_y\vec{E}_{\text{tan,y}})(\overline{|\vec{v}_x\vec{E}_{\text{tan,x}} + \vec{v}_y\vec{E}_{\text{tan,y}}|})^{-1} \tag{4.5}$$

where the overline denotes the value of a quantity averaged along the AIMD trajectory.

4.3.3 Exposure Systems

Two exposure systems were used for the experimental assessment. (i) a 64 MHz birdcage (length = 65 cm, diameter = 70 cm) (MITS1.5, ZMT Zurich MedTech AG, Switzerland) with an iso-symmetrically loaded 44 cm-diameter cylindrical phantom filled with tissue simulating liquid ($\epsilon_r = 78$, $\sigma = 0.47$ S/m) to the height of 19 cm, and (ii) a 128 MHz birdcage (length = 50 cm, diameter = 70 cm) (MITS3.0, ZMT Zurich MedTech AG, Switzerland) loaded with the same phantom. The Q-I ports can be driven with RF square pulses with 40% duty cycle over a wide range of phase differences and amplitude ratios.

Two implant routings are established with the following design goals: (i) minimal reflections from truncated boundaries, (ii) minimal scattering between two parallel segments of the implant leads, and (iii) supporting implant lengths up to 90 cm. This ensures at least 5 cm separation between the implant body to any truncated boundaries and at least 10 cm separation between parallel segments of the implant as determined by [46]. Different polarization states of the B_1 field are achieved by controlling the driving vectors of the two-port RF coils, which, are monitored by two optical magnetic field probes H1TDSx/MR (SPEAG, Zurich, Switzerland) with a frequency range of 10 MHz to 6 GHz and a dynamic range of 120 dB at 1 Hz resolution bandwidth. The accuracy in amplitude and phase is better than 0.4 dB and less than 3%, respectively. Figure 4.2 illustrates the test setup and the two implant routings used in this work.

To validate the exposure system, the RF-coils are driven to achieve three reachable polarization states: P1 (left circular polarization), P2 (linear polarization), and P3 (right circular polarization). The spatial distributions of the total electric field over the plane where the IUT will be located are experimentally verified by measuring the field components with the near-field pseudo-vector electric field probe EU2DV3 (SPEAG, Zurich, Switzerland) [95]) and compared with values obtained from full-wave simulations of the exposure setups with the Sim4Life software platform (ZMT Zurich MedTech AG, Switzerland). The unique probe design enables to accurately determine the polarization ellipse and the magnitude of the induced fields. The linearity of the probe is ± 0.2 dB with a dynamic range of 10 V/m to 1000 V/m and the sensor positioning uncertainty is less than 0.3 mm. The deviation between experimental and numerical evaluations of the total electric field was found to be less than the total (simulation and measurement)

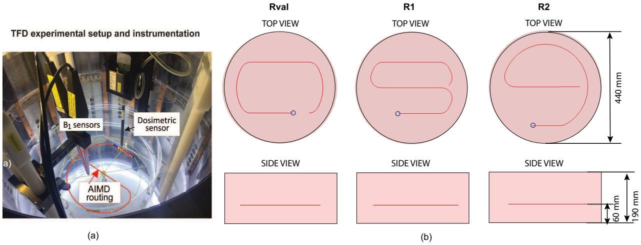
TFD experimental setup and instrumentation
B1 sensors
Dosimetric sensor
AIMD routing
a)
Rval
R1
R2
TOP VIEW
TOP VIEW
TOP VIEW
440 mm
SIDE VIEW
SIDE VIEW
SIDE VIEW
60 mm
190 mm

(a) (b)

Figure 4.2: (a) TFD experimental setup and instrumentation. (b) Top view and side view of the predefined implant routings Rval, R1, and R2 (see Figure 2a) that ensure at least 5 cm separation distance between IUT and phantom boundaries, and 10 cm between parallel lead segments. Rval is used for calibration, R1 and R2 are for validation test. The location of the distal termination of an IUT is indicated by a blue ”o” marker. Only the lead routings are shown here; the leads are connected to the implanted pulse generator (IPG) when placed in the setup, in the same way they are connected when the AIMD RF transfer function is obtained.

combined standard uncertainty of 0.2 dB (k=1).

4.3.4 Tier 3 RF Transfer Function

To characterize the implant-RF interaction, the transfer function concept is introduced in Tier 3 of ISO/TS 10974 to determine the RF-induced heating [1, 49]. Figure 8.3 illustrates the Tier 3 RF transfer function of the IUT at 64 MHz and 128 MHz, respectively, derived in homogeneous TSM according to the piecewise excitation method described in [83]. The principal assumption of the method is that the total induced field at an electrode is the superposition of the induced field contributed by local excitations along the implant [49]. Therefore, the method offers a sound strategy to determine the total RF-induced power deposition resulting at each electrode from any arbitrary incident field condition.

If we normalize the Tier 3 RF transfer function $h(l)$ magnitude such that

$$1 = \left(\int_0^L h\,(l)dl\right)\left(\int_0^L h\,(l)dl\right)^* \tag{4.6}$$

the RF-heating enhancement of the IUT can be expressed as:

$$P_{\text{dep}} = P_0 \left(\int_0^L h\,(l)\,\vec{E}_{\text{tan}}\,(l)\,dl\right)\left(\int_0^L h\,(l)\,\vec{E}_{\text{tan}}\,(l)\,dl\right)^*, \tag{4.7}$$

where P_{dep} is the power deposition of the IUT under the incident E_{tan} defined in (4.4) and P_0 (W/(V/m)^2) is the power deposition of the IUT under unit iso-electric incident field ($\vec{E}_{\text{tan}}(l) = 1e^{j\phi_0}$ V/m, where ϕ_0 is a constant). $\vec{E}_{\text{tan}}(l)$ is the tangential electric field at location l along the IUT.

The transfer function of the AIMD is then calibrated with selected routing Rval, using 2 selected exposues — (τ_a, ϵ_a) and (τ_b, ϵ_b). The resulting E_{tan} ratio from the two exposures can be expressed as:

$$\frac{\vec{E}_{\text{tan}}(\tau_a, \epsilon_a)}{\vec{E}_{\text{tan}}(\tau_b, \epsilon_b)} = |\text{A}|e^{j(\phi_a - \phi b)} \tag{4.8}$$

Where A is the E_{tan} amplitude ratio between the two exposures, $\phi_a - \phi_b$ are the phase difference, for the selected orthogonal exposures, $\phi_a - \phi_b = \pi/2$. The calibrated P_0 are 22.4 and 6.03 (pW/(V/m)^2) for 64 MHz and 128 MHz, respectively.

4.3.5 RF-Heating Derived from the AIMD Transfer Function

The RF-heating enhancement factor of the IUT, χ, is defined as follows:

$$\chi = P_{\text{dep}}/P_0 \tag{4.9}$$

The theoretical RF-heating enhancement factor (hereafter denoted as χ_{Tier3}) which is derived from the Tier 3 AIMD transfer function can be expressed by combining (4.7) and (4.9) as:

$$\chi_{Tier3} = \left(\int_0^L h\,(l)\,\vec{E}_{\text{tan}}\,(l)\,dl\right)\left(\int_0^L h\,(l)\,\vec{E}_{\text{tan}}\,(l)\,dl\right)^* \tag{4.10}$$

Two other quantities, χ_0 and χ_ϕ, shall be used throughout the rest of the paper. χ_0 is the enhancement factor of the IUT under the unit iso-electric incident condition, $\vec{E}_{\text{tan}}(l) = 1e^{j\phi_0}$ V/m. By definition (normalization of $h(l)$) χ_0= 1. χ_ϕ shall be the maximum enhancement factor achievable with an E_{tan} of the form $1e^{j\phi(l)}$ (iso-magnitude exposure condition), where $\phi(l)$ is an arbitrary phase function. It can be achieved, e.g., by setting $\phi(l) = -\angle\left(h(l)\right)$. In this case, χ_ϕ= $(\int_0^L |h(l)|dl)^2$.

For any unit iso-magnitude exposure condition, $0 \leq \chi_{\text{Tier3}} \leq \chi_\phi$. When the incident E_{tan} does not have a constant magnitude (but still has the same length-averaged magnitude), phase functions can be found that result in χ_{Tier3} that exceed χ_ϕ. However, for real-world conditions, we have found that χ_ϕ is not far from being an upper bound (Figure 4.4).

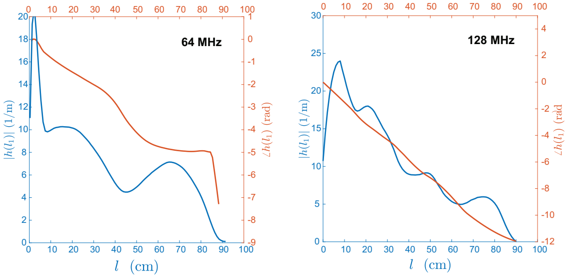

Figure 4.3: Tier 3 RF transfer function of the IUT derived in homogeneous TSM (ϵ_r = 78, σ = 0.47 S/m).

4.3.6 RF-heating Measured from TFD Experiments

To maximize the validation power, exposure conditions were selected such that they sample a wide range of expected enhancement factors, assuming that large enhancement factor differences must be the result of important exposure differences (either because of important changes in the E_{tan} phase distribution, or because of a shift of high exposure locations to another region of the transfer function $h(l)$). Section 4.5 provides a systematic mathematical framework that could be used to further optimize the selection of exposure conditions.

Twenty exposure conditions of the IUT were selected in this study (1-10 for routing R1, 11-20 for routing R2, see Figure 2) based on the distribution of χ_{Tier3} (τ,ϵ) of the IUT. For that purpose, χ_{Tier3} was calculated according to (4.10) for the full range of exposure polarization states (0° $\leq \tau \leq$ 180° and -45° $\leq \epsilon \leq$ 45°).

Figure 4.4 shows the distributions of χ_{Tier3} (τ,ϵ) of the IUT at both 64 MHz and 128 MHz for the two selected routings, R1 and R2. χ_0 and χ_ϕ are highlighted with red solid lines on the colorbars. Diverse incident conditions to the IUT can be obtained by sampling χ_{Tier3} in the (τ,ϵ) space. The selected exposure conditions and associated χ_{Tier3} are marked in Figure 4.4 for each frequency band and routing. As different routings have been selected for calibration and validation, the resulting E_{tan} distribution from calibration and validation are completely different as expected. Figure 4.5 shows the $E_{\text{tan}}(l_1)$ characteristics of the selected exposures for each frequency band. These selected exposures are then used in the radiated testing of the IUT. The selected exposures for the same IUT routing resulting a phase difference of roughly $\pi/2$ for different segments along the routings, with which different segments of the routing can be validated. In addition to that, exposures for routing R1 and R2 resulting a dramatically different E_{tan} along the entire routings, with the two combination, all the IUT segments can then be successfully validated.

The IUT is placed along the selected routings within the phantom of the experimental setup depicted in Figure 4.2. The RF-coil is driven to achieve each polarization state of the B_1 field selected above (Figure 4.4). During each exposure, the B_1 polarization state is reconstructed from the time-domain information recorded by the optical magnetic-field probes and the magnitude of exposure is determined from the magnitude of electric fields at predefined location recorded by the dosimetric probe EX3515 (SPEAG, Zurich, Switzerland), which can measure the RF-heating enhancement factor of the IUT, χ_{TFD}, with a dynamic range of 10 μW/g to 100 mW/g and a sensor positioning uncertainty of ± 0.2 mm.

4.4 Results

The validation power deposition results are summarized in Table 1, and Figures 4.6 and 4.7 summarize the resulting RF-heating enhancement factors of the IUT obtained from the TFD experiments at 64 MHz and 128 MHz,

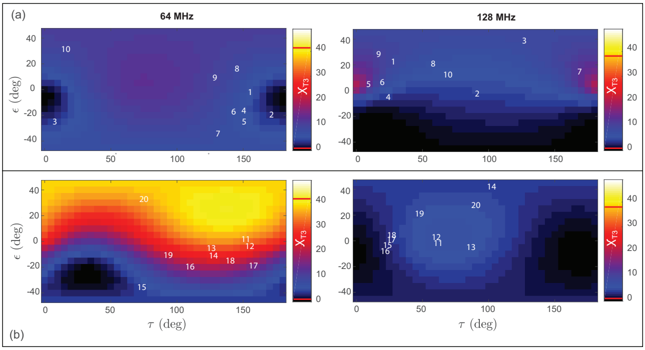

Figure 4.4: (a) Distributions of χ_{Tier3} in the (τ,ϵ) space at 64 MHz and 128 MHz, respectively, with the IUT placed along routing R1. χ_0 and χ_ϕ are highlighted with red solid lines on the colorbars. (b) Same as (a), but for IUT placement along routing R2.

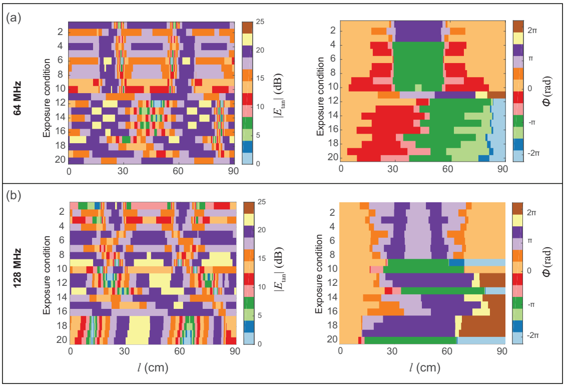

Figure 4.5: Characteristics of the complex-valued E_{tan} of the 20 selected exposure conditions identified for the TFD experiment. (a) Amplitude $|E_{\text{tan}}|$ (left) and phase ϕ (right) of the $E_{\text{tan}}(l_1)$ along the implant routing trajectory l as a function of exposure condition at 64 MHz. (b) Same as (a), but for 128 MHz.

respectively. The comparison of χ_{Tier3} calculated from (4.10), and the experimentally obtained χ_{TFD} is provided. The maximum deviations of χ_{TFD} from χ_{Tier3} are 1.0 dB and 1.5 dB for 64 MHz and 128 MHz exposure, respectively, which is within the estimated combined standard uncertainty of χ_{Tier3} and χ_{TFD}.

The effective B_1 polarization states during the exposure tests can slightly deviate from their theoretical target values and, therefore, each χ_{Tier3} shown in Figures 4.6 and 4.7, is re-evaluated for the B_1 polarization state recorded during each exposure.

As shown in Figures 4.6 and 4.7, test exposure configurations 1-10 show a different dynamic range of the enhancement factor χ than that of test configurations 11-20. This is due to the distinct routing selected for configurations number 1-10 (R1) and number 11-20 (R2). We find that the observed RF-heating enhancement factor (χ) dynamic range of the IUT reaches from 0 to about χ_{ϕ} for 64 MHz exposure and up to $0.5\chi_{\phi}$ for 128 MHz. This is likely due to the roughly twofold higher transfer function phase range at 128 MHz, which increases the probability of destructive interference.

The uncertainty budget of the study comprises uncertainty factors associated with the TFD validation method and the transfer function approach. The TFD method uncertainty includes both experimental and numerical factors (Table 4.2). The total combined uncertainty (obtained as the root-sum-square value of the various experimental and computational uncertainty contributions) of χ_{Tier3} and χ_{TFD} is found to be 1.36 dB and 1.5 dB, respectively (Table 4.2). It is, however, worth to notice that for the comprehensive uncertainty budget analysis of *in vivo* Tier 3 power deposition, uncertainty related to the *in vivo* incident evaluation (e.g., the anatomical routing, anatomical modelling, tissue variety and etc.) should also be included.

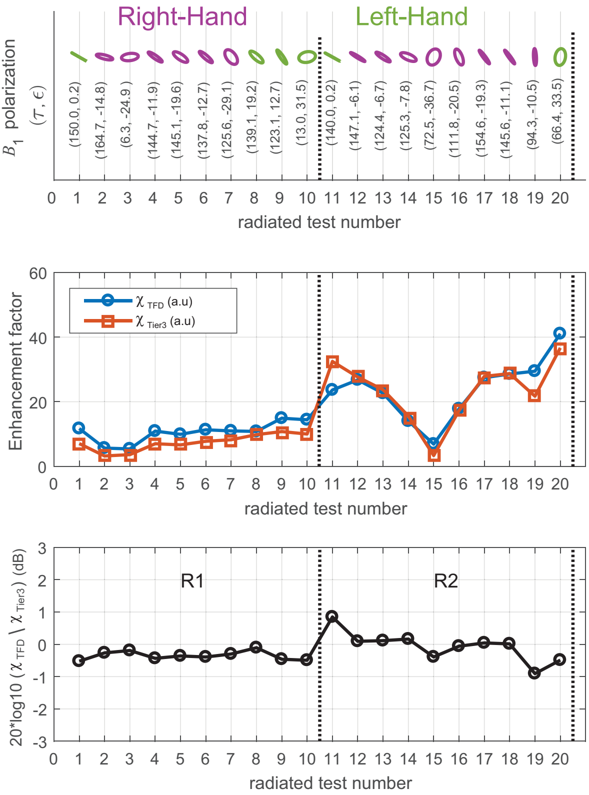

Figure 4.6: Summary of the TFD experiment on RF-induced heating enhancement, evaluated for the IUT at 64 MHz. Twenty exposure test configurations were selected to sample the dynamic range of IUT RF-induced heating enhancement. Top: B_1 polarization states of the selected exposure test configurations. The left-hand and right-hand polarized exposures are indicated in green and purple, respectively. Middle: Measured and calculated RF-heating enhancement factors, χ_{TFD} and χ_{Tier3}, of the selected exposure test configurations. Bottom: Deviation between measured χ_{TFD} and Tier 3 [1] calculated χ_{Tier3}.

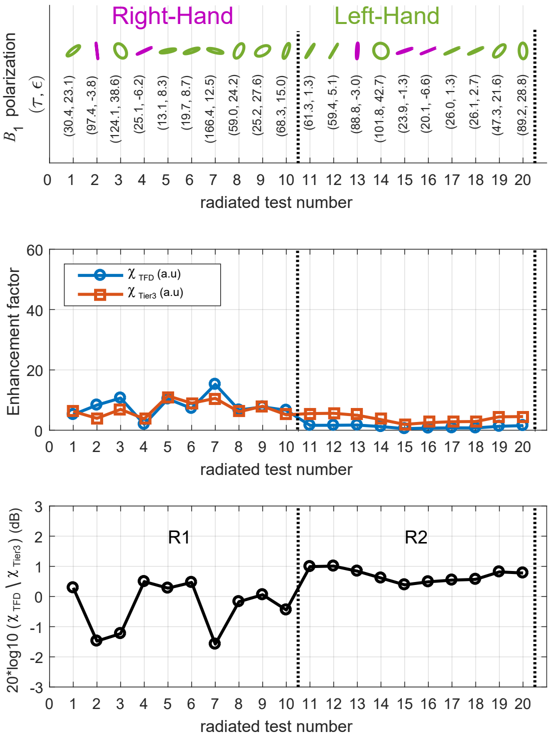

Figure 4.7: Summary of the TFD experiment on RF-induced heating enhancement, evaluated for the IUT at 128 MHz. Twenty exposure test configurations were selected to sample the dynamic range of IUT RF-induced heating enhancement. Top: B_1 polarization states of the selected exposure test configurations. The left-hand and right-hand polarized exposures are indicated in green and purple, respectively. Middle: Measured and calculated RF-heating enhancement factors, χ_{TFD} and χ_{Tier3}, of the selected exposure test configurations. Bottom: Deviation between measured χ_{TFD} and Tier 3 [1] calculated χ_{Tier3}.

Table 4.1: Summarized power deposition obtained from Tier 3 [1] prediction ($P_{\text{dep,Tier3}}$) and validation tests ($P_{\text{dep,TFD}}$)

	64 MHz		128MHz	
Radiated test number	$P_{\text{dep,Tier3}}$ (mW)	$P_{\text{dep,TFD}}$ (mW)	$P_{\text{dep,Tier3}}$ (mW)	$P_{\text{dep,TFD}}$ (mW)
1	0.044	0.055	0.016	0.015
2	0.025	0.027	0.014	0.020
3	0.027	0.025	0.020	0.026
4	0.043	0.052	0.010	0.009
5	0.041	0.047	0.027	0.025
6	0.047	0.053	0.024	0.021
7	0.049	0.052	0.026	0.037
8	0.050	0.051	0.016	0.016
9	0.055	0.065	0.021	0.021
10	0.054	0.063	0.019	0.020
11	0.144	0.112	0.013	0.010
12	0.131	0.126	0.013	0.010
13	0.112	0.107	0.012	0.010
14	0.070	0.066	0.009	0.008
15	0.025	0.028	0.008	0.007
16	0.082	0.084	0.009	0.008
17	0.132	0.130	0.009	0.008
18	0.136	0.135	0.010	0.008
11	0.111	0.139	0.011	0.009
20	0.174	0.194	0.011	0.009

Table 4.2: Uncertainty budget of enhancement factor (χ) evaluation

Source	χ_{Tier3} **Uncertainty (dB)**	χ_{TFD} **Uncertainty (dB)**
TFD exposure		
experimental setup	-	0.86
numerical modeling	0.68	0.68
Local enhancement evaluation		
data acquisition system	-	0.52
TSM	-	0.25
post-processing [96]		0.88
Tier 3 model [49]		
piecewise excitation system [83]	1.18	-
Combined Uncertainty (k = 1)	**1.36**	**1.50**

4.5 Discussion

In this paper, we propose a new method that reduces the required number of different routings and improves the exposure fidelity for a comprehensive transfer function validation of AIMDs with elongated leads. With the proposed TFD test setup, each routing provides sets of diverse distinguished exposure conditions through changing the polarization of B_1.

The diversity of the exposure conditions has been maximized by selecting polarization states that exploit the full achievable enhancement factor (χ) range. Further diversification could be achieved by introducing other unique test routings, or by increasing the number of the birdcage coil channels. At this point it is useful to present a mathematical framework that could be employed to systematically select exposure conditions that maximize sensitivity and validation information content, potentially allowing to further reduce the required number of test conditions.

Despite the fact, that E_{tan} exposures for different (channel-)driving vectors $\vec{v}$ are just linear combinations of the E_{tan} exposures of the N individual channels (E^i_{tan}, where $N = 2$ and $i = x, y$ in our experimental setup), they still provide additional validatory information. This can readily be understood when applying variational calculus to determine the influence of errors in the amplitude ($A(l)$) or phase ($\phi(l)$) of the transfer function $h(l) =$

$A(l)e^{(i\phi(l))}$ on the enhancement factor $\chi = (\int_0^L h(l)E_{tan}(l)dl)(\int_0^L h(l)E_{tan}(l)dl)^*$:

$$\frac{\delta\chi}{\delta A(l)} = 2\mathrm{Re}\left[E_{tan}(l)\cdot e^{(i\phi(l))}F^*_{norm}\right] \tag{4.11}$$

$$\frac{\delta\chi}{\delta\phi(l)} = -2\mathrm{Im}\left[E_{tan}(l)\cdot A(l)e^{(i\phi(l))}F^*_{norm}\right] \tag{4.12}$$

Where $\frac{\delta\chi}{\delta A(l)}$ and $\frac{\delta\chi}{\delta\phi(l)}$ represent the sensitivities of the IUT Tier 3 power deposition enhancement factor (χ) with respect to transfer function amplitude errors ($\delta A(l)$) and phase errors ($\delta\phi(l)$) , respectively. Re [] and Im [] indicate the real and imaginary parts, and $F_{norm} = \int_0^L E_{\tan}(l')\cdot A(l')\exp(i\phi(l'))dl'$. It is apparent from (4.11) and (4.12), that χ is sensitive to errors at locations where $E_{\tan}(l)$ (resp. $E_{\tan}(l)\cdot A(l)$) is large. Therefore, linear combinations of the different channels, which – thanks to complex interference – maximize exposure at locations of interest along the lead, can produce measurements that are particularly sensitive to errors in $h(l)$ at these locations (provided $|h(l)|$ is not too small at these locations, which would again reduce sensitivity). Figure 4.8 shows the sensitivities of the IUT Tier 3 power deposition with regard to transfer function amplitude and phase errors for different $\vec{v}$ (linear and circular polarization (CP) modes). It can be seen, how the two different channels have vastly different sensitivities, and how the combined CP mode is also sensitive to localized errors.

To demonstrate the ability of using different χ measurements with varying $\vec{v}^j$ to constrain the error of $h(l)$, we have investigated the suitability of such measurements to reconstruct $h(l)$, independently from the $h(l)$ measurement approach by piecewise excitation. For that purpose, we assume that $A(l)$ and $\phi(l)$ can be approximated by a finite number (n_A and n_ϕ) of cosine expansion terms: $\widetilde{A}(l;\vec{c}_A) = \sum_{p=0}^{n_A-1} c_{A,p}\cos(2\pi p\frac{l}{L})$ and $\widetilde{\phi}(l;\vec{c}_\phi) = \sum_{q=0}^{n_\phi-1} c_{\phi,q}\cos(2\pi q\frac{l}{L})$. Then we can define the residual function:

$$f_{res}(\vec{c}_A,\vec{c}_\phi) = \sum_t\sum_j\left(\left|\int_0^L E_{tan,t,j}(l)\cdot\widetilde{A}(l;\vec{c}_A)exp(i\widetilde{\phi}(l;\vec{c}_\phi))dl\right|^2 - \chi_{meas,t,j}\right)^2 \tag{4.13}$$

where $E_{\tan,t,j} = \sum_{i=1}^{N}(\vec{v}^j)_i\cdot E^i_{\mathrm{tan,t}}$ is the tangential incident field along trajectory t, for the coil driving vector $\vec{v}^j$. Subsequently f_{res} can be minimized using the *fminsearch* function from MATLAB (The MathWorks, Inc.,

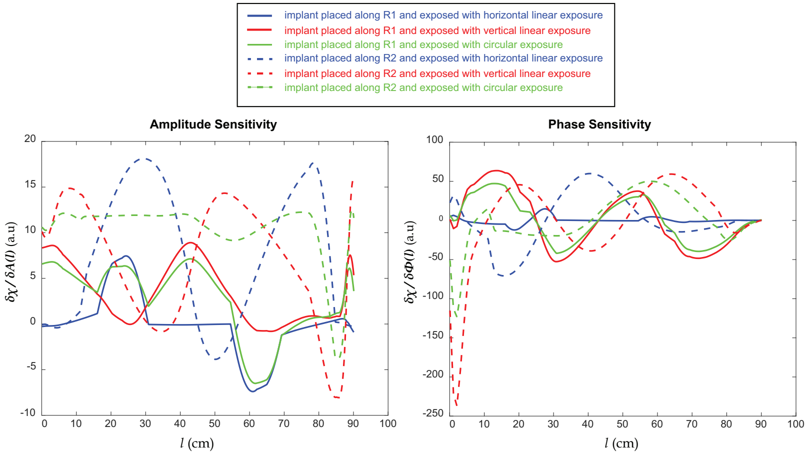

Figure 4.8: Sensitivities of the Tier 3 power deposition enhancement factor (χ) at 64 MHz with regard to errors in transfer function amplitude (left) and phase (right) for different linear and circular polarization (CP) modes.

Natick, Massachusetts, USA). To provide comparable weight to the different excitations $\vec{v}$, the field intensities have been scaled such that $\overline{|E_{\text{tan}}|} = 1$. We have found that values in the order of 10 are suitable (a balance between accuracy and convergence) for n_A and n_ϕ.

Figure 4.9 illustrates, how well $h(l)$ (phase and amplitude) can be reconstructed by minimizing $f_{res}(\vec{c}_A, \vec{c}_\phi)$. Three reconstructions are compared: i) using the measurement data from routing R1 only, ii) using only the data from routing R2, and iii) using both. The reconstruction quality is comparable to how well $h(l)$ can be approximated by its cosine transformation (see Appendix: Suitability of cosine expansion) and also depends on the precision of E_{tan}. Figure 4.10 shows, how well the different approaches manage to fit the measured χ values (in comparison also to the ones evaluated with the measured $h(l)$). As expected, the exposure configurations that were used to reconstruct $h(l)$ fit the results best. To assure independent validation, it is important that the transfer function is determined in a completely different system than the validation system, e.g., using the piecewise excitation technique [83] that employs a different phantom and very different exposures (dipole antenna).

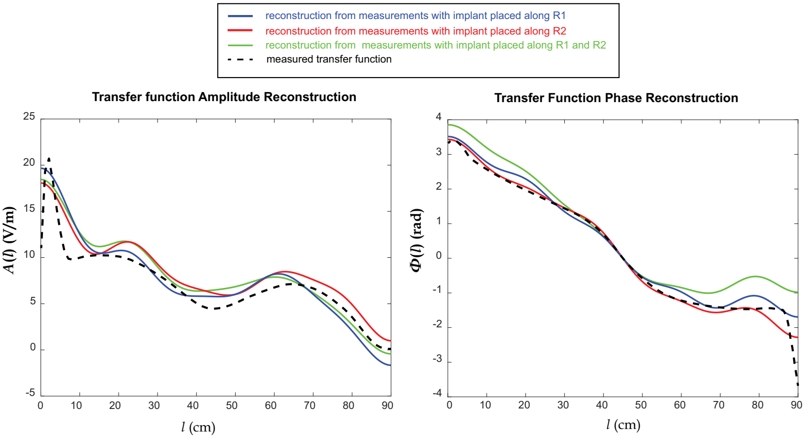

Figure 4.9: Amplitude (left) and phase (right) reconstruction of the IUT RF transfer function at 64 MHz by using the measurement data with implant placed along routing R1 and R2 to minimize the residual function f_{res} in (4.13). The RF transfer function measured by the piecewise excitation technique is also shown with the dashed line.

A further increase in validation power (and a reduction of the associated $h(l)$ uncertainty) could be achieved by optimizing $\vec{v}^j$ such that i) sensitivity to errors in $A(l)$ and $\phi(l)$ is maximized, along with ii) the additional independent information provided by each individual $\vec{v}^j$ (minimization of $E_{tan,t,j}$ correlations). This can be done based on (4.11) and (4.12).

The methodologies introduced in this study (maximization of E_{tan} diversity by full sampling of the enhancement factor variability range) can be used to optimize the validation power of the TFD method and to reduce the associated uncertainty on an individual implant basis. In view of the similarity of many transfer functions for certain device classes and frequency bands, it is also possible to prescribe corresponding, carefully chosen, fixed and generally applicable exposure conditions for routine evaluations. One limitation of the TFD method is its sensitivity to misplacement of the transverse plane normal to the ($z-$)axis of the birdcage test coil, where the implant lies, because of the strong dominance of the electric field component

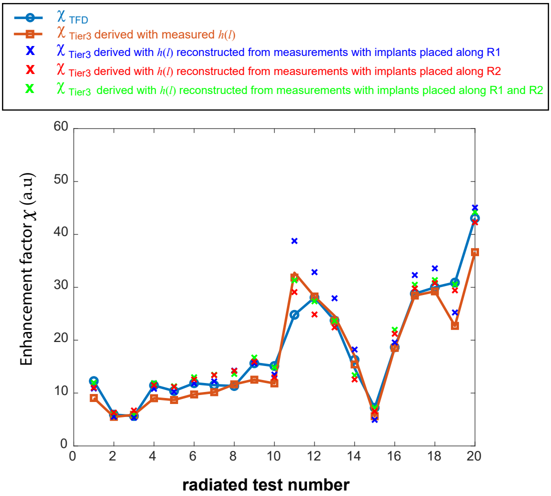

Figure 4.10: RF-heating enhancement factors of the IUT at 64 MHz for different test number (Figure 4.6) obtained with differently reconstructed RF transfer functions.

in this axis.

While the TFD method has been developed and optimized for the described exposure system, it is also applicable to other test systems (e.g., different RF coil geometries, tissue simulating media, etc.). However, its performance and associated uncertainties would have to be re-investigated for each implementation. The next step is to extend the methodology to ultrahigh fields that requires development of the corresponding equipment and reassessment of all the sensitivities.

4.6 Conclusion

Based on the finding that amplitude and phase of the incident tangential electrical field along a single lead path in a cylindrical phantom can be sufficiently vareid by changing the polarization of the incident magnetic field inside standard birdcage RF coils, a TFD method has been proposed in this work to provide diverse incident conditions to the implant under test while preserving the fidelity of the incident conditions, which allows an effient and reliable characterization of transfer function of AIMD with elongated leads.

The proposed AIMD exposure setup has been characterized and validated and meets the requirements regarding negligible backscattering effects between AIMD sections and phantom boundaries. The uncertainty (k=1) of the incident conditions associated with the phantom and provided IUT is 0.86 dB (Table 4.2).

The TFD method has been successfully applied to a 90 cm long IUT, and the deviation of the experimentally evaluated RF-heating from theoretical values is less than the combined standard uncertainty of 2 dB (root-sum-square of 1.36 and 1.5 dB in Table 4.2). With the proposed TFD method, for the same number of validation test configurations (20 in this case), the time required by TFD is about 20 times less than that for the methods applied in [1, 88, 33, 89, 97, 37, 90].

Appendix: Suitability of cosine expansion

The approximation of the phase and amplitude of $h(l)$ for an AIMD without lumped elements by a cosine expansion is motivated by the following factors: i) appreciation of the curve shape (continuous, without sharp bends, but oscillating); ii) desire to avoid complex-valued decompositions (such as the Fourier transformation), because of the real-valued nature of A and ϕ and because performing a complex derivative to evaluate (4.11) and (4.12) is not possible (violation of the Cauchy-Riemann equations); iii) numerical investigations have shown that the cosine approximation can approximate $h(l)$ well, with a moderate number of terms. However, it should be noted that the cosine transformation assumes a symmetric function, which enforces a zero derivative at $l = 0$ that is not present in $h(l)$ – in fact $h'(0)$ is relatively steep. Therefore, the fitting cannot be expected to be perfect in that region. Investigations involving seven experimentally determined AIMD transfer functions have shown that the cosine transformation provides superior results in comparison with the sine function and is always able to approximate $h(l)$ with a small standard deviation.

Chapter 5

Data-driven Experimental Evaluation Method for the Safety Assessment of Implants with Respect to RF-induced Heating During MRI

5.1 Abstract

[1]Small (mm-size) distal electrodes of active medical implants can cause localized radiofrequency (RF)-induced power deposition with extreme spatial gradients (5-6 dB/mm). We propose a method that aims to improve the accuracy of the traditional experimental evaluation, which relies solely on hardware instrumentation. A numerically-derived local deposition distribution is used to assist the estimation of power deposition. The method was

---

[1] This Chapter has been published in [98]

successfully validated against numerical simulations, considering three different generic implants with a single electrode. The power deposition in the surrounding region of the implant electrodes estimated with the proposed method was validated with less than 1 dB (30%) uncertainty.

5.2 Introduction

Magnetic resonance imaging (MRI) is now considered one of the most widely used technologies in the assessment of global and regional tissue and inner organ function. The number of patients receiving MRI increases as the imaging modality becomes more commonplace. Likewise, the number of patients with medical implants, both with and without electronic components, is rapidly and constantly growing [15, 65, 25, 99]. At the intersection of these two populations lies a serious safety concern.

The presence of implants poses several potential risks for a patient undergoing MR imaging. Radio frequency (RF) induced heating is one of the most critical safety issues for implants — especially, those with elongated configurations (e.g., neurostimulator, cardiac pacemaker, etc.) The RF exposure can induce strong electric fields inside the body which leads to temperature elevations of more than several degrees in the body tissues[69]. This may cause an unacceptable health risk to the patient [77].

As invasive electromagnetic (EM) or temperature measurements within the human body are generally not feasible, RF-induced heating assessment of implants is customarily conducted via *in vitro* (in phantoms) and animal experiments. [100, 57, 101, 102, 78, 103, 32, 104]. Although *in vitro* experiments cannot be used directly to evaluate conclusively the *in vivo* RF-heating of implants within the patient, they are an integral part of RF-heating assessment of implants. It is necessary in practice to investigate RF-heating characteristics of implants under well-controlled test conditions [63, 105, 38, 106, 26].

Traditional *in vitro* experiments generally entail a measurement of induced temperature rise (T) or specific absorption rate (SAR) at sampled locations in the vicinity of the implant by ways of temperature or dosimetric sensors [59, 57, 101, 102, 107, 97]; the sampled locations are typically within the regions of high heating, such as locations close to the interface between tissue and electrode contact. Due to the high spatial gradient of the induced temperature and SAR distributions (e.g., 2 dB/mm for temperature and 5 dB/mm for SAR are not uncommon), highly accurate positioning of the sensors (sub-mm accuracy) is required to obtain measurement values with reasonable experimental uncertainty.

In Section 5.3, we elaborate the limitations of the traditional *in vitro* experimental method for assessing RF-heating of implants and thus, the motivation for our work. In Section 5.4, we propose a complementary evaluation method that improves upon the traditional method by using simple numerical modeling and image processing algorithms to overcome the stringent requirement on sensor positioning. In the proposed method, only a limited part of the implants need be numerically modeled to derive the high-resolution induced SAR distribution over the region of high-heating. Therefore, substantial computational resources are not required. We apply the proposed evaluation method to three different generic implants and the estimated power deposition of the implants is validated against full-wave computational electromagnetics (CEM) simulations of the completely modeled implants and RF exposure conditions. As a comparison, the power deposition of the three generic implants estimated using the traditional method as described in [97] is provided as well. The results are compiled in Section 5.5.

5.3 Motivation

There are several guidelines describing *in vitro* experiments required in the RF-heating assessment of implants [63, 1]. A test phantom filled with tissue simulating medium (TSM) is commonly used to submerge the implant under test. The phantom is then exposed to RF energy, usually generated with an RF source which provides MRI-like RF exposure conditions. The induced temperature or SAR at sampled locations, typically within the region of high heating, such as locations in close proximity to electrode-TSM interface, is measured with temperature or dosimetric sensors, respectively. The region of high-heating exhibits an extremely high spatial gradient in the induced T and SAR (5 – 6 dB/mm and 1 – 2 dB/mm spatial gradient in SAR and T, respectively, are not uncommon). Sub-millimeter accuracy in the positioning of the sensors is required to obtain measurement values with reasonable experimental uncertainty. Figure 5.1 plots the spatial gradients of induced SAR and T at the locations in the vicinity of the exposed metallic tip of two generic implants with a tip length of 2 mm and 10 mm.

The induced SAR and T are extracted from full-wave FDTD numerical simulations, along a line near the exposed metallic tip. The region where the experimental evaluation is usually performed is colored in gray.

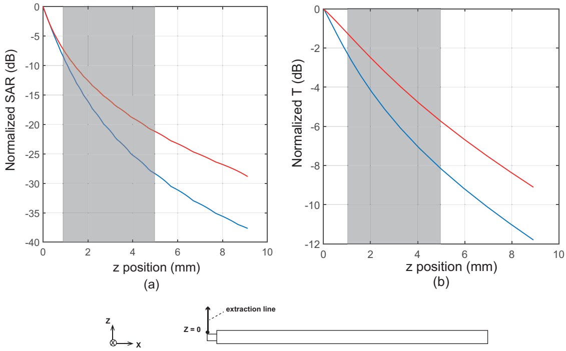

Figure 5.1: Examples of normalized SAR and T at locations in the vicinity of two generic implants with 2 mm (blue) and 10 mm (red) tip size, obtained from numerical simulations. 0 dB is referenced to the SAR and T values at z = 0 mm (touch) position. The gray region indicates the locations where measurements are usually performed.

The ultimate goal of RF-induced heating evaluation is to determine potential tissue damage in the patient and temperature increase seems most suitable metric. However, it must be reiterated that *in vivo* temperature increases in tissue cannot be directly inferred from temperature increases found in phantom experiments, as most *in vitro* experiments do not reflect the thermal conditions resembling that of the *in vivo* situation. The results of *in vitro* experiment are limited to a power metric (SAR or power deposition) to promote corroboration of results from different studies. The power deposition can then be translated to tissue heating, considering appropriate thermal conditions [47].

To assess power deposition, either SAR-based or T-based experiments can be used. Although the induced T profile in the vicinity of the electrodes has a spatial gradient that is much lower than that of the induced SAR, T evaluations suffer from other practical drawbacks. In order to prevent heat convection, the temperature sensors must remain stationary during exposure. A sensor is required at each sample measurement location, thus limiting the number of sampled locations allowed in a concurrent acquisition. Repositioning of the sensors is feasible but time-consuming and becomes an overwhelming task when extrapolated to multiple tests. On the contrary, SAR evaluation can be performed with a single dosimetric sensor and a positioning system that allows repositioning of the sensor at multiple sample locations. Therefore, a SAR evaluation method is preferable in practice if the high-spatial-gradient restriction need to be overcome.

5.4 Proposed Method

RF-induced heating evaluation is not a trivial process. Obtaining an estimate of power deposition in tissue caused by the RF-implant interactions requires dedicated instrumentation and a robust evaluation protocol. In this section, the implementation of our proposed evaluation method is described in detail. We divide our method into three parts: 1) exposure definition, 2) data acquisition, and 3) post-processing. The method, described in this section, is applied to three generic implants and the results are consolidated in Section 5.5.

5.4.1 Exposure Definition

First and foremost, an incident condition or exposure condition must be defined. For this study, we choose a constant magnitude and constant phase tangential electric field along the implant (hereafter, referred to as iso-electric) as the exposure condition. This is one of the most commonly used incident conditions in RF-induced heating evaluation of implants [1].

A two-port generic birdcage coil is used to provide an RF exposure at 64 MHz. An elliptical phantom filled with TSM ($\epsilon_r = 78$, $\sigma = 0.47$ S/m) and a dedicated implant holder are designed to provide an approximately iso-electric incident condition to the implant (magnitude and phase variation of less than 0.5 dB and ±5 degrees, respectively). Figure 5.2 illustrates the experimental setup comprising the two-port RF coil, the TSM-filled elliptical phantom, the dedicated implant holder, and an implant sample.

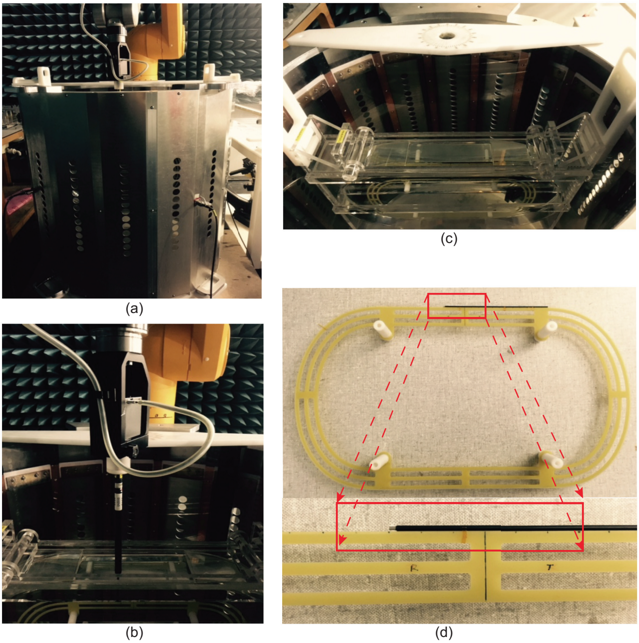

Figure 5.2: (a) Two-port RF coil and the robotic acquisition system. (b) EX3DV4 dosimetric probe positioned inside the elliptical phantom at a sample location. (c) TSM-filled elliptical phantom, positioned optimally within the RF-coil for iso-electric exposure. (d) Implant placement on the implant holder, optimally designed for iso-electric incident condition to the implant.

5.4.2 Data Acquisition

To perform the measurement, a high-precision robotic measurement system is used to position a dosimetric probe. Figure 5.2 demonstrates the data acquisition system used in this study; it comprises the DASY52 robotic measurement system and the EX3DV4 dosimetric probe (SPEAG, Switzerland). The RF-induced point SAR is measured at the sampled locations illustrated in Figure 5.3: a scan volume of 80 mm x 6 mm x 2 mm with scan resolution of 2 mm x 1 mm x 1 mm. Three generic implant samples (see Figure 5.3) are considered in this study:

- Sample A: A 150 mm-long solid conductor with 1.5 mm-diameter and a 0.5 mm-thick insulation layer. The insulation is removed at one end, leaving a 2 mm-long exposed metallic tip. The other termination is left isolated.
- Sample B: A 150 mm-long solid conductor with 1.5 mm-diameter and a 0.5 mm-thick insulation layer. The insulation is removed at one end, leaving a 10 mm-long exposed metallic tip. The other termination is left isolated.
- Sample C: A 110 mm-long coiled conductor. The conductor is 0.2 mm in diameter. The pitch and diameter of the helical coil are 0.3 mm and 0.6 mm, respectively. The coil insulation layer is 0.4 mm-thick. The coil is terminated at one end in a 1 mm-diameter, 5 mm-long copper tip and the other termination is isolated.

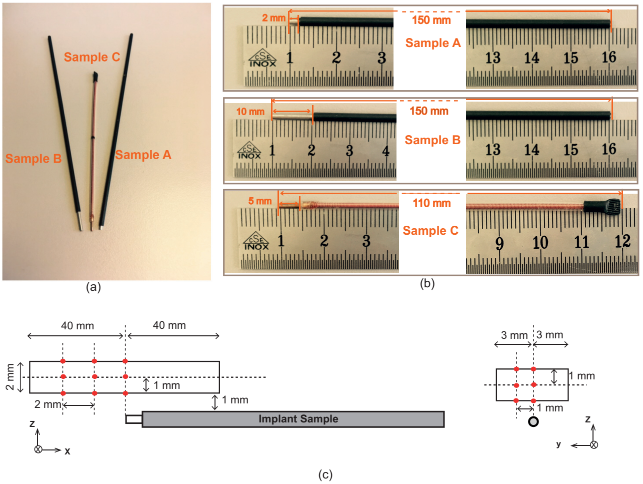
Sample C
Sample B
Sample A
2 mm
150 mm
Sample A
10 mm
150 mm
Sample B
5 mm
110 mm
Sample C
40 mm
40 mm
2 mm
1 mm
1 mm
2 mm
Implant Sample
z
x
3 mm
3 mm
1 mm
1 mm
z
y

(a)

(b)

(c)

Figure 5.3: (a) Implant samples used in this work. (b) The detailed geometry of implant samples A, B, and C. (c) Top view and side view of the measurement grid. The sample locations are indicated by red dots.

5.4.3 Post-processing

In our proposed method, only a limited part of the implants need be numerically modeled to derive the high-resolution induced SAR distribution near the electrode. Therefore, substantial computational resources are not required. This high-resolution profile (hereafter refer to as SAR_{HR}) is used in a feature-based registration of the measurement data and provides the sub-mm accuracy unavailable in the traditional method. Figure 5.4 illustrates the SAR_{HR} for implant samples A, B, and C. The power deposition of the tip electrode (P_0) is calculated from a volume integral containing the -30 dB contour relative to the maximum deposition.

The induced SAR measured by the dosimetric probe at the sample locations, SAR_{meas}, are co-registered with the SAR_{HR}. The co-registration is implemented as a simple translation of SAR_{HR} along the three cardinal axes by $\boldsymbol{\Delta} = (\Delta x, \Delta y, \Delta z)$, and down-sampling to the measurement locations, $\boldsymbol{r}_i$. In short, a linear least-square is applied to solve for the real-valued scalar, α, and the translation vector, $\boldsymbol{\Delta}$:

$$\min_{\alpha,\boldsymbol{\Delta}} \sum_{i=1}^{N} \left|\alpha SAR_{\text{HR}}(\boldsymbol{r}_i + \boldsymbol{\Delta}) - SAR_{\text{meas}}(\boldsymbol{r}_i)\right|^2 \tag{5.1}$$

where N is the number of sample measurement points. An optimal solution set, α_{opt} and $\boldsymbol{\Delta}_{\text{opt}} = (\Delta x_{\text{opt}}, \Delta y_{\text{opt}}, \Delta z_{\text{opt}})$, is determined by the set of α and $\boldsymbol{\Delta}$ that produces the minimum square error. For brevity, we define:

$$SAR_{\text{opt}} = \alpha_{\text{opt}} SAR_{\text{HR}}(\boldsymbol{r}_i + \boldsymbol{\Delta}_{\text{opt}}) \tag{5.2}$$

and $P_{\text{TIP}} = \alpha_{\text{opt}} P_0$ is the estimated power deposition of the implant with P_0 defined by:

$$P_0 = \rho \int_V SAR_{\text{HR}}(\boldsymbol{r}) dv \tag{5.3}$$

where V is the volume containing the -30 dB contour relative to the maximum deposition and $\rho = 1000$ kg·m^{-3} is assumed for TSM.

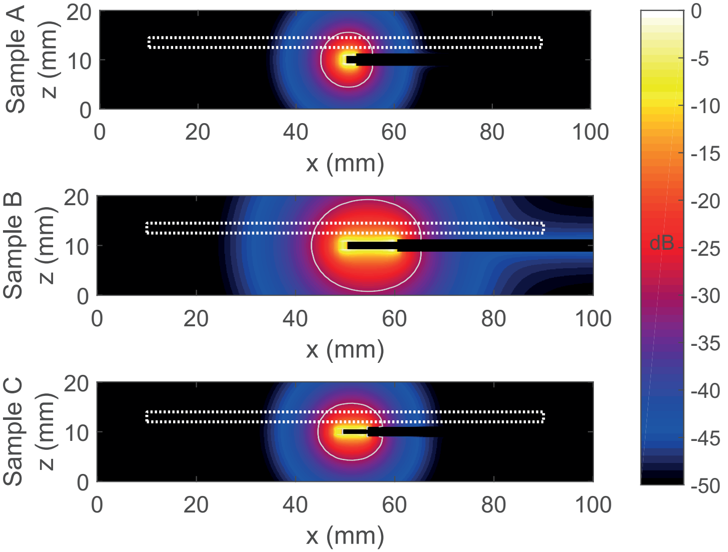

Figure 5.4: SAR_{HR} of implant samples A, B, and C (0 dB is the maximum SAR of each implant), with the -30 dB contour marked by a white solid line. The x-z plane of the measurement region is shown as the white rectangular box.

5.5 Results

The results obtained from our proposed method are validated against reference simulations of the experimental setup. Contrary to the simulations of 5.4.3 used to obtained SAR_{HR}, where only a small part of the implant is modeled, the objective of the reference simulations is to mimic the experimental condition as closely as possible. Therefore, the RF-source, phantom, and generic implant samples, must be rendered in details. A generic shielded 1.5 T (64 MHz) RF coil loaded with a TSM-filled elliptical phantom, with each implant sample placed inside the phantom, resembling that used in the experiment, is numerically modeled and induced EM fields are calculated from full-wave FDTD simulation. Figure 5.5 shows the full-wave reference simulation setup for all implant samples. The power deposition of the reference simulation is calculated from a volume integral similar to (5.3). The uncertainty of the power deposition derived from the reference simulations is assessed to be 0.3 dB (see supplemental material for details Chapter B).

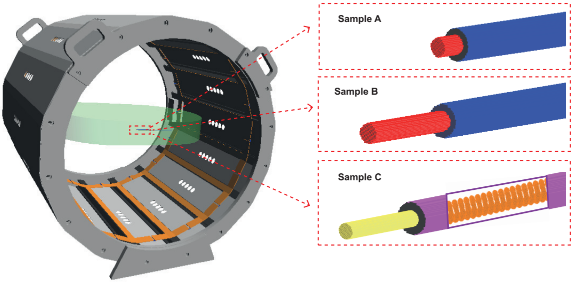

Figure 5.5: Reference simulations setup for implant samples A, B, and C.

The proposed experimental method, described in Section 5.4, is applied to the three implant samples and the estimated power deposition (P_{TIP}) of each implant electrode is obtained. The uncertainty budget of the estimated power deposition obtained with the proposed method and with the traditional method is provided in Table 5.1 (see supplemental material for details Chapter B).

The main difference between the traditional [97] and proposed methods is the use of a data-assist co-registration algorithm in the proposed method as described in Section 5.4.3. For the traditional method, $\alpha_{\text{opt}} = 1$ and $\mathbf{\Delta}_{\text{opt}} = (0, 0, 0)$, while α_{opt} and $\mathbf{\Delta}_{\text{opt}}$ are derived from (5.1) for the proposed method. Table 5.2 summarizes the deposited power of the three implant samples obtained with the proposed evaluation method, traditional method, and those obtained from reference simulations. The deviations of the results between the proposed method and reference simulations, $|\Delta_{\text{prop}}|$, are less than 0.4 dB for all experiments considered in this study — well within the combined uncertainty budget of the proposed evaluation method. Whereas with the traditional method, the deviations, $|\Delta_{\text{trad}}|$, are between 1 – 2.3 dB, incontestably higher than the proposed method.

The implants are exposed to E_{inc} = 35 – 70 V·m^{-1}; where E_{inc} is the magnitude of the tangential component of the electric fields along the

Table 5.1: Uncertainty budget of the estimated power deposition of the AIMD obtained with the traditional method and with the proposed method.

Source	Traditional Method Uncertainty (dB)	Proposed Method Uncertainty (dB)
Exposure Definition		
Exposure Drift	0.20	0.20
Phantom	0.19	0.19
TSM	0.27	0.27
Combined Uncertainty (k = 1)	**0.39**	**0.39**
Data Acquisition		
Data Acquisition Electronic	0.32	0.32
Truncated Boundary	0.29	0.29
Field Sensor Position	1.45	0.00
Combined Uncertainty (k = 1)	**1.52**	**0.43**
Post Processing		
SAR_{HR}	0.39	0.39
Power Calculation	0.46	0.46
Co-registration	0.00	0.29
Combined Uncertainty (k = 1)	**0.60**	**0.67**
Total Combined Uncertainty (k = 1)	**1.68**	**0.88**

implant, measured during the exposure without the implant present. Figure 5.6 shows the results of our evaluation for samples A, B, and C at incident field level E_{inc} = 50 V·m^{-1}. The data collection was done with the EX3DV4 dosimetric probe which comprises 3 small electric dipole sensors in a 2.5 mm-diameter PEEK enclosure. Figures 5.6(a), (c), and (e) compare the SAR_{meas} and SAR_{opt} 2D-distributions of the three implants. Figures 5.6(b), (d), and (f) show the pixel-to-pixel correlation of SAR_{meas} and SAR_{opt} of Figures 5.6(a), (c), and (e).

Next, we perform the evaluation with two different types of dosimetric probes: EX3DV4 and ET1DV4. The ET1DV4 has a single electric dipole sensor and a 1.2 mm-diameter PEEK enclosure. The difference in the results obtained from the two dosimetric probes is $\sim$ 0.4 dB.

In practice, a high incident field magnitude ($E_{\mathrm{inc}} \geq$ 200 V·m^{-1}) may be difficult to achieve. We verified that the experimental data can be acquired over any moderate exposure level, provided that the experiment is within a valid operating range of the instrumentation (e.g., dosimetric probe and acquisition electronics). Different levels of the induced SAR were provided by adjusting the input power to the RF coil to achieve E_{inc} = 35, 50, and 70 V·m^{-1} along the implant. Figure 5.7 shows P_{TIP} evaluated for implant sample A exposed to different E_{inc} levels. The experimental results from the three incident field levels are indicated by the red ‘o’ markers and the nu-

Table 5.2: Summary of estimated power deposition obtained from proposed method, traditional method, and reference simulations. The deviation of the values obtained with proposed and traditional method from the reference values, $||\Delta_{\text{prop}}||$ and $||\Delta_{\text{trad}}||$, are provided in dB.

P_{TIP}						
Sample	**Scenario**	**Proposed Method (mW)**	**Traditional Method (mW)**	**Ref. Simulation (mW)**	**$\|\|\Delta_{\text{prop}}\|\|$ (dB)**	**$\|\|\Delta_{\text{trad}}\|\|$ (dB)**
A	Sc2	60.0	39.9	57.9	0.2	1.6
B	Sc2	78.0	48.9	81.7	0.2	2.3
C	Sc2	53.0	64.0	50.3	0.2	1.0
A	Sc1	31.0	-	28.4	0.4	-
A	Sc2	60.0	-	57.9	0.2	-
A	Sc3	111.0	-	113.0	0.1	-
A	Sc2	60.0	-	57.9	0.2	-
A	Sc4	53.0	-	57.9	0.4	-

Sc1, Sc2, and Sc3: implant exposed to E_{inc}= 35, 50, and 70 V·m^{-1}, respectively. EX3DV4 dosimetric probe used in data acquisition.

Sc4: implant exposed to E_{inc}= 50 V·m^{-1}. ET1V4 dosimetric probe used in data acquisition.

merical results, derived from the reference full-wave simulation of implant sample A, are indicated by the blue solid line. The results show excellent linearity with E^2_{inc} and the evaluation method can be applied to any moderate exposure levels. Thus, the result obtained at a certain incident field level can be translated to any target incident field magnitude.

It has been demonstrated that the proposed method is objective to the different AIMD types, exposure definitions, and data acquisitions — an optimal solution was consistently obtained within 1 dB uncertainty. No customizations of the evaluation protocol with respect to the particular tested implant samples, exposure definitions, or data acquisitions, were needed. Most importantly, only approximate positioning of the sensor with respect to the implant was needed which substantially relaxes the strict requirement on sensor positioning accuracy.

5.6 Conclusion

The steep spatial gradient of the induced SAR distribution in the vicinity of the implant electrodes (on the order of 5 – 6 dB/mm) poses a great challenge to the experimental evaluation method used in practice. Traditional SAR-based evaluation of implant RF-induced heating inevitably suffers from large uncertainty associated with sensor positioning with respect to the implant. Our proposal supplements existing experimental methods and hardware to improve the resulting accuracy of RF-heating estimation. We provide a method where a numerically-derived induced SAR distribution is used to assist in the estimation of RF power locally deposited by the implant.

The robustness of the method was examined with respect to a variety of implants (3 different implant samples), exposure levels (3 different E_{inc} levels), and data acquisition procedures (2 different types of dosimetric probes). No customization of the protocol was required in the evaluation of the three generic samples. The proposed method was successfully validated against reference CEM simulations resembling the true experimental setup for three generic implants. The power deposition of the implants obtained with the proposed method has an associated standard uncertainty of less than 1 dB (30%). This is much reduced from that of the traditional SAR-based evaluation method, estimated to be at least 2 dB.

Lastly, the limitations of the current study must be noted. The study is limited to implants with a single electrode (i.e., single high-gradient SAR/deposition profile) exposed to a single (iso-electric) incident condition. In theory, the proposed method can accommodate devices with multiple electrodes — a characteristic common to medical implants currently in clinical usage, and any exposure condition. However, further investigation is needed. It must be determined if additional sources of uncertainty will compromise the accuracy of the method. Minimum requirements of the method befitting a variety of exposure conditions and implant characteristics shall be derived in future studies.

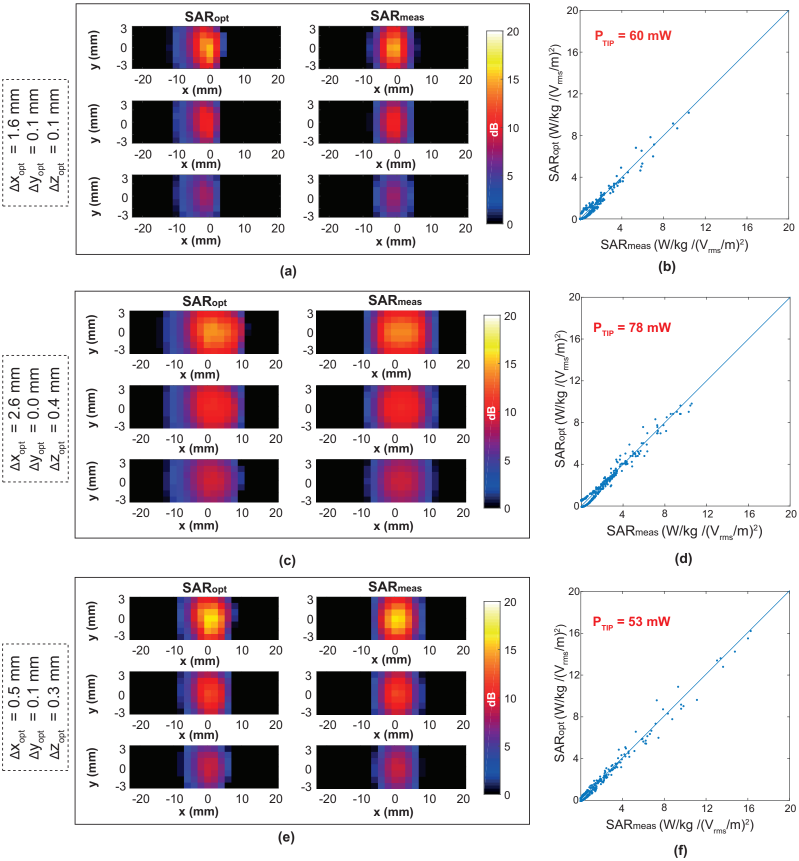

Figure 5.6: Evaluation results of implant sample A (top), sample B (middle) and sample C (bottom), exposed to E_{inc} = 50 V·m^{-1}. (a) XY-plane view of SAR_{meas} and SAR_{opt}. From top to bottom, the SAR distribution in three measurement slices from closest to furthest from the implant is depicted. The measurement slices are the same as those defined in Figure 5.3. (b) The pixel-to-pixel correlation of SAR_{meas} and SAR_{opt}. (c) - (d) show similar information as (a) - (b) for sample B. (e) - (f) show similar information as (a) - (b) for sample C.

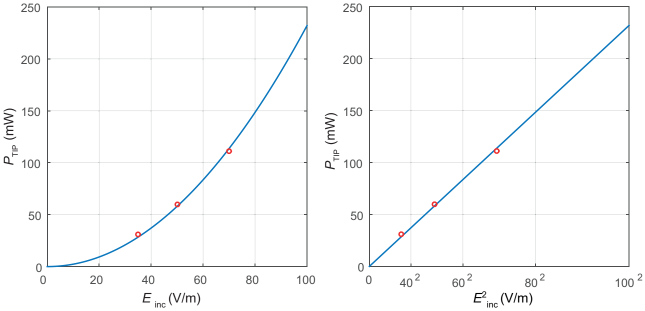

Figure 5.7: Quadratic relationship of P_{TIP} with E_{inc} (i.e., linear relationship of P_{TIP} with E^2_{inc}). P_{TIP} evaluated for implant sample A exposed to E_{inc} = 35, 50, and 70 V·m^{-1} are indicated by the red 'o' markers. The total power deposition of implant sample A as a function of incident tangential electric fields along the implant, derived from the reference full-wave simulation, is indicated by the blue solid line. (a) P_{TIP} as a function of E_{inc}. (b) P_{TIP} as a function of E^2_{inc}.

Part IV

in vivo Human-RF Interaction Evaluation

Chapter 6

Anatomical Model Uncertainty for RF Safety Evaluation of AIMD Under MRI Exposure

6.1 Abstract

[1] The Virtual Population (ViP) phantoms have been used in many dosimetry studies, yet, to date, anatomical phantom uncertainty in radiofrequency (RF) research has largely been neglected. The objective of this study is to gain insight, for the first time, on the uncertainty in RF induced fields during magnetic resonance imaging associated with tissue assignment and segmentation quality and consistency in anatomical phantoms by evaluating the differences between two generations of ViP phantoms, ViP1.x and ViP3.0. The RF-induced 10 g-average electric (E-) fields, tangential E-fields distribution along active implantable medical devices (AIMD) routings, and estimated AIMD-heating were compared for five phantoms that are part of both ViP1.x and ViP3.0. The results demonstrated that differences exceeded

---

[1] This Chapter has been published in [108]

3 dB ((-29%, +41%)) for local quantities and 1 dB (±12% for field, ±25% for power) for integrated and volume-averaged quantities (e.g., estimated AIMD-heating and 10 g-average E-fields), while the variation across different ViP phantoms of the same generation can exceed 10 dB ((-68%, +217%) for field, (-90%, +900%) for power). In conclusion, the anatomical phantom uncertainty associated with tissue assignment and segmentation quality/consistency is larger than previously assumed, i.e., 0.6 dB or ±15% ($k = 1$) for AIMD-heating. Further, multiple phantoms based on different volunteers covering the target population are required for quantitative analysis of dosimetric endpoints that depend on patient anatomy, e.g., AIMD-heating. Phantoms with the highest fidelity in tissue assignment and segmentation should be used, as these ensure the lowest uncertainty and possible underestimation of exposure. To verify that the uncertainty decreases monotonically with improved phantom quality, the evaluation of differences between phantom generations should be repeated for any improvement in segmentation.

6.2 Introduction

Anatomical human phantoms are a key component in dosimetric studies investigating the absorption of electromagnetic fields in the human body in implant safety assessments [44, 45]. With the exception of a few phantoms based on cryosection images [109, 110], most of the available phantoms were derived from images of Computational Tomography (CT) or Magnetic Resonance Imaging (MRI) scanners [111, 112, 113, 114, 115, 116, 117].

High-fidelity phantoms of the human body represented by polygon meshes were developed by the IT'IS Foundation in collaboration with the U.S. Food and Drug Administration, Center for Devices and Radiological Health (FDA/CDRH) [117]. This widely utilized set of anatomical phantoms is known as the Virtual Population Version 1.x (ViP 1.x). The ViP 1.x has been used in a variety of computational electromagnetics (CEM) studies, such as (i) dosimetry of mobile phones, e.g., [45, 118, 119], (ii) exposure assessment of home appliances, e.g., [120, 121], (iii) hyperthermia therapy, e.g., [122, 123, 124], (iv) implant-radiofrequency (RF) interactions, e.g., [87, 48, 125, 126], (v) medical imaging research, e.g., [127, 128, 129, 130]. ViP 1.x has also been applied in more than 200 submissions to the FDA, mainly for demonstration of MR safety of active implants.

As tools and knowledge have evolved over recent years, the review of

ViP 1.x has revealed some limitations in the local detail and accuracy related to the segmentation of organs, poor tissue surface mesh quality, insufficient structure continuity and details, and inconsistent tissue assignment across all phantoms. A considerable research and development effort to overcome these deficiencies resulted in the release of the latest generation of ViP 3.0 [131]. In particular, the ViP 3.0 has been enhanced and refined to better suit medical applications, where higher fidelity in the local anatomical features is required [132, 133]. Four of the ViP 3.0 phantoms (Duke, Ella, Billie, and Thelonious) were simplified to contain 22 separate tissue groups and optimized for finite-element modeling; these phantoms are freely distributed as ViP 2.0.

An important question to be addressed relates to the uncertainty posed by the limitations of the phantoms with respect to population sampling, segmentation, tissue parameters, and discretization. While the latter two factors can be easily evaluated by means of a sensitivity analysis, the first two are difficult to quantify, as the segmentation and number of samples cannot be easily increased and varied, and the effort to segment and validate one model requires more than one year of effort for a very experienced physician or biologist. Presumably for this reason, population- and segmentation-based uncertainty contributions associated with exposure evaluations have not previously been systematically studied in the literature. In this paper, we characterize the RF-exposure uncertainty posed by segmentation by comparing the results of ViP 1.x and ViP 3.0 from multi-tier safety assessments of MRI RF-induced heating of active implantable medical devices (AIMD), according to Clause 8 of ISO/TS 10974 [1].

6.3 Method

The following phantoms, tools, and evaluation protocols were applied to assess the impact of the use of ViP 3.0 versus ViP 1.x in safety evaluations of AIMDs in MRI.

6.3.1 Anatomical Phantoms

Five ViP phantoms that occur in both versions 1.x and 3.0 were included in the study (Table 1). The stated differences in height and mass are the results of differences in discretization.

6.3.2 Simulation of the MRI Environment

The incident field was generated by a generic 1.5 T (64 MHz) high-pass RF body coil with dimensions similar to those of a typical 70-cm-bore scanner (75-cm-coil diameter, 50-cm-coil length, 150 cm shield length) [134, 135]. This well represents the typical clinical magnetic RF fields with clockwise circular polarization in its iso-center with respect to the positive z-axis (pointing from feet to head). The field has been verified by measurements performed in [136]. For each anatomical phantom, three imaging positions, namely at the head, thorax, and pelvis, were evaluated. Furthermore, left and right AIMD routing groups per imaging position were defined: (i) left and right deep brain stimulator (DBS) routing groups ($\mathrm{DBS_L}$and $\mathrm{DBS_R}$) at the head imaging position: the routings run underneath the skin from the proximal ends of the left and right pectoral muscles, along the side of the neck behind the left and right ears, up to the crown of the head, and through the skull, terminating in the distal end of the thalamus; (ii) left and right pacemaker (PM) routing groups ($\mathrm{PM_L}$ and $\mathrm{PM_R}$) at the thorax imaging position: the routings run underneath the skin from the proximal ends of the left and right pectoral and along the veins, terminating in the distal end of the left heart ventricle; and (iii) left and right spinal cord stimulator (SCS) routing groups ($\mathrm{SCS_L}$ and $\mathrm{SCS_R}$) at the pelvis imaging position: the routings run underneath the skin from left and right buttocks below the waistline, along the epidural space from the T10 vertebra, and terminating at the C1 vertebra. Figure 6.1 illustrates the three imaging positions and the associated routing groups considered for each phantom.

CEM simulations of the RF-exposures were conducted by means of the finite difference time domain (FDTD) simulation platform, Sim4Life V2.0 (ZMT Zurich MedTech, Zurich, Switzerland). It was ensured that a steady-state was attained before the simulations were determinate. The phantoms were discretized with a maximum grid size of $2.0 \times 2.0 \times 2.0\ \mathrm{mm}^3$, and dielectric tissue properties at 64 MHz [137] were assigned to the tissues. All evaluations were performed at the normal MRI operating mode limit [20].

6.3.3 Evaluation

An elongated conductive AIMD behaves like an antenna, potentially accumulating RF power that is absorbed very locally, e.g., at the electrodes,

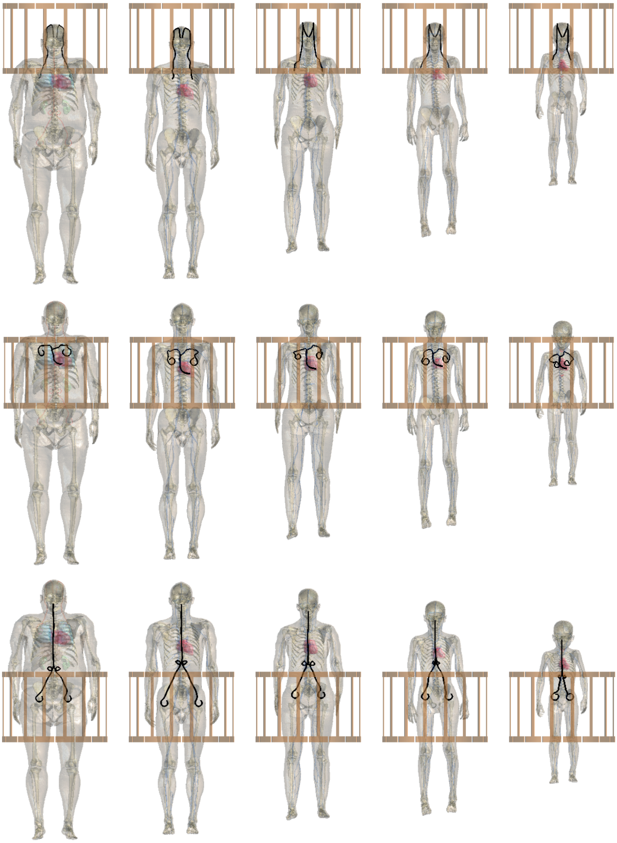

Figure 6.1: From left to right: ViP phantoms Fats, Duke, Ella, Billie, and Thelonious. Top: left and right deep-brain stimulator ($\mathrm{DBS_L}$ and $\mathrm{DBS_R}$) routing groups at the head-imaging position. Middle: left and right pacemaker ($\mathrm{PM_L}$ and $\mathrm{PM_R}$) routing groups at the thorax-imaging position. Bottom: left and right spinal-cord stimulator ($\mathrm{SCS_L}$ and $\mathrm{SCS_R}$) routing groups at the pelvis imaging position.

and may pose a risk to the patient due to very local thermal tissue damage. A four-tier approach to the evaluation of risk of RF-induced local tissue-heating for a large variety of AIMDs has been defined by [1]. All four tiers are designed to be conservative, with decreasing overestimation and increasing complexity of evaluation as a function of increasing tier number. Tier 1 and 2 can be used to assess only electrically short AIMDs; Tier 3 is the most practical approach, as it allows for experimental generation of a field-response model of the AIMD that can be combined with the induced field in the body along any implant trajectory, i.e., requiring only the fields induced in the patient without implants. This allows evaluation of millions of exposure configurations. The highest Tier, Tier 4, provides the most accurate estimation of local power deposition via full modeling of the clinical scenarios. However, until now, this approach is practical only for very short and mainly passive implants due to computational limitations; a typical AIMD would require μm resolution in a multi-meter domain. The impact of using ViP 3.0 versus ViP 1.x has been evaluated for all four tiers.

Tier 1 and Tier 2 evaluations

In the Tier 1 approach, the AIMD-induced enhancement is evaluated for a uniform incident field with a strength pre-defined in the ISO/TS specification. This value corresponds to the maximum induced spatial peak 10g-averaged E_{RMS} fields (hereafter, referred to as E_{10g}) estimated to occur at the SAR limits of MRI normal operating mode, i.e.: head SAR less than 3.2 W/kg, whole body SAR less than 2 W/kg, partial body SAR less than 2-10 W/kg (depending on the exposed patient mass) [20]. The E_{10g} values were derived from four ViP 1.x phantoms (Fats, Louis, Ella, and Duke) inside an RF cylindrical body coil operating at 64 MHz, at head through knee imaging positions.

The Tier 2 approach differs from that of Tier 1, in that E_{10g} is derived from user-defined exposure conditions (i.e., without specific patient and imaging positions are defined for Tier 2 in ISO/TS [2012]) in the region of the body where the AIMD is located. The maximum 95^{th} percentile of E_{10g} across all conditions considered concludes the incident field condition for Tier 2 evaluation

We defined $\text{p}_p E_{\text{10g}}$ as the p-th percentile of E_{10g} computed within a volume of interest. The E_{10g} was computed using a method consistent with IEEE C95.3 [138]. At each voxel of the body model, a 10 g averaging volume in the shape of a cube was found by expanding the cube in all directions from the centre voxel until the mass reaches 10 g. The uncertainty of E_{10g} evaluation was determined on the basis of the modeling parameters uncertainties from [67] as 0.5 dB.

For the Tier 1 evaluation, $p = 99$ was chosen to avoid the spatial locations with an irregular averaging volume of E_{10g} (e.g., fingers) and $\mathrm{p}_{99}E_{\text{10g}}$ within the whole body of each phantom was computed for the head-, thorax-, and pelvis-imaging positions shown in Figure 6.1.

For the Tier 2 evaluation, the exposure of the pacemaker AIMD was evaluated, and the incident conditions for the AIMD PM region — defined as the volume encompassing both $\mathrm{PM_L}$ and $\mathrm{PM_R}$ routings — were evaluated. The PM region is illustrated in Figure 6.2 for the ViP phantom Duke. The $\mathrm{p}_{95}E_{\text{10g}}$ within the PM region of each phantom was computed for the three imaging positions, and the maximum $\mathrm{p}_{95}E_{\text{10g}}$ g across all exposure conditions (patients and imaging positions) is defined as the Tier 2 *in vivo* incident condition for the PM region.

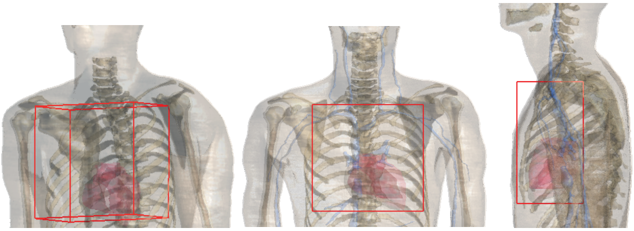

Figure 6.2: Pacemaker active implantable medical device (AIMD) evaluation area (PM region) used in Tier 2 evaluation, illustrated for the Virtual Population (ViP) phantom Duke.

Tier 3 evaluation

In the Tier 3 evaluation, the *in vivo* local power deposited in the tissue caused by AIMD is estimated from:

$$P_{\text{dep}} = W_0 \left(\int_0^L h(l)\, E_{\text{tan}}(l)\, dl \right) \left(\int_0^L h(l)\, E_{\text{tan}}(l)\, dl \right)^* \tag{6.1}$$

where $h(l)$ is the E-field transfer function of the AIMD [49], and $E_{\text{tan}}(l)$ is the tangential component of the incident E-field along the implant routings. Both quantities are defined along the routing length, l. W_0 is the power deposited at the vicinity of the electrodes when the implant is exposed to an incident E-field of constant amplitude and phase (E_{tan} = 1 V·m^{-1}).

For each of the implant routing groups previously defined (DBS$_{\text{L}}$, DBS$_{\text{R}}$, PM$_{\text{L}}$, PM$_{\text{R}}$, SCS$_{\text{L}}$, and SCS$_{\text{R}}$), 100 routings were randomly generated. For each exposure condition, $E_{\text{tan}}(l_1)$ was extracted from ViP 1.x and 3.0 and the local RF-induced power deposition of each implant routing (P_{dep}) was estimated from (6.1). The predictive RF heating model, $h(l)$ and W_0 of generic AIMDs, represented by insulated wires of three different lengths (40, 60, or 80 cm depending on the length of the AIMD routings in each ViP phantom) were assumed. The insulated wires comprise a 1.5 mm diameter conductor and 0.5 mm-thick insulation layer, with insulation at the distal termination removed over a length of 10 mm, the other termination is capped. W_0 and $h(l)$ of the generic AIMDs were characterized according to [96].

Tier 4 evaluation

Tier 4 evaluation requires a numerical model that approximates the actual clinical scenario, and therefore the implant model is incorporated into the body model. The evaluation is straightforward but is computationally demanding, as the multi-scale structures must be sufficiently resolved to provide accurate results of the electromagnetic interactions between the RF exposure and implant embedded in the complex anatomy. This means that the safety evaluation cannot be performed for a comprehensive set of clinical scenarios (e.g., permutations of multiple imaging positions, patients, and AIMD routings) at reasonable computing cost. Therefore, only the Duke phantom from the ViP 1.x and 3.0 was considered in the Tier 4 analysis.

For the Tier 4 evaluation, one of the 100 randomly generated routings for the Tier 3 evaluation was selected per routing group, and six clinical scenarios — DBS$_{\text{L}}$ and DBS$_{\text{R}}$ at head imaging position; PM$_{\text{L}}$ and PM$_{\text{R}}$ at thorax imaging position; and SCS$_{\text{L}}$ and SCS$_{\text{R}}$ at pelvis imaging position — were defined for the phantom. The insulated wires, previously described for the Tier 3 evaluation, were incorporated into the phantom along the six selected routings, and a full-wave FDTD simulation was then performed for each scenario. The power deposition was calculated from a volume integral of the power density contained within the -30 dB contour relative to the maximum deposition.

6.4 Results

6.4.1 Anatomical Comparison

As described in [131], ViP 1.x phantoms suffer from several shortcomings, including limitations in the local detail and accuracy of organ segmentation, insufficient tissue continuity between separately acquired and merged image regions, and inconsistent tissue classification and segmentation across the different phantoms. Most of these issues were addressed in ViP 3.0 phantoms, resulting in improved fidelity to the original patient data. As a consequence, the transition from ViP 1.x to ViP 3.0 introduced large anatomical differences over several regions of the body. Here, we summarize some of the most clearly identified differences in the tissue regions relevant to this study.

To be able to segment thin and small tissue structures without holes or stair-casing artifacts, and without exaggerating tissue thickness or volume, the sampling resolution in ViP 3.0 has been increased from $0.9\times0.9\times0.9$ mm^3 (ViP 1.x) to $0.5\times0.5\times0.5$ mm^3 by applying Lanczos interpolation [139] and more than 150 additional tissues have now been segmented in ViP 3.0 compared with ViP 1.x. After a review of ViP 1.x, a set of guidelines was established to ensure that ViP 3.0 segmentations are consistent irrespective of the operator performing the segmentation and the image dataset. As a result of the improved segmentation consistency in ViP 3.0, the standard deviation of the tissue number across different models decreased from 16.3 (ViP 1.x) to 2.7 (ViP 3.0). Figure 3 shows a comparison of how tendons and the circulatory system were segmented in ViP 1.x and ViP 3.0, revealing substantial inconsistencies in the tissue assignment of tendons, especially near the vertebrae, in ViP 1.x (Figure 3a) versus ViP 3.0 (Figure 3b). Consistency in tendon tissue mass ratio across different models in ViP 3.x are improved by more than 40% compared to ViP 1.x. With the improvements in the alignment and merging algorithms of the image stacks and the tissue assignment [131], the positions of some segmented tissues are shifted; the most significant change is about 5 mm, found in Ella, in the veins. The improved quality of the circulatory system of the ViP 3.0 is shown in Figure 3c and d. Compared with ViP 1.x, discontinuities in veins and arteries have been eliminated, and the segmentation of the circulatory network has been made consistent across all ViP 3.0 phantoms. The heights and masses of the discretized ViP 1.x and ViP 3.0 models are summarized in Table 1. A uniform grid size of $0.5\times0.5\times0.5$ mm^3 was used to compute the heights and masses. The differences in height and mass were 0 - 0.02 m and 0.1 -1.7 kg, respectively. With the improved segmentation, the mass error of the segmented models compared to the original scanned volunteers are decreased from 3.8% in ViP 1.x to 1.2% in ViP 3.0.

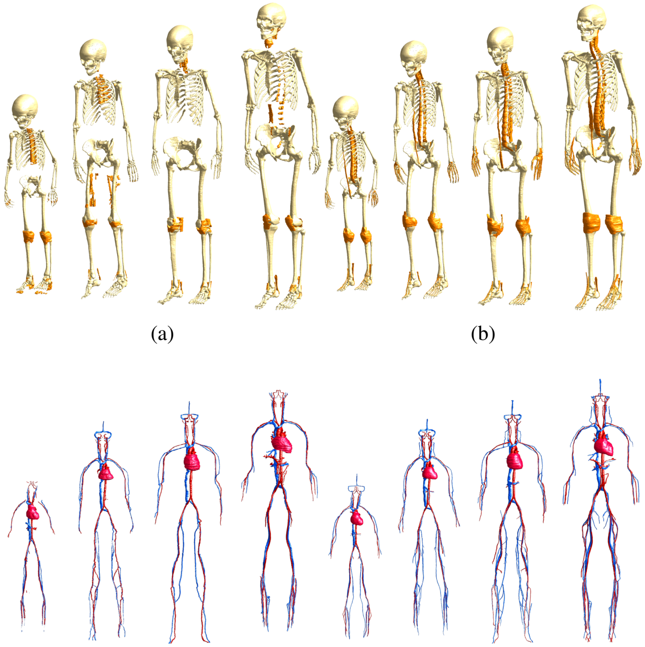

(a) (b)

(c) (d)

Figure 6.3: Improvements in the quality and consistency of tissue segmentation in Virtual Population (ViP) 3.0 compared with ViP 1.x phantoms: tendons of (a) ViP 1.x and (b) ViP 3.0; the circulatory system of (c) ViP 1.x and (d) ViP 3.0.

The improved quality of the segmentation of the ViP 3.0 leads to inter-

Table 6.1: Heights and Weights of the Five Phantoms Studied From ViP 1.0 and ViP 3.0, Obtained From Discretized Models With a Uniform Grid Size of 0.5x0.5x0.5 mm^3.

	Height (m)		Mass (kg)		$\|\|\Delta\|\|$ (%)		DOI (Prefix 10.13099/)	
Phantom	ViP 1.x	ViP 3.0	ViP 1.x	ViP 3.0	Height	Mass	ViP 1.x	ViP 3.0
Fats	1.84	1.82	119.4	119.5	1.1	<0.1	ViP-Fats-V1.1	ViP-Fats-V3.0
Duke	1.79	1.77	71.9	70.2	1.1	2.4	ViP-Duke-V1.1	ViP-Duke-V3.0
Ella	1.63	1.63	55.8	57.3	<0.1	2.7	ViP-Ella-V1.1	ViP-Ella-V3.0
Billie	1.49	1.49	34.7	34.0	<0.1	2.0	ViP-Billie-V1.1	ViP-Billie-V3.0
Thelonious	1.18	1.16	17.5	318.5	1.8	5.7	ViP-Thelonious-V1.3	ViP-Thelonious-V3.0

nal organ, e.g., lungs, liver and kidneys, of more realistic shapes that are clearly recognizable from the tissue distributions (Figure 6.4). The peak spatial averaged specific absorption rate (SAR) values averaged over 10 g (psSAR10g) were selected for local SAR distribution comparison, as this is defined by the safety guidelines [1] as relevant metric, and is supported by studies [140]. The optimal averaging strategy depends on factors such as the properties of the exposed tissue and the exposure, as evident from the tissue property dependence of the characteristic heating spread (e.g., quantified by length of decay of Green's function of the Pennes bioheat equation [47]). The psSAR10g at the thorax imaging position for circularly polarized B_1 excitation was computed. Differences of up to 5× (lower limbs) and 3× (upper body) were found between ViP 1.x and ViP 3.0 (Figure 6.4(d)).

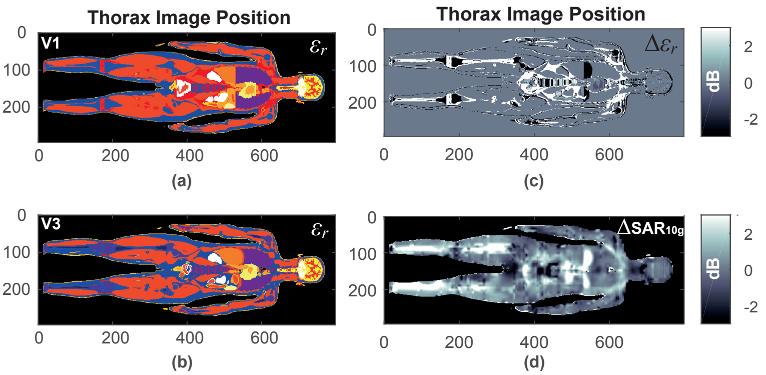
Thorax Image Position
V1
ε_r
0
100
200
0
200
400
600
(a)
V3
ε_r
0
100
200
0
200
400
600
(b)
Thorax Image Position
$\Delta\varepsilon_r$
0
100
200
0
200
400
600
(c)
dB
2
0
-2
ΔSAR10g
0
100
200
0
200
400
600
(d)
dB
2
0
-2

Figure 6.4: Improvements in the quality of tissue (permittivity ϵ_r is shown) and SAR_{10g} distributions in ViP 3.0 compared with ViP 1.x phantoms for the ViP phantom Ella: ϵ_r of (a) ViP 1.x and (b) ViP 3.0; (c) difference in tissue permittivity distribution ($\Delta\epsilon_r$) between ViP 1.x and ViP 3.0; (d) difference in SAR_{10g} distribution (ΔpsSAR10g) between ViP 1.x and ViP 3.0.

6.4.2 Tier 1 and Tier 2 Evaluations

The $\mathrm{p}_{99}E_{10g}$ obtained at the normal MRI operating mode limit [IEC, 2010] for all phantoms and imaging positions are summarized in Table 6.2 and

Figure 6.5(a). The maximum $\mathrm{p}_{99}E_{\text{10g}}$ across all considered exposures is identified as the Tier 1 in vivo incident condition. The values derived from ViP 1.x and 3.0 are 237 $\mathrm{V{\cdot}m^{-1}}$ and 235 $\mathrm{V{\cdot}m^{-1}}$, respectively, showing a difference of less than 0.1 dB ($\pm$1.5%). The largest difference (1.1 dB $\pm$13%) in $\mathrm{p}_{99}E_{\text{10g}}$ was found in Fats at the head-imaging position. The variation across the phantoms, $|\Delta_{\text{ViP}}|$, is higher in all exposure scenarios, i.e., 1.4 – 3.4 dB (confidence interval of (-15%, +17%) to (-32%, +48%)). The influence of anatomical variation within the patient population on worst-case whole-body exposure is considerably higher than that of the model fidelity.

Similar results are seen for the Tier 2 evaluation: the $\mathrm{p}_{95}E_{\text{10g}}$ within the PM region for all phantoms and imaging positions is summarized in Table 6.3 and Figure 6.5(b). The Tier 2 in vivo incident conditions derived from ViP 1.x and ViP 3.0 are both 177 $\mathrm{V{\cdot}m^{-1}}$ — a difference of less than 0.1 dB ($\pm$1.5%). The largest difference in $\mathrm{p}_{95}E_{\text{10g}}$ 1.0 dB ($\pm$12%) was found in Ella at the pelvis imaging position. Once again, the variation across the phantoms, $|\Delta_{\text{ViP}}|$, is considerably larger, i.e., 2.2 – 5.9 dB (confidence interval of (-22%, +29%) – (-49%, +97%)), indicating that the influence of anatomical variation within the patient population on the worst-case regional exposure exceeds that of the model fidelity.

6.4.3 Tier 3 Evaluation

For each phantom of the ViP 1.x and 3.0, the $E_{\text{tan}}(l_1)$ of six exposure scenarios (Figure 6.1) were evaluated. Local differences of $E_{\text{tan}}(l_1)$ as large as 3 dB (confidence interval of (-29%, +41%)) were found between ViP 1.x and 3.0. The $E_{\text{tan}}(l_1)$ comparison of the ViP phantom Ella is depicted in Figure 6.6.

Next, the local power deposition, P_{dep}, was calculated from (6.1) for ViP 1.x and 3.0. The distributions of P_{dep} for the six exposure conditions obtained with the five ViP 1.x and 3.0 models is compared in Figure 6.7; the 95th percentile values of P_{dep} of each phantom, as well as the variation across the phantoms, for each exposure condition are summarized in Tables 6.4 – 6.6. The maximum difference in the 95^{th} percentile values of ViP 1.x and 3.0 was 1.0 dB (confidence interval of $\pm$25%), found in Ella for $\mathrm{PM_R}$. The variation across the patient population taking into account all positions and routings was between 3 – 11 dB (confidence interval of (-50%, +99%) – (-92%, +1160%)), depending on the exposure scenarios and, considerably higher than the differences between ViP 1.x and 3.0.

Table 6.2: $\mathrm{p}_p E_{\mathrm{10g}}$ (99th Percentile of the 10g-Average E-field) at head, thorax, and pelvis imaging positions. Tier 1 exposures are indicated in bold.

Tier 1: $\mathrm{p}_p E_{\mathrm{10g}}$ ($p = 99$) at the normal MR operating mode ($\mathrm{V{\cdot}m^{-1}}$)									
	Head		Thorax		Pelvis		$\|\|\Delta\|\|$ (dB) (Confidence interval (%))		
Phantom	ViP 1.0	ViP 3.0	ViP 1.0	ViP 3.0	ViP 1.0	ViP 3.0	Head	Thorax	Pelvis
Fats	157	139	207	201	**237**	**235**	1.1 (±13%)	0.3 (±3.5%)	$<$ **0.1** (±**1.5%**)
Duke	127	118	160	153	190	184	0.6 (±7.0%)	0.4 (±5.0%)	0.3 (±3.5%)
Ella	122	119	177	181	207	214	0.2 (±2.5%)	0.2 (±2.5%)	0.3 (±3.5%)
Billie	136	125	171	166	208	193	0.7 (±8.4%)	0.3 (±3.5%)	0.6 (±7.0%)
Thelonious	130	133	140	156	163	179	0.2 (±2.5%)	1.0 (±12.5%)	0.8 (±9.6%)
$\|\|\Delta_{\mathrm{ViP}}\|\|$ (dB)	1.6	2.7	2.6	2.9	2.5	2.7	-	-	-
(Confidence interval (%))	(-22, +29)	(-15,+17)	(-32,+48)	(-24,+32)	(-31,+46)	(-24,+32)	-	-	-

Table 6.3: $\mathrm{p}_p E_{\mathrm{10g}}$ (95th Percentile of the 10g-Average E-field) Within the Evaluation Area Containing the Pacemaker AIMD (PM region) at Head-, Thorax-, and Pelvis-Imaging Positions Tier 2 exposures are indicated in Bold.

Tier 2: $\mathrm{p}_p E_{\mathrm{10g}}$ ($p = 95$) at the normal MR operating mode (V·m^{-1})									
	Head		Thorax		Pelvis		$\|\|\Delta\|\|$ (dB) (Confidence interval (%))		
Phantom	ViP 1.0	ViP 3.0	ViP 1.0	ViP 3.0	ViP 1.0	ViP 3.0	Head	Thorax	Pelvis
Fats	103	101	**177**	**177**	44	42	0.2 (±2.5%)	$<$ **0.1** (±**1.5%**)	0.4 (±5%)
Duke	59	61	143	138	35	33	0.2 (±2.5%)	0.3 (±3.5%)	0.3 (±3.5%)
Ella	84	82	155	159	37	41	0.1 (±1.5%)	0.2 (±2.5%)	1.0 (±12.5%)
Billie	106	96	147	1642	42	44	0.9 (±11%)	0.3 (±3.5%)	0.3 (±3.5%)
Thelonious	109	120	128	142	58	62	0.8 (±9.6%)	0.9 (±11%)	0.5 (±5.9%)
$\|\|\Delta_{\mathrm{ViP}}\|\|$ (dB)	5.3	5.9	2.8	2.2	4.5	5.4	-	-	-
(Confidence interval (%))	(-46, +84)	(-49,+97)	(-28,+28)	(-22,+28)	(-40,+59)	(-46,+86)	-	-	-

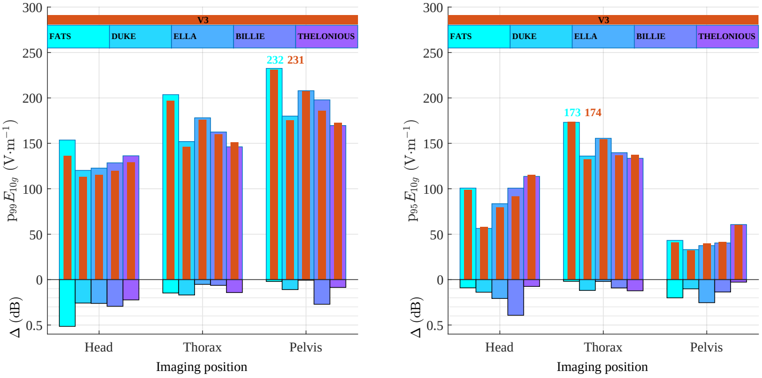

(a) (b)

Figure 6.5: Visual depiction of the information in Tables 6.2 and 6.3: (a) $\mathrm{p}_{99}E_{10\mathrm{g}}$ with the derived Tier 1 incident values and (b) $\mathrm{p}_{95}E_{10\mathrm{g}}$ with the derived Tier 2 incident values within the pacemaker at the normal MRI operating mode limit for the head-, thorax-, and pelvis-imaging positions; the bars illustrate the $\mathrm{p}_pE_{10\mathrm{g}}$ for each ViP phantom, with the value derived from ViP 3.0 indicated by the orange inset bar. Lower y axis: the difference $\Delta\mathrm{p}_pE_{10\mathrm{g}}$ in dB between ViP 1.x and ViP 3.0.

Table 6.4: Tier 3 power deposition, evaluated for the AIMD along DBS_L and DBS_R at the head imaging position. The 95^{th} percentile value of P_dep are summarized for ViP 1.0 and ViP 3.0. $||\Delta||$ is the absolute value of the difference in 95^{th} percentile of P_dep for ViP 1.0 and ViP 3.0. $||\Delta_\text{ViP}||$ indicates the variation of P_dep across the patient population.

Tier 3: 95^{th} percentile of P_dep for DBS routings at head imaging position						
	DBS_L (mW)		DBS_R (mW)		$\|\|\Delta\|\|$ (dB) (Confidence interval (%))	
Phantom	ViP 1.0	ViP 3.0	ViP 1.0	ViP 3.0	DBS_L	DBS_R
Fats	89.6	82.2	10.4	10.4	0.4 (±9.6%)	< 0.1 (±2.3%)
Duke	74.7	72.6	47.7	46.8	< 0.1 (±2.3%)	< 0.1 (±2.3%)
Ella	80.4	83.2	23.3	20.9	< 0.1 (±2.3%)	<0.5 (±12.2%)
Billie	76.3	79.8	31.7	31.2	< 0.1 (±2.3%)	< 0.1 (±2.3%)
Thelonious	42.8	45.6	20.5	23	0.3 (±7.0%)	0.5 (±12.2%)
$\|\|\Delta_\text{ViP}\|\|$ (dB) (Confidence interval (%))	3.2 (-51, +109)	2.6 (-45,+82)	6.6 (-78,+357)	6.5 (-78,+347)	- -	- -

Table 6.5: Tier 3 power deposition, evaluated for the AIMD along PM_L and PM_R at the head imaging position. The 95^{th} percentile value of P_dep are summarized for ViP 1.0 and ViP 3.0. $||\Delta||$ is the absolute value of the difference in 95^{th} percentile of P_dep for ViP 1.0 and ViP 3.0. $||\Delta_\text{ViP}||$ indicates the variation of P_dep across the patient population.

Tier 3: 95^{th} percentile of P_dep for PM routings at thorax imaging position						
	PM_L (mW)		PM_R (mW)		$||\Delta||$ (dB) (Confidence interval (%))	
Phantom	ViP 1.0	ViP 3.0	ViP 1.0	ViP 3.0	PM_L	PM_R
Fats	29.9	27.5	27.5	28.1	0.4 (±9.6%)	< 0.1 (±2.3%)
Duke	47.5	46.4	17.6	16.9	< 0.1 (±2.3%)	0.2 (±4.7%)
Ella	26.4	29.4	6.8	8.4	0.5 (±2.2%)	1.0 (±25.8%)
Billie	28.5	28.3	15.5	15.3	< 0.1 (±2.3%)	< 0.1 (±2.3%)
Thelonious	16.2	3.6	3.6	3.8	0.3 (±7.0%)	0.2 (±4.7%)
$||\Delta_\text{ViP}||$ (dB)	4.7	4.9	8.8	8.7	-	-
(Confidence interval (%))	(-66, +195)	(-68,+209)	(-87,+658)	(-87,+641)	-	-

Table 6.6: Tier 3 power deposition, evaluated for the AIMD along SCS_L and SCS_R at the head imaging position. The 95^{th} percentile value of P_dep are summarized for ViP 1.0 and ViP 3.0. $||\Delta||$ is the absolute value of the difference in 95^{th} percentile of P_dep for ViP 1.0 and ViP 3.0. $||\Delta_\text{ViP}||$ indicates the variation of P_dep across the patient population.

Tier 3: 95^{th} percentile of P_dep for SCS routings at pelvis imaging position						
	SCS_L (mW)		SCS_R (mW)		$\|\|\Delta\|\|$ (dB) (Confidence interval (%))	
Model	ViP 1.0	ViP 3.0	ViP 1.0	ViP 3.0	SCS_L	SCS_R
Fats	43.1	40.3	30.6	31.8	0.3 (±7.0%)	0.2 (±4.7%)
Duke	28.9	25.2	29.7	27.1	0.6 (±14.8%)	0.4 (±9.6%)
Ella	29.2	29.2	38.7	36.8	< 0.1 (±2.3%)	0.2 (±12.2%)
Billie	25.2	24.0	39.0	36.5	0.2 (±4.7%)	0.3 (±7.0%)
Thelonious	3.3	3.2	8.9	8.9	0.2 (±4.7%)	<0.1 (±2.3%)
$\|\|\Delta_\text{ViP}\|\|$ (dB) (Confidence interval (%))	11.1 (-92, +1188)	11.0 (-92,+1158)	6.5 (-78,+347)	6.2 (-76,+317)	- -	- -

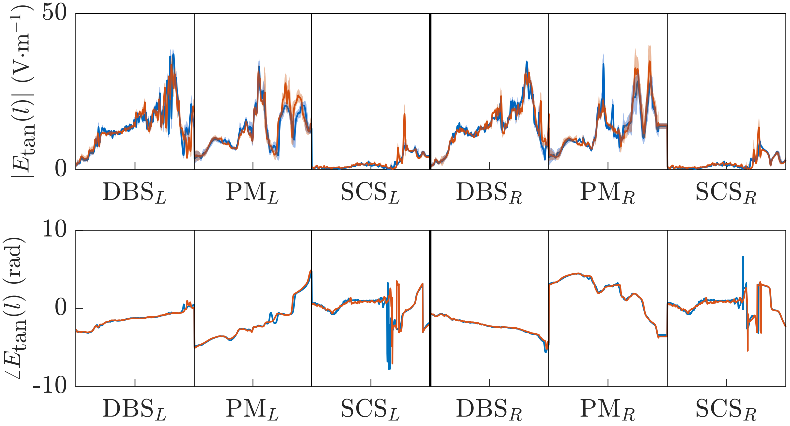

Figure 6.6: Magnitude (top) and phase (bottom) of $E_{\text{tan}}(l_1)$ averaged over 100 routings (solid lines) and the variations within 100 routings (shaded regions) for each routing group in the Virtual Population (ViP) phantom Ella with ViP 1.x results in blue and ViP 3.0 results in orange.

6.4.4 Tier 4 evaluation

The local power deposition calculated for all six AIMDs in Duke by means of the Tier 4 approach is summarized in Table 6.7. The differences between ViP 1.x and ViP 3.0 across all evaluated scenarios are less than 0.7 dB ($\pm 16\%$). Figure 6.8 summarizes the results from the Tier 4 evaluation of the left generic deep-brain stimulator AIMD, DBS$_{\text{L}}$, in Duke at the head imaging position. SAR distributions in a sagittal plane through the electrode of the DBS$_{\text{L}}$ are shown for ViP 1.x and ViP 3.0. Histograms of SAR within the tissue region at close proximity to the distal tip of the DBS$_{\text{L}}$ show similar distribution for ViP 1.x and ViP 3.0.

6.4.5 Discussions

For evaluations on the whole-body scale, the differences in $\text{p}_{99}E_{\text{10g}}$ (99^{th} percentile of the 10 g-average E-field) obtained with ViP 1.x and ViP 3.0

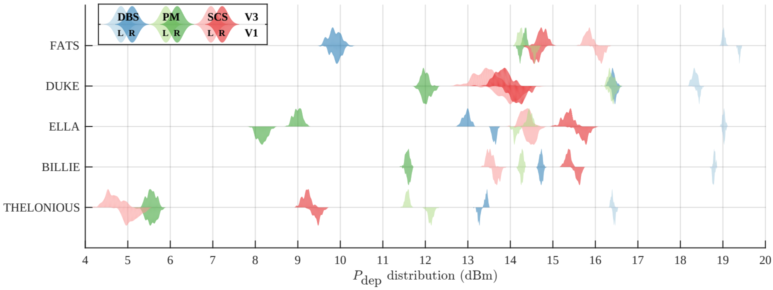

Figure 6.7: Distribution of Tier 3 power deposition (P_{dep}) for deep brain stimulator (DBS) (blue), pacemaker (PM) (green), and spinal cord stimulator (SCS) (red) active implantable medical devices (AIMDs) in all five Virtual Population (ViP) 1.x (lower histogram) and ViP 3.0 (upper histogram) phantoms.

are <0.8 dB (confidence interval of ±9.6%), all of which can be explained by the effect of improved segmentation. More stable values can be expected when sampling the position with finer resolution. It must be noted that these findings are not inconsistent with the published and widely applied Tier 1 values, as these values remain conservative for testing implants, and, furthermore, the differences between ViP 1.x and ViP 3.0 are much smaller than the observed variation across the five phantoms of 2 – 6 dB (confidence interval of (-21%, + 26%) – (-50%, +100%)).

For local evaluations, considerable (>3 dB or confidence interval of larger than (-29%, +41%)) deviation in the tangential E-fields were found for Tier 3 evaluation. The results of this study show that all differences can be explained by local anatomical differences and the more precise and consistent tissue segmentation in ViP 3.0. Hence, detailed and accurate segmentation is key for accurate representation of the actual patient, especially when local effects are of relevance.

For evaluations involving an integral throughout the anatomy, as for Tier 3 evaluation of deposited power, the differences were always ≤1 dB (confidence interval of ±25%). These differences were consistently caused by the changes in segmentation and tissue assignments. For example, the largest difference observed in PM_{R} of Ella is caused by the differences in the po-

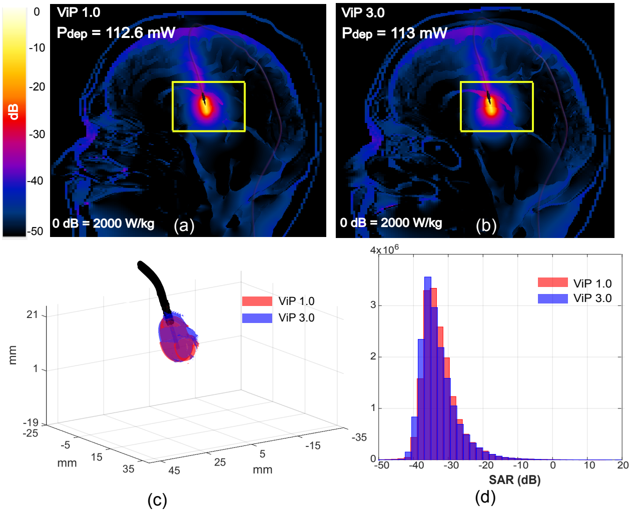

Figure 6.8: Tier 4 evaluation of the left generic deep-brain stimulator (DBS_L) active implantable medical device (AIMD) in Duke at the head-imaging position. Specific absorption rate (SAR) distribution in a sagittal plane through the tip of active implantable medical device (AIMD) for (a) Virtual Population (ViP) 1.x and (b) ViP 3.0; (c) the surface enclosing the tissue volume at the vicinity of the distal tip of the DBS_L AIMD with the local SAR contained tissue volume within the -30 dB contour line relative to the maximum SAR of ViP 1.x (red) and ViP 3.0 (blue); (d) histogram of SAR within the tissue region at close proximity to the distal tip of the DBS_L AIMD (shown as a yellow box in (a) and (b) for ViP 1.x (red) and ViP 3.0 (blue).

Table 6.7: Tier 4-estimated *in vivo* power deposition obtained with Duke phantom of ViP phantom Duke for the selected clinical scenarios. $||\Delta||$ is the absolute value of the difference in the Tier 4-estimated *in vivo* power deposition of ViP 1.0 and ViP 3.0.

	Tier 4: *in vivo* power deposition at the normal MR operating mode		
AIMD	ViP 1.0 (mW)	ViP 3.0 (mW)	$||\Delta||$ (dB) (Confidence interval (%))
DBS_L	112.6	113.0	0.07 (±1.6)
DBS_R	90.0	91.0	0.05 (±1.1)
PM_L	39.1	39.4	0.04 (±0.9)
PM_R	23.3	24.3	0.17 (±4.0)
SCS_L	17.0	19.0	0.48 (±12)
SCS_R	18.8	22.0	0.64 (±16)

sitions of segmented veins between ViP 1.x and ViP 3.0. Once again, the variation across the ViP phantoms is considerably larger, with differences of 3 – 11 dB (confidence interval of (-29%, +41%) – (-72%, +255%) and (-50%, +99%) – (-92%, +1160%) for field and power, respectively) found among the exposure scenarios considered. The finer tissue and organ details of ViP 3.0 lead to an increase of about 15% in the voxelling and computational time required, compare to that required for ViP 1.x.

It must be noted that the Tier 3 evaluation of *in vivo* power deposition reported in this study is based on a generic AIMD model that is derived under simplified conditions. It is intended for comparative analysis only, and the absolute values of the deposited power reported here cannot be considered representative of the RF-induced heating of any specific commercial AIMDs. The differences for any specific AIMD model may vary from what is reported here, as it also depends on the characteristics of $h(l)$ [1]. The study was limited to a single birdcage configuration. However, it has been shown that the volume birdcages installed in all MRI scanners can be well represented with a library of birdcages of different dimensions and configurations [61, 141]. As the volumetric extension of the generated EM-fields varies with the birdcage design, it changes the globally induced field distributions when normalized to the whole-body and partial-body limits but not the local differences due to segmentation differences. Therefore, the findings of this study are valid for any birdcage configuration.

Furthermore, the results provided in this study cannot be applied to investigations of contributions to uncertainty other than segmentation and tissue assignment, such as (i) the simplification made in the assumption of homogeneous and constant tissue properties throughout each individual tissue and organ, (ii) the introduction of sharp tissue interfaces, and (iii) the variability associated with the dielectric properties of tissues.

The objective of the study was only to access the uncertainties related to the generation of the initial, non-posed or morphed models, i.e., related to segmentation and tissue assignment in the imaging conditions, and not the effects related to changes of the organ shape and movement as a function of posture and breathing or changes introduced by additional implants (e.g., hip implants). The local field variations caused by these effects can be large, i.e., on order of those due to variations between models.

6.4.6 Conclusions

The availability of two generations of the same ViP phantoms allows us to establish for the first time the uncertainty associated with segmentation and tissue assignment. The results show that differences between ViP 1.x and ViP 3. 0 on dosimetric endpoints are larger than anticipated, all of which are consistent with the revisions in segmentation and tissue assignment.

The differences exceeded 3 dB (confidence interval of (-29%, +41%)) for local quantities (e.g., tangential E-fields along AIMD) and 1 dB (confidence interval of ±12% and ±25% for field and power, respectively) for integrated and volume-averaged quantities (e.g., estimated AIMD-heating and 10g-average E-fields). We conclude that the phantom uncertainty associated with tissue assignment and segmentation quality/consistency can be larger than 3 dB (confidence interval of (-29%, +41%)) and 1 dB (confidence interval of ±12% and ±25% for field and power, respectively) for the assessment of local and integrated/averaged quantities, respectively. The uncertainty contribution of 0.6 dB or ±15% ($k = 1$) associated with tissue assignment and segmentation is estimated for AIMD-heating evaluation. By increasing the sample size of the phantoms that are based on different data sets i.e., from different volunteers, the uncertainties associated with random segmentation-related tolerances/inaccuracies may be further reduced.

Although not negligible, the difference between phantom generations is small in comparison to the variation across different ViP phantoms of the same generation, which can exceed 10 dB (confidence interval of (-68%, +217%) and (-90%, +900%) for field and power, respectively). Therefore, it is necessary to examine multiple phantoms covering the targeted population that are based on different patients to be able to achieve quantitative analysis of dosimetric endpoints (e.g., AIMD-heating) that depend on patient anatomy. Despite the comparatively small difference between ViP generations, it is encouraged that the available phantoms with the highest fidelity in segmentation be used, as these ensure results with the lowest uncertainty and possible underestimation of the exposure. To verify that the uncertainty monotonically decreases with improved phantom quality, evaluation of the differences between phantom generations should be repeated any time segmentation is improved.

Chapter 7

Standardized, Validated and Effective Safety Assessment of Patients with Medical Implants under MRI Exposure Using A Comprehensive Data Library Combined with an Analytics Toolset

7.1 Abstract

[1]The radiofrequency (RF) induced heating for patients with implants during exposure to magnetic resonance imaging (MRI) is a complex function

---

[1] This Chapter has been published in [142]

of multiple factors, e.g., the characteristics of the implant, patient anatomy, imaging position, RF coil, etc. A comprehensive safety assessment cannot be derived from the limited scenarios possible in clinical trials. We have established an *in silico* safety assessment trial that comprises a data library with a data analytics toolset to perform a comprehensive evaluation in a timely and traceable manner. We demonstrated the workflow for RF-induced heating evaluation for patients with medical implants.

7.2 Introduction

For patients with medical implants, the magnitude of radiofrequency (RF) induced heating during magnetic resonance imaging (MRI) amounts to a multitude of variables specific to the MRI system (e.g., RF-coil design and manufacturing details), patient anatomy, and imaging positions. Therefore, clinical trials performed with a limited number of scenarios are likely to be insufficient to ensure patient safety. It is essential that a standardized framework that provides not only relevant but also comprehensive, consistent, extendable, and traceable results be established to facilitate the establishment of a corroborated knowledge base build upon existing and emerging results. To that end, we report here the formulation of a standardized workflow that requires 1) a data library of the RF-induced fields inside the human body, 2) digital representations of the clinical routings of implants, 3) an implant RF-heating transfer function (Tier 3 model), and 4) a data analytics toolset. In this work, an *in silico* trial for RF-heating evaluatioin of generic implants during 1.5 T MRI exposure is demonstrated.

7.3 Methods

Figure 7.1 illustrates the proposed workflow, which is comprised of the following components:

- RF-exposure data library: This component provides pre-computed RF-induced fields inside a variety of patients during MRI exposures. The library comprises the exposure of a population of virtual patients (different patient anatomy) of the Virtual Population (ViP) [131] to a set of generic RF cylindrical body-coils at different clinical imaging positions.

- Implant-specific objects: This component includes the digital representations of clinical routings of the implants under test (IUT) as well as the Tier 3 model for RF-induced heating of the IUT, which defines the transfer function of RF-induced characteristics [1].

- Data filter: This component allows the user to select the specific dataset for each *in silico* trial.

- Data processing module: This component is a software module for generation of clear and traceable digital evidence.

- Output data/results: This component provides the results of the *in silico* trial as a traceable output available for analysis.

  This workflow is designed to allow each component within the workflow to be independently revised and evolved.

We apply the proposed construct to evaluate the RF-induced heating of a 60-cm generic spinal cord stimulator IUT exposed to 1.5 T MRI. Figure 7.2 summarizes the data filter used to define the selection of the trial.

Safe RF exposure conditions for commercial AIMDs are expressed in terms of both SAR and B_{1+} levels[143]. Therefore, the local deposited power of the IUT is evaluated at the normal operating mode SAR limits[20] and as well as at a fixed B_{1+} level.

The results were investigated further to indicate scenarios that may improve patient safety and image quality. As an example, a set of the following constraints on the IUT power deposition, B_{1+} homogeneity, and B_{1+} magnitude, is imposed on the output data/results of the RF-induced heating assessment:

1. B_{1+} level, measured by the average magnitude of B_{1+} over the iso-center slice of the RF-coil, is at least 90% of that provided by circularly-polarized (CP) B_1.

2. B_{1+} homogeneity, measured by the coefficient of variation of B_{1+} [144] over the iso-center slice of the RF-coil, does not exceed 10%.

3. The power deposition of the IUT does not exceed 300 mW.

Concisely:

$$\langle|B_{1+}(\epsilon,\tau)|\rangle \geq 0.9 \times \langle|B_{1+}(45^o,\tau)|\rangle \tag{7.1}$$

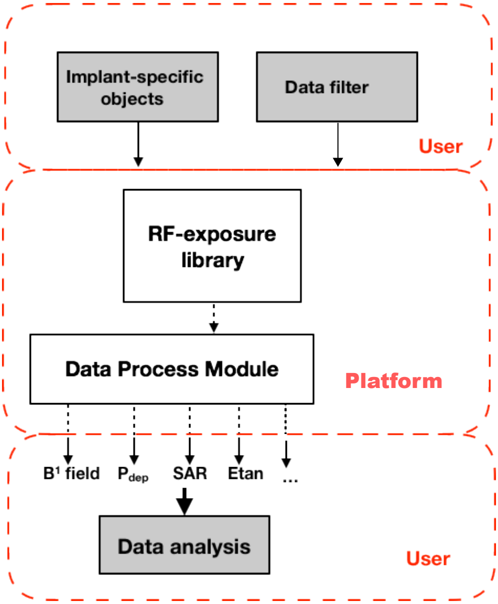
Implant-specific objects
Data filter
User
RF-exposure library
Data Process Module
Platform
B¹ field
Pdep
SAR
Etan
...
Data analysis
User

Figure 7.1: Proposed *in silico* trial workflow based on the IEC standard for patients without medical implants[20] and Tier 3 evaluation of RF-induced effects for patients with medical implants[1]

$$B_{1+,cov}(\epsilon,\tau) \leq 0.1 \tag{7.2}$$

$$P_{\text{dep}}(\epsilon,\tau) \leq 0.3 \tag{7.3}$$

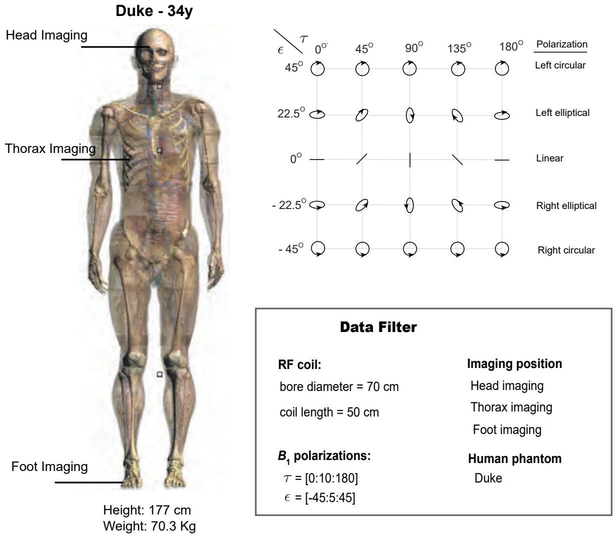
Duke - 34y
Head Imaging
Thorax Imaging
Foot Imaging
Height: 177 cm
Weight: 70.3 Kg
τ
ϵ
0°
45°
90°
135°
180°
Polarization
45°
Left circular
22.5°
Left elliptical
0°
Linear
- 22.5°
Right elliptical
- 45°
Right circular
Data Filter
RF coil:
bore diameter = 70 cm
coil length = 50 cm
B_1 polarizations:
τ = [0:10:180]
ϵ = [-45:5:45]
Imaging position
Head imaging
Thorax imaging
Foot imaging
Human phantom
Duke

Figure 7.2: Summary of the data selection for the *in silico* trial. Bottom-right: data filter. Left: illustration of phantom 'Duke' indicating the three imaging positions. Upper-right: Ellipticity (ϵ) and orientation (τ) angles represented on planar projection of the Poincaré sphere [94].

7.4 Results

Figure 7.3 shows the distribution of power deposition of the IUT as a function of B_1 polarizations, $P_{\text{dep}}(\epsilon, \tau)$, evaluated at the normal operating mode SAR limits and at a fixed B_{1+} level of 1μT.

Figure 7.3 also indicates that the circular-polarized B_1 guarantees neither maximum $\langle|B_{1+}(\epsilon,\tau)|\rangle$ nor minimum P_{dep}. Therefore, the above set of constraints (1)-(3) is imposed on the output of the trial to identify exposure scenarios that may improve either imaging quality and/or patient safety, while complying with normal operating mode SAR limits.

$\langle|B_{1+}(\epsilon,\tau)|\rangle$, $B_{1+,cov}(\epsilon,\tau)$, and $P_{\text{dep}}(\epsilon,\tau)$ that satisfy constraints (1)-(3) are enclosed within regions marked by the white dashed lines in Figure 7.4. The candidate exposures that may further improve scanning of patients equipped with this IUT are identified as intersections of the three qualified regions for each scenarios.

7.5 Conclusions

Through the establishment of a common data library and analysis tools, *in silico* trials can be performed to evaluate patient safety due to RF-implant interactions. Further, large clinical scenarios based on permutations of patients, imaging positions, RF coils, and implant clinical routings can be considered with a clear and traceable digital chain of custody.

We provide here an example *in silico* trial where a subset of the data from the common library was selected for IUT RF-heating evaluation. Further, the established workflow facilitates exploratory data analysis (EDA). EDA was performed on the trial's output and exposure conditions, where both imaging quality and patient safety can be maximized, were identified.

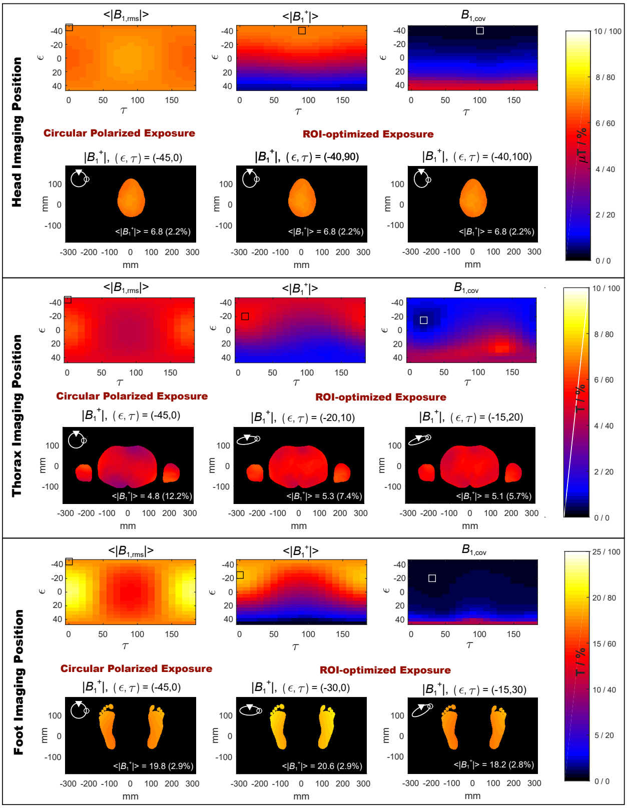

Figure 7.3: Data distribution for head, thorax, and foot imaging. Top-left and -right: distributions of power deposition of the IUT (P_{dep}) as a function of B_1 polarization at the normal operating mode SAR limits and at a fixed B_{1+} level of 1μT, respectively. Bottom-left: distribution of the B_{1+} magnitude averaged over iso-center slice ($\langle|B_{1+}|\rangle$) as a function of B_1 polarization at the normal operating mode SAR limits. Bottom-right: spatial distribution of B_{1+} magnitude over iso-center slice for circular-polarized B_1. The averaged magnitude and coefficient of variation of B_{1+} ($\langle|B_{1+}|\rangle$ and $B_{1+,cov}$) are indicated in μT and % at bottom-right of the figures.

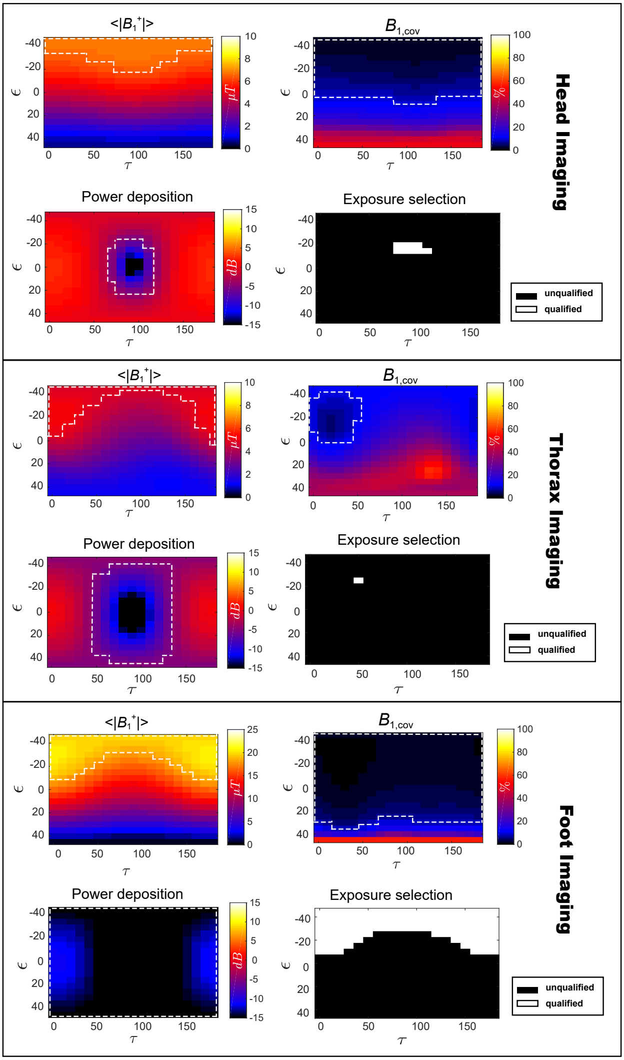

Figure 7.4: Data distribution for head, thorax, and foot imaging. For each imaging position, top-left, top-right, and bottom-left: distributions of B_{1+} magnitude averaged over iso-center slice ($\langle|B_{1+}|\rangle$), coefficient of variation of B_{1+} ($B_{1+,cov}$), and power deposition of the IUT (P_{dep}) as a function of B_1

Part V

Determination of the *in vivo* Temperature Increase

Chapter 8

Efficient and Reliable Assessment of the Maximum Local Tissue Temperature Increase at the Electrodes of Medical Implants under MRI Exposure

8.1 Abstract

[1]**Objective:** Standard risk evaluations posed by medical implants during magnetic resonance imaging (MRI) includes (1) the assessment of the total local electromagnetic (EM) power (P) absorbed in the vicinity of the electrodes and (2) the translation of P into a local *in vivo* tissue tempera-

---

[1] This Chapter has been published in [145]

ture increase ΔT ($P2\Delta T$) in animal experiments or simulations. We investigated the implant/tissue modeling requirements and associated uncertainties by applying full-wave EM and linear bio-heat solvers to different implant models, incident field conditions, electrode configurations, and tissue models. Results show that the magnitude of the power is predominately determined by the lead, while the power distribution, and the $P2\Delta T$ conversion, is determined by the electrode and surrounding tissues. $P2\Delta T$ is strongly dependent on the size of the electrode, the tissue type in contact with the electrode, and the tissue inhomogeneity (factor of $>$2 each) but less on the modeling of the lead ($< \pm 10\%$) and incident field distribution along the lead ($< \pm 20\%$). This was confirmed by means of full-wave simulations performed with detailed high-resolution anatomical phantoms exposed to two commonly used MRI clinical scenarios (64 MHz, 128 MHz), resulting in differences of $<6\%$. For the determination of $P2\Delta T$, only the electrode and the surrounding tissues must be modeled in great detail, whereas the lead can be modeled as a computationally efficient simplified structure exposed to a uniform field. The separate assessments of lead and electrode reduce the overall computational effort by several orders of magnitude. The errors introduced by this simplification can be considered by uncertainty terms.

8.2 Introduction

Patients undergoing magnetic resonance imaging (MRI) scans are exposed to static, gradient, and radiofrequency (RF) electromagnetic (EM) fields. The RF magnetic field components, at frequencies of 64 MHz (1.5T MRI) and 128 MHz (3.0T MRI), induce strong electric (E-) fields in the tissues of exposed patients, and the energy absorption causes both an increase in core temperature and the development of local temperature hotspots [146, 147, 61]. Whole-body and local tissue-specific absorption rates (SAR) and temperature increases for both general exposure and in MRI cases have been investigated [148, 67, 149]. In cases where patients have conductive implants, the implant couples with these induced fields, resulting in local amplification of these E-fields and, consequently, development of local hotspots [59, 26, 150, 151]. In general, the amplification is largest for resonant isolated leads of active medical implantable devices (AIMD) with small electrodes, e.g., neurostimulators and pacemakers. The local SAR can be several orders of magnitude higher than that caused by the external RF-coil alone [36, 152, 32, 37, 151]. As direct measurement of the *in vivo* tissue heating is possible only in animal studies, in vitro experiments and numerical simulations of *in vivo* conditions are often used to evaluate maximum *in vivo* tissue temperature increase [33, 26, 97, 153, 96].

The temperature increase, ΔT, measured in experimental phantoms does not accurately reflect the temperature increase inside the human body, not even when normalized to an equivalent amount of deposited power, P, due to large differences in the heat-transfer characteristics of the medium used in the test phantom compared to that of tissues *in vivo*. Phantoms can be used to approximate only either a single homogenous tissue or an average of tissue values over a larger volume, and no effects due to perfusion are take into account during the phantom measurements.

Today, the standard approach to determine the *in vivo* ΔT is performed in two steps:

i) translation of measured *in vitro* specific absorption rate (SAR) or ΔT into estimated local *in vivo* power deposition

ii) conversion of estimated local *in vivo* power deposition into estimated *in vivo* temperature changes

Step (i) can be performed according to ISO/TS 10974 [1] for each independent electrode, while step (ii) can be realized by means of the approach outlined in Annex F of [1] . However, simulations of the detailed AIMD for all relevant incident field conditions and tissue configurations can be computationally very costly. In [84], it was demonstrated that the local enhancements of electrically short implants can be well approximated with a radically simplified model of the implant. Here, we investigate the modeling simplifications that may be applied for long implants for evaluation of the maximum in vivo temperature increase at the electrodes of AIMD without substantial increase of the assessment uncertainty. The development of modeling simplifications that reduce demand for computational resources related to the complexity of implants (e.g., multiple helical leads) and the large variation in E-field incident conditions at the lead trajectories (that depend on anatomy, landmark positions, surrounding tissues, etc.) are extremely desirable. The working hypothesis of this study is that the lead and electrodes can be evaluated separately, i.e., the lead predominately determines the magnitude of the deposited power while the electrode and the surrounding tissues determine the power distribution and consequently the in vivo temperature – provided that the lead is electrically long ($> \lambda/2$) and the electrode is short ($< \lambda$/40, λ = 400 mm for 64 MHz and 200 mm for 128 MHz within the high permittivity medium defined in ISO/TS 10974: permittivity of 78, conductivity of 0.47 S/m). In this paper, we ignored the modeling requirements for the heat transfer via the lead, as it is generally low [97]. It should be further noted that the power deposition at each electrode must be determined separately if they are connected to individual wires, e.g., uni- versus bipolar AIMD [151].

8.3 Method

8.3.1 Deposited power-to-ΔT ($P2\Delta T$) factor

To quantify the conversion of *in vivo* power deposition to *in vivo* temperature rise, we define the power-to-ΔT ($P2\Delta T$) factor:

$$P2\Delta T = \frac{\Delta T_{max}}{P} \tag{8.1}$$

where ΔT_{max} is the peak steady-state increase in the tissue temperature, and P is the local power deposited in the vicinity of the implant electrode, obtained via a volume integral of the scattered SAR distribution, i.e., the local $SAR_{electrode}(\mathrm{r})$ - the $SAR_{incident}(\mathrm{r})$ without the implant. To limit the effect of numerical noise and contributions from other parts of the implants, the integral was limited to the -30 dB iso-contour relative to the peak deposition:

$$P_{\text{dep}} = \int_V \rho_t(\mathrm{SAR}_{electrode}(\mathrm{r}) - \mathrm{SAR}_{incident}(\mathrm{r}))dv \tag{8.2}$$

8.3.2 Simulations

It should be noted that ΔT_{max} might be not most relevant safety value as tissues around the tip might have temperature sensitivities, the implication of which will be discussed later.

The EM computations were performed with the finite difference time domain (FDTD) solvers of the simulation platform Sim4Life V4.0 (ZMT Zurich MedTech, Switzerland).

The increase in tissue temperature, in excess of metabolic heat generated by the body, due to the power deposited at the implant electrode can be expressed by the linear Pennes bio-heat equation (BHE) [154]:

$$\rho_t(\mathrm{r})c_t(\mathrm{r})\frac{\partial \Delta T(\mathrm{r},t)}{\partial t} = \nabla(k(\mathrm{r})\nabla\Delta T(\mathrm{r},t))+\rho_t(\mathrm{r})\mathrm{SAR}(\mathrm{r})-\rho_t(\mathrm{r})\rho_b c_b \omega(\mathrm{r})(\Delta T(\mathrm{r},t)) \tag{8.3}$$

where $\rho_t(\mathrm{r})$ is the mass density (kg/m^3), $c_t(\mathrm{r})$, the heat capacity (J/kg/K), $k(\mathrm{r})$ the thermal conductivity (W/m/K), $\omega(\mathrm{r})$ the perfusion rate (ml/min/kg) of tissue, ρ_b the mass density (kg/m^3), and c_b the heat capacity (J/kg/K) of blood. SAR(r) is the local specific absorption rate (W/kg), and $\Delta T(\mathrm{r}, t)$ is the temperature increase due to implants, in excess of body core temperature. As the resulting temperature increase should stay within the biological safe limits of less than 10 K, it can be approximated that the parameters are time- and temperature-independent.

In this study, we used the BHE solver of Sim4Life V4.0 and the analytical solution of BHE:

$$\Delta T = (\rho_t(\mathrm{r})(\mathrm{SAR}_{electrode}(\mathrm{r}) - \mathrm{SAR}_{incident}(\mathrm{r}))) * \mathrm{G}(\mathrm{r}) \tag{8.4}$$

where G(r) is the Green's function of the BHE [155, 47, 156]. As the G(r) is no longer suitable for inhomogeneous tissue distribution scenario, only the BHE solver of Sim4Life V4.0 is used for the inhomogeneous cases.

8.4 Parameter Study

The impact of different parameters on $P2\Delta T$ has been determined by varying:

- lead geometry, electrode geometry, and insulation thickness of the AIMD
- incident conditions
- tissue distributions

The geometries of the implants under test (IUT) used throughout the study are shown in Figure 8.1. The wire and insulation are concentric cylinders, and the electrodes are either cylindrical or helical. The radius of the wire and insulation are defined as a and c, respectively. The length and radius of the electrode are defined as $\mathrm{L_E}$ and t, respectively. The length of the implant lead is defined as L.

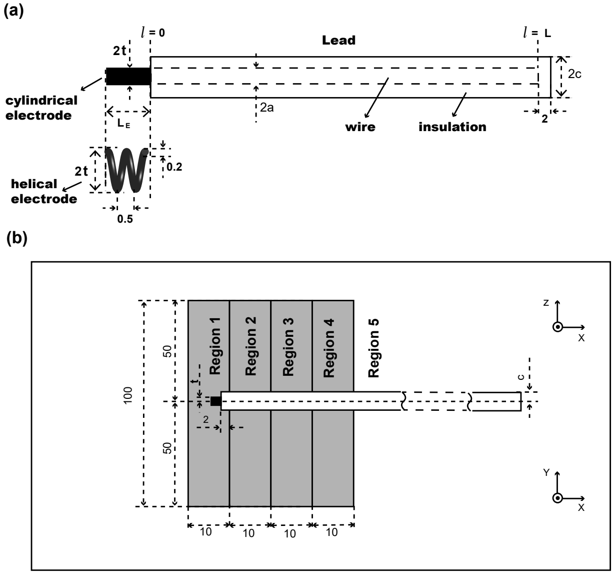
(a)
l = 0
Lead
l = L
2t
2c
cylindrical electrode
LE
2a
wire
insulation
2
2t
0.2
helical electrode
0.5
(b)
Region 1
Region 2
Region 3
Region 4
Region 5
100
50
50
t
2
c
10
10
10
10
Z
X
Y
X

Figure 8.1: (a) Geometry of the IUTs used in the study. Wire and insulation are concentric cylinders and electrodes are either cylindrical (top) or helical (bottom). (b) Tissue model of IUT-embedding media used in Section 8.4.1 and Section 8.4.2.

8.4.1 AIMD Modeling

To include different types of common-seen implant electrode and lead length, six different types of implant electrodes were chosen with lead lengths of 200 – 600 mm. First, the dependence of $P2\Delta T$ on the length (L) of the

AIMD was evaluated for L = 200 – 600 mm. Six types of IUT electrodes were considered, cylindrical electrodes with L_E= 2, 4, 6, 8, 10 mm, and a helical electrode with L_E= 2 mm; two conductive wire radii of a$\rightarrow$ 0 mm (i.e., a simple dimensionless wire) and a = 0.5 mm were considered. For all IUTs, t = 0.5 mm and c = 0.75 mm.

Next, the dependence of $P2\Delta T$ on the conductive wire topology of AIMD was investigated by simulating IUTs of wire radii a = 0 – 0.8 mm and insulation radius c = 0.75 – 4 mm, with L_E= 2 mm, t = 0.5 mm, and L = 500 mm.

Finally, the effect of incident field conditions along the conductive wire on $P2\Delta T$ was investigated by varying the incident field conditions:

$$E_{\text{tan}} = E_0 e^{j\xi l} \tag{8.5}$$

whereby E_{tan} is the E-field induced tangentially along the implant trajectory, l is the position along the IUTs, and the linear phase ξ is ramped over 0 – 30 rad/m [157]. Two lengths of IUT electrodes, L_E= 2 and 10 mm, were considered. For all IUTs, t = 0.5 mm, a = 0.5, c = 0.75, and L = 500 mm. All IUTs considered in this section are embedded in an unbounded homogeneous medium (i.e., regions 1 – 5 = high permittivity media [HPM] defined in [1]; see Figure 1), the properties of which are summarized in Table 8.1.

Table 8.1: Summary of the dielectric and thermal properties of the tissues.

Tissue	ϵ_r	σ (S/m)	k (K/W/kg)	ω (ml/kg/min)	ρ (kg/m^3)
Blood	86.4	1.2	0.52	10000	1049
Cancellous bone	20.6	0.36	0.31	30	1178
Cortical bone	16.7	0.06	0.32	10	1908
Connect tissue	53.9	0.49	0.39	37	1027
CSF	97.3	2.06	0.21	0	1007
Dura matter	73.2	0.71	0.44	380	1174
Fat	13.6	0.06	0.21	32.7	911
Fibrotic tissue	65.8	0.57	0.48	32.85	1000
Heart muscle	106.5	0.67	0.56	1026	1081
HPM	78	0.47	0.61	0	1000
Ligament	59.5	0.47	0.47	29	1142
Muscle	72.2	0.68	0.49	36.7	1090
Nevor	47.3	0.34	0.49	160	1075
Spinal cord	55	0.32	0.51	160.3	1075

8.4.2 Piecewise Varying Tissue Distribution Modeling Along AIMD

The dependence of $P2\Delta T$ on the tissue distribution surrounding the AIMD is calculated for different tissue distributions, as described in Figure 8.1 and Table 8.2. All tissue properties are summarized in Table 8.1. Four IUTs of insulation thicknesses c = 0.9, 1.2, 1.8, and 2.4 mm were considered. For all IUTs, t =0.5 mm, L_E= 2 mm, a = 0.6 mm, and L = 500 mm.

8.4.3 Electrode Embedded in Locally Spatially Inhomogeneous Tissues

In the preceding evaluation, the tissue distribution surrounding the implant electrode was treated as homogeneous. The objective was to investigate whether the power deposition and $P2\Delta T$ can be sufficiently well approximated by the tissue in contact with the electrode, as has been postulated in the past. The example structure shown in Figure 8.2 is the simplified tissue distribution in three different positions inside the epidural space of a typical spinal cord. The three evaluated positions of the generic electrode of diameter 0.5 mm and length 2 mm are also illustrated in Figure 8.2:

- position 1: the implant electrode is slightly penetrates the dural matter ($<$ 0.2 mm);
- position 2: the implant electrode is in contact with the dural matter;
- position 3: the implant electrode is completely inside epidural space (fat);

8.4.4 Validation in Detailed Anatomical Models in Clinically Relevant Scenarios

We applied the derived simplifications to two common clinical used implant types a) a generic pacemaker and b) a generic spinal-cord stimulator. Both scenarios are simulated with the anatomical model Duke V3.0 of the Virtual Population (ViP) [158] originally developed by [117] and refined [131] by the IT'IS Foundation. The model was exposed to the fields of the generic 64 MHz RF-body coil [159] and 128 MHz RF-body coil [160]. The

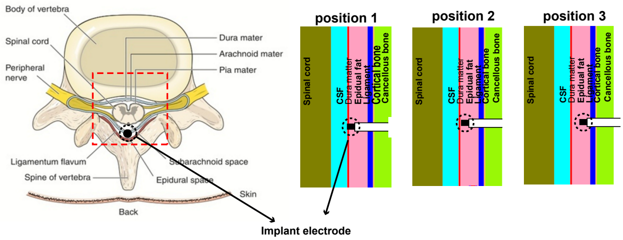
Body of vertebra
Spinal cord
Peripheral nerve
Dura mater
Arachnoid mater
Pia mater
Ligamentum flavum
Spine of vertebra
Subarachnoid space
Epidural space
Skin
Back
Implant electrode
position 1
position 2
position 3
Spinal cord
CSF
Dura matter
Epidual fat
Ligament
Cortical bone
Cancellous bone

Figure 8.2: Illustration of the anatomical model of spinal cord and selected three positions where electrode of the generic spinal cord stimulator was located.

dielectric and thermal parameters compiled in the IT'IS Foundation's tissue properties database [137] were used. The two clinical scenarios were chosen for their substantial dissimilarities in AIMD incident conditions and tissue distributions. The IUT and anatomical features in the vicinity of the IUT are shown in Figures 8.3 and 8.4 for the pacemaker and the spinal-cord stimulator, respectively. Table 8.3 lists the parameters of the two clinical scenarios.

A number of simplifications were applied to the clinical scenarios, and the $P2\Delta T$ was calculated and compared to the results without any simplifications. The simplifications shown in Figures 8.3 and 8.4 are:

- none: no simplifications were applied and the clinical scenario (RF-coil, patient, and IUT) is fully emulated in the computational domain
- IUT: the IUT is simplified as L = 300 mm, a →0 mm, with c unchanged; the remainder of the clinical components, i.e., the RF-coil and patient, are unchanged and emulated in the computational domain
- IUT plus tissue: both IUT and tissue distribution are simplified; the simplified IUT has L = 300 mm, a →0 mm, with c unchanged; the remainder of the clinical components, i.e., the RF-coil and patient, are replaced with an unbounded homogeneous medium exposed to simple excitation conditions; the simplified IUT is placed along a cardinal axis of the computational domain, and the embedding medium has the properties of the tissue in contact with the electrode

Table 8.2: Tissue assignment of the tissue model depicted in Figure 8.1, for different tissue distribution used in Section 8.4.2.

Tissue Distribution	Region 1	Region 2	Region 3	Region 4	Region 5
Muscle	Muscle	Muscle	Muscle	Muscle	Muscle
CSF	CSF	CSF	CSF	CSF	CSF
Fat	Fat	Fat	Fat	Fat	Fat
Heart Muscle	Heart muscle	Heart muscle	Heart muscle	Heart muscle	Heart muscle
Fat-dominated	Muscle	Fat	Blood	CSF	Heart muscle
Muscle-dominated	Fat	Muscle	Blood	CSF	Heart muscle

Table 8.3: Summary of parameters, associated with the IUT, tissue distribution, and RF-exposure, of the two clinical scenarios.

Tissue	Pacemaker	Spinal-cord stimulator
IUT: (t, L_E, L, a, c (mm)	0.5, 2, 400, 0.6, 1.2	0.5, 2, 500, 0.5, 0.9
Tissue distribution	heart muscle, muscle, blood	fat, bone, CSF, ligament
RF-coil extent	Vertebra C5 to Vertebra L5	Vertebra L2 to middle thigh

8.5 Results

8.5.1 AIMD Modeling

Figure 8.5 (a) and (b) show that the conductive wire topology has very little effect on $P2\Delta T$. Figure 8.5 (a) shows the $P2\Delta T$ as a function of IUT conductive wire lengths for six types of electrodes. The results indicate that the length of the IUT conductive wire has little influence on $P2\Delta T$; the dependence of $P2\Delta T$ on wire length increases with increasing L_E and shows asymptotic behavior towards larger L for both wire topologies, $a \to 0$ mm and a = 0.5 mm. The effect of IUT lengths $L \geq 0.5\lambda$ on $P2\Delta T$ are $<7\%$. As expected, $P2\Delta T$ are greatly affected by the shape of implant electrode, as the SAR distribution can be seen as the result of a quasi-static field, which is strongly affected by electrode shape features such as sharpness (leads to field concentration) and extent (lead to field distribution). In the example studied, $P2\Delta T$ is more than 22% higher in the helical wire electrode compared to the same length of straight wire, and 55% lower in the long straight wire electrode (L_E= 10 mm) compared to the short straight wire electrode (L_E= 2 mm).

Figure 8.5 (b) shows that the influence of the wire diameter is small for any other IUTs as well ($c = 0.75 \rightarrow 4$ mm, the radius of the conductor varying from dimensionless to 0.8 mm); the difference is $<5\%$.

Figure 8.5 (c) shows the $P2\Delta T$ determined for two IUTs with L_E= 2 and 10 mm exposed to a set of linear-phase E_{tan} conditions with phase gradient ξ ranging from $0 \rightarrow 30$ rad/m. The variability of $P2\Delta T$ is 6% for the short (L_E= 2 mm) and 13% for the long (L_E= 10 mm) electrodes.

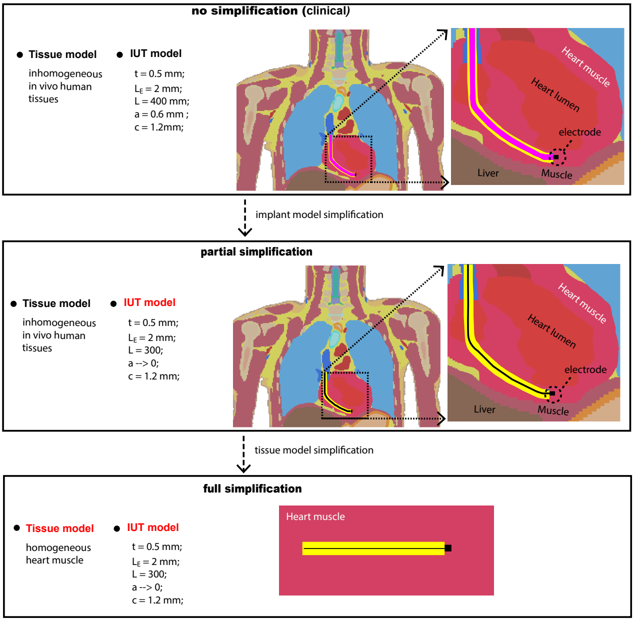
no simplification (clinical)
● Tissue model
inhomogeneous in vivo human tissues
● IUT model
t = 0.5 mm;
L_E = 2 mm;
L = 400 mm;
a = 0.6 mm ;
c = 1.2mm;
Heart muscle
Heart lumen
electrode
Liver
Muscle
implant model simplification
partial simplification
● Tissue model
inhomogeneous in vivo human tissues
● IUT model
t = 0.5 mm;
L_E = 2 mm;
L = 300;
a --> 0;
c = 1.2 mm;
Heart muscle
Heart lumen
electrode
Liver
Muscle
tissue model simplification
full simplification
● Tissue model
homogeneous heart muscle
● IUT model
t = 0.5 mm;
L_E = 2 mm;
L = 300;
a --> 0;
c = 1.2 mm;
Heart muscle

Figure 8.3: Application of proposed simplifications to the clinical scenario of a patient with a generic pacemaker. The different simplification stages where $P2\Delta T$ is calculated are illustrated. Top: no simplification (clinical), Middle: partial simplification, and Bottom: full simplification. Note: the RF-coil is not depicted.

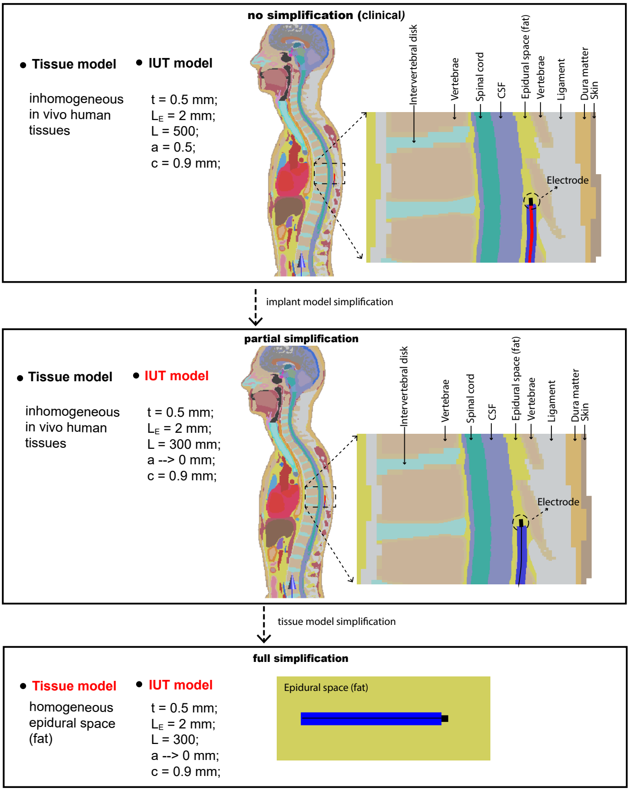
no simplification (clinical)
• Tissue model
• IUT model
inhomogeneous in vivo human tissues
t = 0.5 mm;
L_E = 2 mm;
L = 500;
a = 0.5;
c = 0.9 mm;
Intervertebral disk
Vertebrae
Spinal cord
CSF
Epidural space (fat)
Vertebrae
Ligament
Dura matter
Skin
Electrode
implant model simplification
partial simplification
• Tissue model
• IUT model
inhomogeneous in vivo human tissues
t = 0.5 mm;
L_E = 2 mm;
L = 300 mm;
a --> 0 mm;
c = 0.9 mm;
Intervertebral disk
Vertebrae
Spinal cord
CSF
Epidural space (fat)
Vertebrae
Ligament
Dura matter
Skin
Electrode
tissue model simplification
full simplification
• Tissue model
• IUT model
homogeneous epidural space (fat)
t = 0.5 mm;
L_E = 2 mm;
L = 300;
a --> 0 mm;
c = 0.9 mm;
Epidural space (fat)

Figure 8.4: Application of proposed simplifications to the clinical scenario of a patient with a generic spinal cord stimulator. The different simplification stages where $P2\Delta T$ is calculated are illustrated. Top: no simplification (clinical), Middle: partial simplification, and Bottom: full simplification. Note: the RF-coil is not depicted.

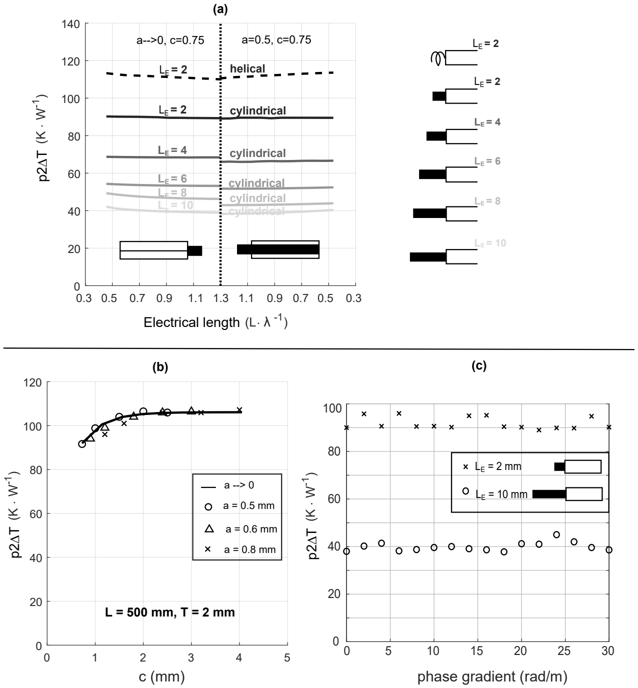

Figure 8.5: (a) $P2\Delta T$ for different electrodes as a function of IUT electrical length (L·λ^{-1}). (b) $P2\Delta T$ as a function of IUT insulation radius, c, evaluated for IUTs with different wire radii, a. (c) $P2\Delta T$ as a function of incident conditions, evaluated for IUTs exposed to linear-phase tangential E-field of different phase gradient (0 - 30 rad/m).

8.5.2 Tissue Distribution Simplification

Figure 8.6 summarizes the heating factors of four different IUTs (c = 0.8, 1.2, 1.8, or 2.4 mm) within different tissue distributions. Six tissue distributions (see Figure 1 and Table 2) are considered for each IUT. For all IUTs considered, the heating factors obtained for homogeneous muscle or fat tissue distributions closely approximate (¡10% deviation) those obtained for muscle-dominated or fat-dominated tissue distributions, respectively, demonstrating that, in such cases, homogeneous simulations can solved more efficiently with, e.g., methods that resemble fast-Poisson solvers. $P2\Delta T$ in fat tissue is more than double that in muscle tissue, due to the much lower thermal conductivity of tissue fat, which reduces diffusion cooling. Both FDTD (FDTD-BHE) and a method whereby the steady-state spherical Green's function of the BHE (G-BHE) [47] is employed were used to solve the BHE. Figure 8.6 shows that the $P2\Delta T$ values obtained with both the FDTD-BHE and G-BHE are in very good agreement for homogeneous tissue distribution scenarios.

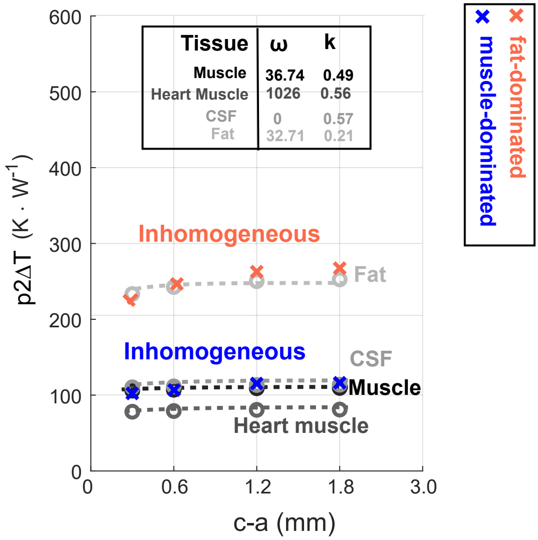

Figure 8.6: $P2\Delta T$ for implants with various insulation thicknesses (c) embedded in different tissue distributions. The BHE is solved both numerically (FDTD-BHE) and with analytical Green's function (G-BHE). The heating factors calculated with FDTD-BHE are indicated by 'o' and 'x' markers. The heating factors calculated with G-BHE are indicated by dash lines.

8.5.3 Electrode Embedded in Locally Spatially Inhomogeneous Tissues

Figure 8.7 shows the E-field and SAR distributions of implant electrodes placed at positions 1, 2, and 3. Even though the surrounding tissue environment of the implant electrode changes only slightly, the E-field and SAR distributions are very different due to the differences in tissue distribution near the electrode. Consequently, the $P2\Delta T$ also varies significantly, i.e., by a factor of more than 2.

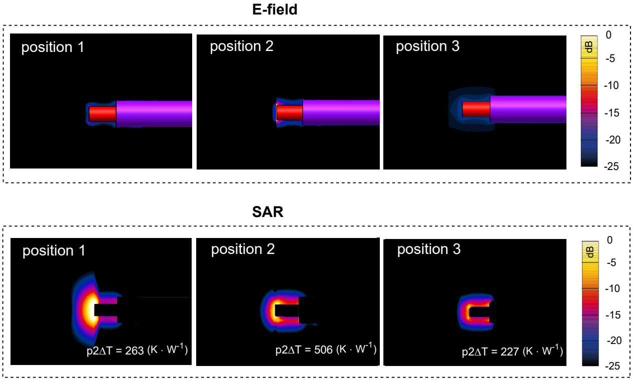

Figure 8.7: The E-field and SAR distributions corresponding to the three positions defined in Figure 2

8.5.4 Validation in Anatomical Models

$P2\Delta T$ and the computational resources required for its derivation for each level of simplification are summarized in Tables 8.4 and 8.5 for the pacemaker and spinal-cord stimulator IUTs, respectively. Despite the different topologies of the implant leads, the incident conditions, and the tissue distributions of the two scenarios, the proposed simplification works well for both. The deviation between $P2\Delta T$ derived with no simplification (clinical) and full simplification is within 6%, while the computational resources required were smaller by more than a factor of 10 (600 Mcell to less than 50 Mcell; this reduction directly translates into a reduction in memory requirement; computation time savings can even exceed this reduction, as a coarser mesh results in a longer stable time-step according to the Courant-Friedrichs-Lewy (CFL) criterion [161], thus with fewer time-steps required).

8.6 Discussion and Conclusions

The results of this parameter study confirm that the lead modeling and the electrode can be largely decoupled, i.e., after the total power deposition is determined, e.g., according to ISO/TS 10974; only a simplified implant with a detailed electrode and electrode-tissue environment must be modeled to determine the $P2\Delta T$, while the impact of the simplified implant lead on $P2\Delta T$ can be assessed with additional uncertainties. For the determination of the magnitude of the deposited power P, an accurate implant model is required, e.g., a transfer function model [1]. The following conclusions can be drawn from this study, provided that the leads are electrically long L $\geq \lambda/2$ and the electrodes short $\leq \lambda/40$:

- The $P2\Delta T$ is predominantly dependent on (1) the geometry (size, sharpness, etc.) of the AIMD electrode and (2) the type of tissue in contact with the electrode, and (3) the inhomogeneity of the tissue in the near vicinity of the electrode.
- The influence on $P2\Delta T$ of (1) details of the lead wire structure, (2) the tissues in which the lead is embedded, and (3) the distribution of the incident fields is small, does not require detail modeling and can be integrated with an uncertainty term.

The simplification of the AIMD and tissue modeling has been successfully validated with two clinical scenarios based on vastly different tissue distributions and induced field conditions.

The results also suggest that the very local tissue distribution, which in general, is not homogeneous, must be analyzed in great detail. For example, non-perfused scar tissue tends to form at the surface of the AIMD electrodes; this scar tissue is generally not temperature sensitive and is much less lossy than surrounding tissues. Also, part of the electrode might be embedded in muscle, whereas the rest could be in contact with the blood, etc.

The thermal properties of the tissue used in this work are averaged values from multiple measurements. The actual properties vary from individual to individual. The effects on $P2\Delta T$ can be determined by a sensitivity analysis or represented by an uncertainty term, with application of the same decoupling simplifications as used in this study. Besides, given the anatomical variation in, e.g., body mass index, across different population, the tissue distribution near the implant electrode maybe different. Therefore, it is necessary to perform the thermal simulations with varying local tissue models that represent a wide population range.

It should also be noted that the $P2\Delta T$ at each electrode cannot be evaluated separately if the power deposition spatially overlaps as for example in case of very narrowly spaced neurostimulation electrodes. In these cases, evaluation of a combined multi-electrode model is advised. In the case of bipolar pacemaker, for example, the separation between ring and tip is sufficiently separated allowing separate $P2\Delta T$ evaluations.

Finally, the limitations of current study must be noted. This study is limited to leads in which the structure close to the electrodes is continuous, i.e., without lumped elements close to the electrodes. Furthermore, investigations are needed to determine the uncertainty limits for electrically longer electrodes such as shock coils in defibrillators.

In summary, we have defined the requirements for modeling $P2\Delta T$ of AIMDs in MRI that —together with, e.g., an ISO/TS 10974-based assessment of the total power deposition — enables comprehensive analysis of the maximum in vivo temperature increases with known confidence intervals and with a limited number of simulations. Importantly, this approach also has the potential to replace animal experiments.

Table 8.4: Summary of $P2\Delta T$ and computational resource required for a generic pacemaker for the different simplifications

Parameters	No Simplification (clinical)	Partial Simplification	Full Simplification (FDTD-EM/-BHE)	Full Simplification (FDTD-EM/G-BHE)	Maximum Variation Time Savings
$P2\Delta T$ (K/W), 64 MHz	81	80	81	82	2%
$P2\Delta T$ (K/W), 128 MHz	81	85	81	82	5%
			SAR(r) (W/m^3) computation		
Computation domain (Mcells)	650	540	30	30	22x
Compute time (hrs)	5	4	0.5	0.5	10x
			ΔT (K) computation		
Computation domain (Mcells)	230	140	30	-	7x
Compute time (hrs)	4	2	0.5	<0.1	8x

Table 8.5: Summary of $P2\Delta T$ and computational resource required for a generic spinal-cord stimulator for the different simplifications

Parameters	No Simplification (clinical)	Partial Simplification	Full Simplification (FDTD-EM/-BHE)	Full Simplification (FDTD-EM/G-BHE)	Maximum Variation Time Savings
$P2\Delta T$ (K/W), 64 MHz	250	240	236	235	-6%
$P2\Delta T$ (K/W), 128 MHz	255	251	253	249	2%
			SAR(r) (W/m^3) computation		
Computation domain (Mcells)	630	350	30	30	21x
Compute time (hrs)	7	3.5	0.5	0.5	14x
			ΔT (K) computation		
Computation domain (Mcells)	210	150	30	-	7x
Compute time (hrs)	5	3	0.5	< 0.1	10x

Part VI

Epilogue

Chapter 9

Conclusions and Outlook on Related Future Research Topics

In this thesis, I have addressed major unresolved scientific and engineering problems in the evaluations of AIMD risk according to Tier 3 of the ISO/TS 10974[1], thereby improving and simplifying the assessment process and substantially reducing the associated uncertainties.

First, novel *in vitro* experimental methods suitable for both 1.5 Tesla and 3.0 Tesla MRI instruments were developed for the characterization of the AIMD RF-heating model. As the accuracy of the AIMD RF-heating model is verified by means of *in vitro* experimental methods, we summarized the theoretical accuracy of Tier 3 method and illustrated the practical considerations for accommodation of the non-ideality of the experimental conditions needed in the Tier 3 assessment of RF-induced heating defined in ISO/TS 10974. The small – mm-scale – distal electrodes of an AIMD can cause localized RF-induced power deposition with very high spatial gradients (5 – 6 dB/mm), which is the main contributor to inaccuracies of near-field measurement. To improve the accuracy of the traditional experimental evaluation, which relies solely on hardware instrumentation, a data-drive experimental method based on an image co-registration algorithm has been developed to reduce the large uncertainty associated with the steep spatial gradient. The method has been successfully validated with respect to a variety of implants, exposure levels, and data acquisition procedures. An uncertainty level of less than 1 dB has been achieved with this method, which is significantly lower than the uncertainty achieved with the traditional evaluation method. To demonstrate the RF safety of an AIMD during MRI exposure, a numerical model of RF-heating of the AIMD is needed. The validation of the model requires a sufficient set of incident tangential electrical field conditions that spans the *in vivo* range of exposure, which was very time consuming and often resulted in poorly defined incident conditions. Based on the finding that the amplitude and phase of the incident tangential electrical field along a single lead path in a cylindrical phantom can be sufficiently varied by changing the polarization of the incident magnetic field inside standard birdcage RF coils, a novel test field diversity (TFD) method has been developed to provide well defined diverse exposure conditions. The new TFD method enables improved and reliable validation of the AIMD model with low uncertainty and it is applicable for evaluation of both 1.5 Tesla and 3.0 Tesla MRI environment.

Next, the gap of knowledge concerning a comprehensive evaluation of *in vivo* RF-human interaction was addressed. The anatomical human phantoms of the Virtual Population (ViP) have been used in many dosimetry studies. However, uncertainty related to the anatomical phantom in RF research has largely been neglected. To bridge this gap, we quantified and established the uncertainty associated with segmentation and tissue assignment by comparing the results obtained from a multi-tier safety assessment of MRI RF-induced AIMD heating, according to Clause 8 of ISO/TS 10974, performed with the ViP 1.x and ViP 3.0 generations of the anatomical phantom models. The results show that the additional uncertainty associated with the tissue assignment and segmentation quality anatomical phantom in evaluations of AIMD heating is 0.6 dB. Assessment of multiple phantoms that cover a targeted population based on different volunteers is required for quantitative analysis of dosimetric endpoints that depend on patient anatomy. The RF-induced heating for patients with implants during MRI exposure is a complex function of multiple factors, e.g., the characteristics of the implant, patient anatomy, imaging positions, RF coil, etc., thus, comprehensive safety assessment cannot be based on a limited number of scenarios. To be able to perform comprehensive evaluations in a timely and traceable manner, we established an *in silico* safety assessment trial that combines a data library with a data analytics toolset. The proposed standardized framework provides not only relevant but also comprehensive, consistent, extendable, and traceable results that facilitate establishment of a corroborated knowledge base built on existing and emerging results. The framework also facilitates exploratory data analysis to be used to identify both maximized imaging quality and patient safety. To provide a fuller picture and better understanding of the implant *in vivo* exposure environment, we investigated the influence of patient anatomical features, imaging positions, and exposure conditions. We also elucidated and summarized the currently accepted mechanisms governing the MRI safety of patients with and without implants.

Finally, safety evaluation of AIMDs during MRI requires assessment of the potential for RF-induced *in vivo* temperature increase in exposed patients. Due to the complicated *in vivo* tissue distributions inside the human body and the multi-scale structures involved in clinical scenarios – on the scale of meters for the human body and millimeters for the AIMD structures), the estimation of *in vivo* temperature increase can be extremely time consuming and computationally expensive. To lessen this burden, we investigated the modeling requirements for efficient and reliable determination of the conversion of local RF power deposition of the AIMD to the *in vivo* maximum local tissue temperature increase ($P2\Delta T$). The results confirm that significantly simplified models of leads and standard incident field conditions, e.g., uniform exposures, can be used to assess $P2\Delta T$ while both the lead electrode and the surrounding tissues need to be modeled in detail. The use of the proposed simplifications for assessment of $P2\Delta T$ can reduce the effort by a factor of more than 10 times.

In summary, the work performed in this thesis contributes to the improvement of MRI safety assessment of medical implants by providing novel methods and models with well-controlled uncertainty to use when performing safety assessments under various scenarios. It also provides essential information to help bridge some of the identified knowledge gaps in the current guidelines on MRI-implant safety.

9.1 Outlook

Many patients with AIMD are excluded from MRI-based diagnosis because the risks associated with RF-exposure are overestimated on the basis of the current safety guidelines. The results obtained from the research performed in this thesis can help improve risk assessment for these patients, providing access to potentially life-saving diagnostic procedures. However, additional improvements beyond the current standardization work are needed to further reduce overestimation of the hazards and to facilitate more precise hazard prediction to make MRI-based diagnostics accessible to more patients. The challenges include:

- *The multi-tissue environment:* The AIMD is generally embedded in a spatially complex distribution of tissues of varying dielectric properties. In other words, the effective wavelength and tissue attenuation changes along the lead. Cochlear implants are a prominent example: these are partially exposed at the interfaces of the skull, skin, and air, inside the bone and in the cochlear fluid. In safety assessments, the complex tissue composition is simulated with one or more types of homogeneous media, and maximum hazard levels are considered. This can lead to several-fold overestimation of risk, as demonstrated in Tier 4 evaluations of cochlea implants. A standardized procedure for multi-tissue environments will improve the hazard evaluations, reducing the overestimation.

- *Partially-implanted and on-body devices:* Until now, all safety assessment activities have been focused on AIMDs that are fully-implanted inside the human body, where the main contribution to the *in vivo* exposure environment is the B_1 induced E-field, which is relatively well defined regardless of the actual birdcage design. For partially-implanted medical devices – e.g., interventional MRI catheters – and on-body devices – e.g., ECG leads – the exposure environment of the devices outside the human body is much more complicated and unpredictable, as it is heavily dependent on the birdcage geometry, e.g., the location of the lumped elements and feeds, and lead routings outside the body. In addition, the E-field outside body can be very large, the implant parts outside the body can pick up this energy and deposit it inside body. It is clear that methodologies developed for fully-implanted devices are not directly applicable to partially implanted or body-worn devices. The most common way to evaluate heating of partially-implanted devices is through direct measurement of the temperature [162, 163]. More generally and easy-to-apply procedures are needed for the hazard assessment of partially implanted medical devices.

- *High-field MRI with multi-channel parallel transmission coils:* The methods and instrumentation discussed in this work are primarily designed and intended for low-field MRI ($\leq$ 3 Tesla) with two-channel RF coils. In these cases, because of the similarity to the wavelength of the human body and the simplicity of the RF coil structure, the field distribution is relatively simple, and the hotspots can be potentially controlled by limiting the whole-body SAR. While for high-field MRI ($\geq$ 3 Tesla), multi-channel parallel transmission coils are used to help achieve homogeneous fields near the field-of-view (FOV) during the MRI scan. The decreased RF field wavelength, together with the complex RF coil structure, yields a much more complicated field distribution. Methodologies and procedures developed for low-field MRI estimation cannot be directly used for high-field cases. Until now, most of the assessment work related to high-field MRI are through direct point measurements of the field or temperature inside the MRI scanner [76, 126]. Procedures and methods that can be used for comprehensive assessment of high-field MRI need to be established in the future.

Part VII

Appendix

Appendix A

Supporting Information of Chapter 4

A.1 Overview

The evaluation of the uncertainty of experiments is based on splitting the total uncertainty into various uncertainty sources which are independent or have limited interdependencies. The contributions of these uncertainties were determined by assuming statistical models. The total uncertainty was expressed as the root-sum-square (RSS) value of all contributions. The basic concepts for determining the uncertainties and selecting appropriate statistical models for applications in the field of electromagnetic compatibility were developed, e.g., by Taylor and Kuyatt[164].

A.2 TFD expsure

The RF-exposure provided by the TFD in Chapter 4 is determined from its experimental and numerical components. An uncertainty budget is established from sensitivity analysis of AIMD heating due to each source of uncertainty.

A.2.1 Experimental Setup

TFD experimental setup consists of RF-coil, phantom, TSM, and RF-fields (E and H) data acquisition system. The contributions associated with TSM and RF-fields data acquisition system are accounted for in the local enhancement evaluation. The uncertainty budget of the experimental setup is established from the following components:

- RF-coil exposure drift: The uncertainty associated with the drift of the exposure systems (MITS1.5 and MITS3.0, Zurich Med Tech, Switzerland) was evaluated during an exposure period of 2 hours.

- Phantom: Uncertainty components associated with shape, position within the RF-coil, AIMD holder presence, reflection from truncated boundaries, and scattering between parallel AIMD lead segments were numerically assessed.

A.2.2 Numerical Modeling

The exposure setup is emulated and the incident fields (E and H fields) within the TFD phantom are calculated with a validated full-wave computational electromagnetics software, Sim4Life (Zurich Med Tech, Switzerland). The B_1 -polarization and $E_{\text{tan}}(l_1)$, recorded during each TFD exposure is re-constructed with the numerical model of the exposure setup. The uncertainty budget of the numerical model is established from the following components:

- Numerical errors: Uncertainty components associated with grid resolution and absorbing boundary condition used in computational domain truncation were assessed. 1) Each RF-coil model is discretized at several grid resolutions and $E_{\text{tan}}(l_1)$ is calculated at each grid resolution. 2) The absorbing boundary condition used in computational domain truncation, assessed according to Chapter 7 of[50]. The deviation of $E_{\text{tan}}(l_1)$ is negligible.

- RF-coil modeling: Uncertainty components associated with loading condition and geometrical simplification of the RF-coil were assessed. The RF-coil model is tuned to resonate at the nominal operating frequency (64 MHz: 1.5 T and 128 MHz: 3.0 T) using different loads (no load to 80-kg load). And different simplifications of geometrical structure of the experimental RF-coil were applied. The deviation of $E_{\text{tan}}(l_1)$ at the operating frequency is considered.

A.3 Local Enhancement Evaluation

During each TFD exposure, local enhancement of the IUT is experimentally evaluated in homogeneous TSM (HPM, ϵ_r = 78, σ = 0.47 S/m) with RF-fields acquisition system. The uncertainty budget of the local enhancement evaluation is established from the following components: 1) data acquisition system; 2) TSM; 3) post-processing.

A.3.1 Data acquisition system

- Dosimetric sensor: Uncertainty components associated with hemispherical isotropy, linearity, and integration volume, are obtained from manufacturer's specification (EX3DV4, SPEAG, Switzerland).

- Data acquisition electronics: Uncertainty components associated with detection limit, read-out electronics, and integration time, are obtained from manufacturer's specification (DAE4, SPEAG, Switzerland).

- TSM: Dielectric properties of TSM, nominally assumed to be ϵ_r = 78, σ = 0.47 S/m. Deviation of $\pm$ 10% and $\pm$ 5% in ϵ_r and σ is considered.

A.3.2 Post-processing

Uncertainty based on method proposed in Chapter 5 is used.

A.4 Tier 3 model

Tier 3 RF-heating model of the IUT was derived using the piecewise excitation method [83]. The uncertainty budget is obtained from manufacturer's specification (piX System, Zurich Med Tech, Switzerland).

Appendix B

Supporting Information of Chapter 5

B.1 Overview

The evaluation of the uncertainty of experiments is based on splitting the total uncertainty into various uncertainty sources which are independent or have limited interdependencies. The contributions of these uncertainties were determined by assuming statistical models. The total uncertainty was expressed as the root-sum-square (RSS) value of all contributions. The basic concepts for determining the uncertainties and selecting appropriate statistical models for applications in the field of electromagnetic compatibility were developed, e.g., by Taylor and Kuyatt[164]. The ISO/TS 10974[1] adapts these methods and specifies the relevant uncertainty parameters to be evaluated for the experimental and numerical testing of the MR safety of medical implants.

B.2 Uncertainty Components of Table 5.1

Table 5.1 summarizes the uncertainty budget of the the traditional method and the proposed method. The combined uncertainty is established from the following components associated with the derivation of the model.

B.2.1 Exposure Drift

The relative change of the exposure over the period of the measurement, determined by magnitude of the magnetic fields produced by the generic RF coil.

B.2.2 Phantom

The effect of 1) phantom shape and position within the RF-coil and 2) the AIMD holder, to the incident fields (AIMD exposure). 1) was assessed from numerical simulations of the phantom, considering the tolerance in phantom position within the RF-coil of ± 5 mm in all directions. The tolerance in the phantom shape is assumed to be negligible. 2) was assessed experimentally from the magnitude of the incident electric field with and without the AIMD holder present.

B.2.3 TSM

The tolerance of the permittivity and conductivity of the tissue-simulating liquid (HPM, ϵ_r = 78, σ = 0.47) of ± 10% and ± 5%, respectively, were considered. The maximum deviation of AIMD exposure was used.

B.2.4 Data Acquisition

The uncertainty of the data acquisition is determined by 1) the uncertainty associated with isotropy and linearity of the probe; 2) the uncertainty associated with detection limits, integration time, and the readout electronics of the data acquisition unit. The uncertainty provided by the probe and data acquisition unit manufacture's specification were used.

B.2.5 Truncated Boundary

The reflection from the phantom wall due to scattering of the AIMD. This is estimated from numerical simulation of an 800 mm-long insulated AIMD, with one capped (isolated) end placed inside an HPM-air half space. The AIMD is placed in HPM, 6 cm away from HPM-air interface. The deviation on the power deposition was found to be 0.5 dB, compared to infinite space of homogeneous HPM.

B.2.6 Field Sensor Position

The tolerances of sensor position x, y and z directions are assumed to be ±0.25mm, based on the positioning accuracy of the robotic system. For the proposed method, this uncertainty component is eliminated through the use of co-registration procedure, defined in Section 5.4.3.

B.2.7 SAR_{HR}

The uncertainty caused by SAR_{HR} calculated from computational electromagnetic simulations includes: 1) contribution from grid resolution of the numerical simulations, which was assessed from the deviation of the power deposition calculated from a coarser, a finer, and the operating grid resolutions;

2) contribution from numerical reflection due to grid truncation by an absorbing boundaries;

3) contribution from HPM properties, assessed numerically by assuming tolerance of the relative permittivity and electrical conductivity of HPM to be ϵ_r = 78 ±10% and σ = 0.47 ± 5% S/m, respectively.

4) contribution from AIMD insulation properties and lead structure, which was assessed numerically, assuming tolerances of the ϵ_r and σ of the AIMD insulation of 2-4 and 0 - 0.003 S/m, respectively. And conductors of different lengths (300 mm - 600 mm) were considered. The uncertainty component is taken to be the maximum deviation of the resulting power depositions;

5) contribution from AIMD holder, assessed from the deviation of the power deposition of a test device with and without the presence of the AIMD holder via numerical simulations.

B.2.8 Power Calculation

The power deposition at the vicinity of the electrode is assessed from a volume integral about the peak spatial value of the SAR distribution. The enclosing volume is defined from the contour of iso-absorption that is determined to be sufficiently large to account for the power deposited by the electrode, meanwhile excluding the contribution from the wired conductor. The variation of the volume integrals for the enclosing volume defined by -30 dB ± 5 dB contour from the peak spatial SAR value is assessed.

B.2.9 Co-registration

The uncertainty associated with co-registration procedure is determined by the resolution of SAR_{HR} used. In this work, 0.1 mm x 0.1 mm x 0.1 mm resolution of SAR_{HR} R is assumed.

Besides, the uncertainty of Tier 4 full-wave reference simulation is not included in the table, as it is only used as a reference to validate the results in this work, it is not part of the evaluation procedure. The uncertainty associated with the Tier 4 full-wave simulations used to derive reference values includes components similar to components 1) to 4) of SAR_{HR} calculation. Therefore, the values from those assessed for SAR_{HR} were used, and the total uncertainty is 0.3 dB.

Appendix C

List of Acronyms

AIMD	Active Implantable Medical Devices
BHE	Bio-heat equation
BMI	Body Mass Index
CEM	Computational Electromagnetic
CT	Computer Tomography
DASY	Dosimetric Assessment System
DBS	Deep Brain Stimulator
DUT	Device Under Test
EM	Electromagnetic
E-field	Electrical field
FDTD	Finite-Difference Time-Domain
FDA	U.S Food and Drug Administration
H-field	Magnetic field
HPM	High Permittivity Medium
hSAR	Head Averaged SAR
ICNIRP	International Commission on Non-Ionizing Radiation Protection
IEEE	Institute of Electrical and Electronics Engineerings
IT'IS	Foundation for Information Technologies in Society
ISO/TS	International Standard Organization/Technical Specification
IUT	Implant Under Test
MITS	Medical Implant Test System
MR	Magnetic Resonance

MRI	Magnetic Resonance Imaging
PM	Pacemaker
psSAR	peak spatial Specific Absorption Rate
psSAR10g	peak spatial Specific Absorption Rate averaged over 10 g
RF	Radiofrequency
RMS	Root Mean Square
SAR	Specific Absorption Rate
SAT	Subcutaneous Adipose Tissue
SCS	Spinal Cord Stimulator
SEMCAD	Simulation Platform for Electromagnetic Compatibility Antenna Design and Dosimetry
SPEAG	Schmid & Partner Engineering
TDS	Time domain Sensor
TE	Transverse Electric
TEM	Transverse Electric and Magnetic
TFD	Test Field Diversity
TSM	Test Simulating Medium
ViP	Virtual Population
wbSAR	Whole-Body Average SAR
ZMT	Zurichmed Tech AG

Appendix D

List of Symbols

Symbol	Quantity	Unit
B	Magnetic flux density	T
E	Electric field	V/m
H	Magnetic field	A/m
P_{dep}	Power deposition near implant electrode	W
f	Frequency	Hz
ΔT	Temperature increase	K
ϵ_r	Relative permittivity	
σ	Conductivity	S/m
c_t	Tissue specific heat capacity	J/kg/K
c_b	Blood specific heat capacity	J/kg/K
k	Thermal conductivity	W/m/K
ω	Perfusion rate	ml/min/kg
E_{tan}	Tangential electric field	V/m
ρ	Mass density	kg/m^3
χ	Power deposition enhancement factor	

Appendix E

List of Publications

E.1 Journal Publications

Within the framework of this thesis, the following scientific publications have been written by the author.

(1) Yao A, Zastrow E, and Kuster N. Data-driven experimental evaluation method for the safety assessment of implants with respect to RF-induced heating during MRI. *Radio Science*, 53(6):700–709, 2018.

(2) Yao A, Zastrow E, Cabot E, Lloyd B, Schneider B, Kainz W, and Kuster N. Anatomical model uncertainty for RF safety evaluation of AIMD under MRI exposure. *Bioelctromagnetics (published online ahead of print)*, 2019.

(3) Yao A, Zastrow E, Neufeld E, and Kuster N. Efficient and reliable assessment of the maximum local tissue temperature increase at the electrodes of medical implants under MRI exposure. *Bioelctromagnetics*, 40(6):422–433, 2019.

(4) Yao A, Zastrow E, Neufeld E, Cabanes-Sempere M, and Kuster N. Novel test field diversity method for RF transfer function validation required for demonstrating MRI safety of active implantable medical devices. submitted to *Magnetic Resonance in Medicine*, 2019.

(5) Murbach M, Yao A, Zastrow E, Kainz W, and Kuster N. Electromagnetic MRI Safety with and without Implantable Metallic Devices: A Review. submitted to *Journal of Magnetic Resonance in Imaging*, 2019.

E.2 Other Publications

The author has presented or co-authored various other publications.

(1) Yao A, Zastrow E, and Kuster N. Standardized, validated and effective safety assessment of patients with medical implants under MRI exposure using a comprehensive data library combined with an analytics toolset. *In Proceedings of* 27^{th} *International Society for Magnetic Resonance in Medicine (ISMRM) Annual Meeting*, 2019.

(2) Yao A, Zastrow E, and Kuster N. A robust experimental evaluatioin method for RF safety assessment of implants during 1.5 T and 3.0 T MRI. *In Proceedings of* 26^{th} *International Society for Magnetic Resonance in Medicine (ISMRM) Annual Meeting*, Paris, France, April 22-27, 2018.

(3) Yao A, Zastrow E, and Kuster N. Power to temperature conversion of AIMD under RF exposure. *In Proceedings of* 26^{th} *International Society for Magnetic Resonance in Medicine (ISMRM) Annual Meeting*, Paris, France, April 22-27, 2018.

(4) Yao A, Zastrow E, and Kuster N. Integration of bid-data analytics in safety assessment of patients with medical implants during MRI exposure. *In Proceedings of the Joint Meeting of the Bioelectromagnetics Society (BEMS) and the European BioElectromagnetics Association (EBEA)*, Piran, Slovenia, June 14-19, 2018.

(5) Yao A, Zastrow E, and Kuster N. Robust experimental evaluation method for the safety assessment of implants due to RF-induced heating during MRI. *IIn Proceedings of the* 32^{th} *URSI General Assembly and Scientific Symposium*, Montreal, Candada, August 16-26, 2017.

(6) Yao A, Zastrow E, and Kuster N. Test field diversification method for the safety assessment of RF-induced heating of AIMDs during 1 . 5-T MRI. *In Proceedings of* 25^{th} *International Society for Magnetic*

Resonance in Medicine (ISMRM) Annual Meeting, Honolulu, USA, April 22-27, 2017.

(7) Yao A, Zastrow E, and Kuster N. Power to temperature conversion factor derivation for AIMD under MRI. *IIn Proceedings of the* 32^{th} *URSI General Assembly and Scientific Symposium*, Montreal, Candada, August 16-26, 2017.

(8) Yao A, Zastrow E, and Kuster N. Test medium derivation for the safety assessment of RF-induced heating of leaded cardio implants during 1.5-T MRI. *In Proceedings of* 25^{th} *International Society for Magnetic Resonance in Medicine (ISMRM) Annual Meeting*, Honolulu, USA, April 22-27, 2017.

(9) Yao A, Zastrow E, and Kuster N. Investigation of test media for the modeling of RF-induced heating of implant: cardio applications during 1.5 T MRI. *In Proceedings of the Joint Meeting of the Bioelectromagnetics Society (BEMS) and the European BioElectromagnetics Association (EBEA)*, Hangzhou, China, June 3-9, 2017.

(10) Yao A, Zastrow E, and Kuster N. Computable anatomical phantoms for MRI safety evaluation of patients with implants. *In Proceedings of the Joint Meeting of the Bioelectromagnetics Society (BEMS) and the European BioElectromagnetics Association (EBEA)*, Ghent, Belgium, June 5-10, 2016.

(11) Yao A, Zastrow E, Cabot E, Payne D, and Kuster N. Evaluation of MRI exposure in patients using the virtual poulation 3.0 and 1.0 anatomical phantoms. *In Proceedings of the Joint Meeting of the Bioelectromagnetics Society (BEMS) and the European BioElectromagnetics Association (EBEA)*, Monterey, USA, June 14-19, 2015.

(12) Yao A, Zastrow E, Cabot E, Payne D, and Kuster N. Evaluation of MRI exposure of patients with deep brain stimulator with virtual poulation 3.0 and 1.0 anatomical phantoms. *In Proceedings of the* 5^{th} *International Workshop on Computational Human Phantoms*, Seoul, Korea, July 19-22, 2015.

(13) Zastrow E, Yao A, and Kuster N. Practical considerations in experimental evaluations of RF-induced heating of leaded implants Experi-

mental characterization of implant RF-induced heating. *In Proceedings of the* 32^{th} *URSI General Assembly and Scientific Symposium*, Montreal, Candada, August 16-26, 2017.

(14) Lucano E, Kozlov M, Cabot E, Louie S, Horner M, Kainz W, Mendoza GG, Yao A, Zastrow E, Kuster N, and Angelone LM. Interlaboratory study of a computational radiofrequency coil model at 64 MHz. *In Proceedings of* 24^{th} *International Society for Magnetic Resonance in Medicine (ISMRM) Annual Meeting*, Singapore, May 07-13, 2016.

(15) Lucano E, Yao A, Zastrow E, Liberti M, and Kuster N. Test field diversification method for the safety assessment of RF-induced heating of medical implants during MRI at 64 MHz. In *The Joint Annual Meeting of BEMS and EBEA*, 2016.

List of Figures

1.1 Fundamental components of an MRI system with the corresponding wavelengths and frequencies of the magnetic fields generated by these components. 4

1.2 An example AIMD: (a) the Medtronic pacemaker; (b) the basic components of the pacemaker; and (c) a typical *in vivo* position of the pacemaker and the structure of the lead. . . . 6

1.3 Image artefacts (axial view) caused by the presence of a cochlear implant during a spin echo pulse sequence in a 1.5 T MRI scanner (left image) compared to image artefacts resulting after the magnetic implant was replaced with a non-magnetic spacer (right image). 7

1.4 CT scan images of patient implanted with a DBS revealing the lesion – caused by the interaction between the RF field inside the MRI and the DBS inside the patient's brain – surrounding the left electrode of the DBS [34]. 8

2.1 Schematic of the piece-wise excitation method. $\hat{\boldsymbol{l}}$ is the unit tangential vector to the implant at length l. 19

2.2 The experimental system for deriving πX models of implant RF-induced local power deposition. (a) The πX system. (b) Close-up of the local excitation source and the exposed 10-mm conductive tip of the 800-mm implant. 20

2.3 The πX models of the 400- and 800-mm implants, derived from numerical simulations with unbounded medium (black solid), the experimental system with 20 L phantom (orange dotted), and the experimental system with 70 L phantom (blue dotted). Up: magnitude of the models; Down: phase of the models; 21

2.4 Phase distribution along the length of the implants of the exposures used in the calculation of power depositions from the πX models. $|E_{\text{tan}}(l)|$ is always unity. (a) Phase- reversal exposure. (b) Linear-phase exposure. 23

2.5 The power deposition of each generic implant per unit $|E_{\text{tan}}(l)|$ obtained from the direct implant-RF modeling ('o' makers), the numerically-derived πX model (black solid), the experimentally-derived model in 20 L phantom (blue dotted), and the experimentally-derived model in 70 L phantom (orange dotted). 24

2.6 Two examples of radiated test experimental setup providing a phase-reversal incident condition to the implant. The implant routing paths are shown as red solid lines. The phase distribution of $E_{\text{tan}}(l)$ of the phase-reversal incident conditions are illustrated in Figure 2.4a 25

2.7 (a) P_{TIP} as a function of separation distance, d. The estimated power is illustrated with respect to P_{TIP} when only 1 lead is present, P_{∞}, is shown in black. The $|E_{\text{tan}}(l)|$, averaged over the length of the implant, with respect to the average $|E_{\text{tan}}(l)|$ when only 1 lead is present, E_{∞}, is plotted in red. (b) Estimated $|E_{\text{tan}}(l)|$ to the lead due to the presence of a neighboring parallel lead at distance, d. 27

3.1 Induced E-field comparison (E1cm^3) between FATS (maximum intensity projection for all imaging positions) and the ASTM phantom (slice view at the vertical center, where the implant is placed). When both are normalized to a wbSAR of 2 W/kg, the local SAR is about a factor 7 higher in FATS, the maximum E1cm3 about a factor 7 in field (factor 50 in power). This large difference in the E-field is at least partially due to high E-fields in fat-tissues. Due to the low electric conductivity of fat, the difference is not reflected in the local SAR. When evaluating the tangential E-field ($E_{\tan}$) along three orthopedic implant trajectories (evaluated for one imaging position each), $E_{\tan}$ can be considerably higher than in ASTM testing (factor >3 in power). Note the factor 3.3 (10 dB) difference in the scale normalization. The box illustrates the thigh region, where SAR is typically highest in muscle, but the E-field in fat ($*$). 35

3.2 Total minimum-maximum spread of SAR levels reached in the normal operating mode for Virtual population (ViP) model FATS (obese phantom) and THELONIOUS (child phantom), at 1.5 T and 3 T in more than seven different body-coil geometries, covering all major MRI bore sizes. The hdSAR limit is always reaches first in head imaging; the wbSAR is always reached first from sternum to knee imaging. In the neck imaging position, the limit for either hdSAR or wbSAR can be reached first, depending on the patient and body-coil geometry; the same applies to imaging below the knees for wbSAR and pbSAR. The actual pbSAR limit is between 2–10 W/kg, depending on the exposed partial body mass. Exposure is in CP only (no RF shimming). 38

3.3 Total minimum-maximum spread of allowed $B_{1+,\,\mathrm{rms}}$ values to reach the normal operating mode limit for FATS and THELONIOUS at 1.5 T and 3 T in seven different body-coil geometries. The body-coil with 70 cm length and 60 cm diameter is indicated as dashed line, as we performed other evaluations with this geometry only. The spread includes coil lengths between 40–70 cm, with diameters between 60–75 cm. A minimum of 3.5μT (1.5 T) and 2μT (3.0 T) can be applied regardless of model, imaging position, and body-coil geometry, in the normal operating mode (red horizontal lines). 39

3.4 Maximum intensity projection of the induced E-field averaged over 1 cm^3 for FATS (top) and THELONIOUS (bottom). The maximum is projected orthogonal to the depicted plane and for the various imaging positions highlighted in white. Typical routings or AIMDs (DBS, PM, SCS) are shown on the very right images. Note the different dB-scale-reference for FATS and THELONIOUS. 41

3.5 Tangential E-field (E_{tan}) magnitude average along the predefined implant routings shown in Figure 3.4. The patches show histograms obtained for different exposure polarizations (RF shimming), the lines represent the corresponding value obtained with CP exposure. All values normalized to the normal operating mode. The worst-case polarization typically shows up to a doubled E_{tan} compared to CP. 42

3.6 Seven identified typical E-field hotspot locations. *Lateral Enhancement:* (a) shown for the thighs, exists also for the lateral torso and arm. *Dielectric contrast:* (b) pronounced effect around the inner organs. *Anatomical body-constrictions:* (c) around the neck towards the shoulders, (d) axilla, and (e) groin. *Tissue constriction around bones:* (f) shown for the wrist and knee, also exists in the other extremity joint of the elbow and ankle, (g) around the pelvis bone. 43

4.1 (a) The polarization ellipse of the magnetic fields $\vec{H}$, $\vec{H}$ can be decomposed to two orthogonal component of $\vec{H}_x$ and $\vec{H}_y$. ϵ and τ are two parameters used to characterize the ellipticity and tilt angle of the ellipse. (b) Selected polarization states of $\vec{H}$ fields as a function of ϵ and τ. 58

4.2 (a) TFD experimental setup and instrumentation. (b) Top view and side view of the predefined implant routings Rval, R1, and R2 (see Figure 2a) that ensure at least 5 cm separation distance between IUT and phantom boundaries, and 10 cm between parallel lead segments. Rval is used for calibration, R1 and R2 are for validation test. The location of the distal termination of an IUT is indicated by a blue "o" marker. Only the lead routings are shown here; the leads are connected to the implanted pulse generator (IPG) when placed in the setup, in the same way they are connected when the AIMD RF transfer function is obtained. 60

4.3 Tier 3 RF transfer function of the IUT derived in homogeneous TSM (ϵ_r = 78, σ = 0.47 S/m). 62

4.4 (a) Distributions of χ_{Tier3} in the (τ,ϵ) space at 64 MHz and 128 MHz, respectively, with the IUT placed along routing R1. χ_0 and χ_ϕ are highlighted with red solid lines on the colorbars. (b) Same as (a), but for IUT placement along routing R2. 64

4.5 Characteristics of the complex-valued E_{tan} of the 20 selected exposure conditions identified for the TFD experiment. (a) Amplitude $|E_{\text{tan}}|$ (left) and phase ϕ (right) of the $E_{\text{tan}}(l_1)$ along the implant routing trajectory l as a function of exposure condition at 64 MHz. (b) Same as (a), but for 128 MHz. 64

4.6 Summary of the TFD experiment on RF-induced heating enhancement, evaluated for the IUT at 64 MHz. Twenty exposure test configurations were selected to sample the dynamic range of IUT RF-induced heating enhancement. Top: B_1 polarization states of the selected exposure test configurations. The left-hand and right-hand polarized exposures are indicated in green and purple, respectively. Middle: Measured and calculated RF-heating enhancement factors, χ_{TFD} and χ_{Tier3}, of the selected exposure test configurations. Bottom: Deviation between measured χ_{TFD} and Tier 3 [1] calculated χ_{Tier3}. 66

4.7 Summary of the TFD experiment on RF-induced heating enhancement, evaluated for the IUT at 128 MHz. Twenty exposure test configurations were selected to sample the dynamic range of IUT RF-induced heating enhancement. Top: B_1 polarization states of the selected exposure test configurations. The left-hand and right-hand polarized exposures are indicated in green and purple, respectively. Middle: Measured and calculated RF-heating enhancement factors, χ_{TFD} and χ_{Tier3}, of the selected exposure test configurations. Bottom: Deviation between measured χ_{TFD} and Tier 3 [1] calculated χ_{Tier3}. 67

4.8 Sensitivities of the Tier 3 power deposition enhancement factor (χ) at 64 MHz with regard to errors in transfer function amplitude (left) and phase (right) for different linear and circular polarization (CP) modes. 71

4.9 Amplitude (left) and phase (right) reconstruction of the IUT RF transfer function at 64 MHz by using the measurement data with implant placed along routing R1 and R2 to minimize the residual function f_{res} in (4.13). The RF transfer function measured by the piecewise excitation technique is also shown with the dashed line. 72

4.10 RF-heating enhancement factors of the IUT at 64 MHz for different test number (Figure 4.6) obtained with differently reconstructed RF transfer functions. 73

5.1 Examples of normalized SAR and T at locations in the vicinity of two generic implants with 2 mm (blue) and 10 mm (red) tip size, obtained from numerical simulations. 0 dB is referenced to the SAR and T values at z = 0 mm (touch) position. The gray region indicates the locations where measurements are usually performed. 78

5.2 (a) Two-port RF coil and the robotic acquisition system. (b) EX3DV4 dosimetric probe positioned inside the elliptical phantom at a sample location. (c) TSM-filled elliptical phantom, positioned optimally within the RF-coil for iso-electric exposure. (d) Implant placement on the implant holder, optimally designed for iso-electric incident condition to the implant. 80

5.3 (a) Implant samples used in this work. (b) The detailed geometry of implant samples A, B, and C. (c) Top view and side view of the measurement grid. The sample locations are indicated by red dots. 81

5.4 SAR_{HR} of implant samples A, B, and C (0 dB is the maximum SAR of each implant), with the -30 dB contour marked by a white solid line. The x-z plane of the measurement region is shown as the white rectangular box. 83

5.5 Reference simulations setup for implant samples A, B, and C. 84

5.6 Evaluation results of implant sample A (top), sample B (middle) and sample C (bottom), exposed to E_{inc} = 50 V·m^{-1}. (a) XY-plane view of SAR_{meas} and SAR_{opt}. From top to bottom, the SAR distribution in three measurement slices from closest to furthest from the implant is depicted. The measurement slices are the same as those defined in Figure 5.3. (b) The pixel-to-pixel correlation of SAR_{meas} and SAR_{opt}. (c) - (d) show similar information as (a) - (b) for sample B. (e) - (f) show similar information as (a) - (b) for sample C. 89

5.7 Quadratic relationship of P_{TIP} with E_{inc} (i.e., linear relationship of P_{TIP} with E_{inc}^2). P_{TIP} evaluated for implant sample A exposed to E_{inc} = 35, 50, and 70 V·m^{-1} are indicated by the red 'o' markers. The total power deposition of implant sample A as a function of incident tangential electric fields along the implant, derived from the reference full-wave simulation, is indicated by the blue solid line. (a) P_{TIP} as a function of E_{inc}. (b) P_{TIP} as a function of E_{inc}^2. 90

6.1 From left to right: ViP phantoms Fats, Duke, Ella, Billie, and Thelonious. Top: left and right deep-brain stimulator (DBS_{L} and DBS_{R}) routing groups at the head-imaging position. Middle: left and right pacemaker (PM_{L} and PM_{R}) routing groups at the thorax-imaging position. Bottom: left and right spinal-cord stimulator (SCS_{L} and SCS_{R}) routing groups at the pelvis imaging position. 97
6.2 Pacemaker active implantable medical device (AIMD) evaluation area (PM region) used in Tier 2 evaluation, illustrated for the Virtual Population (ViP) phantom Duke. 99
6.3 Improvements in the quality and consistency of tissue segmentation in Virtual Population (ViP) 3.0 compared with ViP 1.x phantoms: tendons of (a) ViP 1.x and (b) ViP 3.0; the circulatory system of (c) ViP 1.x and (d) ViP 3.0. 102
6.4 Improvements in the quality of tissue (permittivity ϵ_r is shown) and SAR_{10g} distributions in ViP 3.0 compared with ViP 1.x phantoms for the ViP phantom Ella: ϵ_r of (a) ViP 1.x and (b) ViP 3.0; (c) difference in tissue permittivity distribution ($\Delta\epsilon_r$) between ViP 1.x and ViP 3.0; (d) difference in SAR_{10g} distribution (ΔpsSAR10g) between ViP 1.x and ViP 3.0. . . 104
6.5 Visual depiction of the information in Tables 6.2 and 6.3: (a) $\text{p}_{99}E_{\text{10g}}$ with the derived Tier 1 incident values and (b) $\text{p}_{95}E_{\text{10g}}$ with the derived Tier 2 incident values within the pacemaker at the normal MRI operating mode limit for the head-, thorax-, and pelvis-imaging positions; the bars illustrate the p_pE_{10g} for each ViP phantom, with the value derived from ViP 3.0 indicated by the orange inset bar. Lower y axis: the difference $\Delta\text{p}_pE_{\text{10g}}$ in dB between ViP 1.x and ViP 3.0. 108

6.6 Magnitude (top) and phase (bottom) of $E_{\tan}(l_1)$ averaged over 100 routings (solid lines) and the variations within 100 routings (shaded regions) for each routing group in the Virtual Population (ViP) phantom Ella with ViP 1.x results in blue and ViP 3.0 results in orange. 112

6.7 Distribution of Tier 3 power deposition (P_{dep}) for deep brain stimulator (DBS) (blue), pacemaker (PM) (green), and spinal cord stimulator (SCS) (red) active implantable medical devices (AIMDs) in all five Virtual Population (ViP) 1.x (lower histogram) and ViP 3.0 (upper histogram) phantoms. 113

6.8 Tier 4 evaluation of the left generic deep-brain stimulator (DBS_{L}) active implantable medical device (AIMD) in Duke at the head-imaging position. Specific absorption rate (SAR) distribution in a sagittal plane through the tip of active implantable medical device (AIMD) for (a) Virtual Population (ViP) 1.x and (b) ViP 3.0; (c) the surface enclosing the tissue volume at the vicinity of the distal tip of the DBS_{L} AIMD with the local SAR contained tissue volume within the -30 dB contour line relative to the maximum SAR of ViP 1.x (red) and ViP 3.0 (blue); (d) histogram of SAR within the tissue region at close proximity to the distal tip of the DBS_{L} AIMD (shown as a yellow box in (a) and (b) for ViP 1.x (red) and ViP 3.0 (blue). 114

7.1 Proposed *in silico* trial workflow based on the IEC standard for patients without medical implants[20] and Tier 3 evaluation of RF-induced effects for patients with medical implants[1] 123

7.2 Summary of the data selection for the *in silico* trial. Bottom-right: data filter. Left: illustration of phantom 'Duke' indicating the three imaging positions. Upper-right: Ellipticity (ϵ) and orientation (τ) angles represented on planar projection of the Poincaré sphere [94]. 124

7.3 Data distribution for head, thorax, and foot imaging. Top-left and -right: distributions of power deposition of the IUT (P_{dep}) as a function of B_1 polarization at the normal operating mode SAR limits and at a fixed B_{1+} level of 1μT, respectively. Bottom-left: distribution of the B_{1+} magnitude averaged over iso-center slice ($\langle|B_{1+}|\rangle$) as a function of B_1 polarization at the normal operating mode SAR limits. Bottom-right: spatial distribution of B_{1+} magnitude over iso-center slice for circular-polarized B_1. The averaged magnitude and coefficient of variation of B_{1+} ($\langle|B_{1+}|\rangle$ and $B_{1+,cov}$) are indicated in μT and % at bottom-right of the figures. 126

7.4 Data distribution for head, thorax, and foot imaging. For each imaging position, top-left, top-right, and bottom-left: distributions of B_{1+} magnitude averaged over iso-center slice ($\langle|B_{1+}|\rangle$), coefficient of variation of B_{1+} ($B_{1+,cov}$), and power deposition of the IUT (P_{dep}) as a function of B_1 127

8.1 (a) Geometry of the IUTs used in the study. Wire and insulation are concentric cylinders and electrodes are either cylindrical (top) or helical (bottom). (b) Tissue model of IUT-embedding media used in Section 8.4.1 and Section 8.4.2. 136

8.2 Illustration of the anatomical model of spinal cord and selected three positions where electrode of the generic spinal cord stimulator was located. 139

8.3 Application of proposed simplifications to the clinical scenario of a patient with a generic pacemaker. The different simplification stages where $P2\Delta T$ is calculated are illustrated. Top: no simplification (clinical), Middle: partial simplification, and Bottom: full simplification. Note: the RF-coil is not depicted. 141

8.4 Application of proposed simplifications to the clinical scenario of a patient with a generic spinal cord stimulator. The different simplification stages where $P2\Delta T$ is calculated are illustrated. Top: no simplification (clinical), Middle: partial simplification, and Bottom: full simplification. Note: the RF-coil is not depicted. 142

8.5 (a) $P2\Delta T$ for different electrodes as a function of IUT electrical length (L·λ^{-1}). (b) $P2\Delta T$ as a function of IUT insulation radius, c, evaluated for IUTs with different wire radii, a. (c) $P2\Delta T$ as a function of incident conditions, evaluated for IUTs exposed to linear-phase tangential E-field of different phase gradient (0 - 30 rad/m). 143
8.6 $P2\Delta T$ for implants with various insulation thicknesses (c) embedded in different tissue distributions. The BHE is solved both numerically (FDTD-BHE) and with analytical Green's function (G-BHE). The heating factors calculated with FDTD-BHE are indicated by 'o' and 'x' markers. The heating factors calculated with G-BHE are indicated by dash lines. . . . 144
8.7 The E-field and SAR distributions corresponding to the three positions defined in Figure 2 145

List of Tables

3.1 Potential patient hazards and corresponding test methods list in ISO/TS 10974 [1]. In this review, we classify the hazard into mechanical, malfunction, and thermal, and add the image distortion as a potential indirect harm. 45

4.1 Summarized power deposition obtained from Tier 3 [1] prediction ($P_{\text{dep,Tier3}}$) and validation tests ($P_{\text{dep,TFD}}$) 68

4.2 Uncertainty budget of enhancement factor (χ) evaluation . . 69

5.1 Uncertainty budget of the estimated power deposition of the AIMD obtained with the traditional method and with the proposed method. 85

5.2 Summary of estimated power deposition obtained from proposed method, traditional method, and reference simulations. The deviation of the values obtained with proposed and traditional method from the reference values, $||\Delta_{\text{prop}}||$ and $||\Delta_{\text{trad}}||$, are provided in dB. 86

6.1 Heights and Weights of the Five Phantoms Studied From ViP 1.0 and ViP 3.0, Obtained From Discretized Models With a Uniform Grid Size of 0.5x0.5x0.5 mm^3. 103

6.2 $\mathrm{p}_p E_{\text{10g}}$ (99th Percentile of the 10g-Average E-field) at head, thorax, and pelvis imaging positions. Tier 1 exposures are indicated in bold. 106

6.3 p$_pE_{\text{10g}}$ (95th Percentile of the 10g-Average E-field) Within the Evaluation Area Containing the Pacemaker AIMD (PM region) at Head-, Thorax-, and Pelvis-Imaging Positions Tier 2 exposures are indicated in Bold. 107

6.4 Tier 3 power deposition, evaluated for the AIMD along DBS$_{\text{L}}$ and DBS$_{\text{R}}$ at the head imaging position. The 95^{th} percentile value of P_{dep} are summarized for ViP 1.0 and ViP 3.0. $||\Delta||$ is the absolute value of the difference in 95^{th} percentile of P_{dep} for ViP 1.0 and ViP 3.0. $||\Delta_{\text{ViP}}||$ indicates the variation of P_{dep} across the patient population. 109

6.5 Tier 3 power deposition, evaluated for the AIMD along PM$_{\text{L}}$ and PM$_{\text{R}}$ at the head imaging position. The 95^{th} percentile value of P_{dep} are summarized for ViP 1.0 and ViP 3.0. $||\Delta||$ is the absolute value of the difference in 95^{th} percentile of P_{dep} for ViP 1.0 and ViP 3.0. $||\Delta_{\text{ViP}}||$ indicates the variation of P_{dep} across the patient population. 110

6.6 Tier 3 power deposition, evaluated for the AIMD along SCS$_{\text{L}}$ and SCS$_{\text{R}}$ at the head imaging position. The 95^{th} percentile value of P_{dep} are summarized for ViP 1.0 and ViP 3.0. $||\Delta||$ is the absolute value of the difference in 95^{th} percentile of P_{dep} for ViP 1.0 and ViP 3.0. $||\Delta_{\text{ViP}}||$ indicates the variation of P_{dep} across the patient population. 111

6.7 Tier 4-estimated *in vivo* power deposition obtained with Duke phantom of ViP phantom Duke for the selected clinical scenarios. $||\Delta||$ is the absolute value of the difference in the Tier 4-estimated *in vivo* power deposition of ViP 1.0 and ViP 3.0. 115

8.1 Summary of the dielectric and thermal properties of the tissues. 137

8.2 Tissue assignment of the tissue model depicted in Figure 8.1, for different tissue distribution used in Section 8.4.2. 140

8.3 Summary of parameters, associated with the IUT, tissue distribution, and RF-exposure, of the two clinical scenarios. . . 140

8.4 Summary of $P2\Delta T$ and computational resource required for a generic pacemaker for the different simplifications . . . 148

8.5 Summary of $P2\Delta T$ and computational resource required for a generic spinal-cord stimulator for the different simplifications 149

Bibliography

[1] *ISO/TS10974, Assessment of the safety of magnetic resonance imaging for patients with an active implantable medical device*. International Organization for Standardization, Geneva, Switzerland, 2012.

[2] Bloch F, Hansen W, and Packard M. The nuclear induction experiment. *Physical Review*, 70(7-8):474–485, 1946.

[3] McRobbie DW, Moore EA, Graves MJ, and Prince MR. *MRI from Picture to Proton*. Cambridge University Press, 2007.

[4] Bottomley P and Andrew E. RF magnetic field penetration, phase shift and power dissipation in biological tissue: implication for NMR imaging. *Physics in Medicine and Biology*, 23(4):630–643, 1978.

[5] Bottomley P and Edelstein W. Power deposition in whole body nmr imaging. *Medical Physics*, 8:510–512, 1981.

[6] Bottomley P, Redington R, and Edelstein W. Estimating radiofrequency power deposition in body nmr imaging. *Magnetic Resonance in Medicine*, 2:336–349, 1985.

[7] Shellock FG and Bierman H. The safety of MRI. *JAMA*, 261(23):3412, 1989.

[8] Schenck J, Dumoulin C, Redington R, Kressel H, Elliott R, and McDougall I. Human exposure to 4.0-tesla magnetic fields in a whole-body scanner. *Medical Physics*, 19(4):1089–1098, 1992.

[9] Kangarlu A, Burgess R, Zhu H, Nakayama T, Hamlin R, and Abduljalil A. Cognitive, cardiac and physiological safety studies in ultra

high field magnetic resonance imaging. *Magnetic Resonance Imaging*, 17(10):1407–1416, 1999.

[10] Bourland J, Nyenhuis J, and Schaefer D. Physiologic effects of intense MRI gradient fields. *Neuroimaging Clincs of North America*, 9(2):363–377, 1999.

[11] Irnich W and Schmitt F. Magnetostimulation in MRI. *Magnetic Resonance in Medicine*, 33:619–623, 1995.

[12] Bandettini P, Jesmanowicz A, Kylen J, Birn R, and Hyde J. Functional MRI of brain activation induced by scanner acoustic noise. *Magnetic Resonance in Medicine*, 39:410–416, 1998.

[13] Cho Z, Park S, and Kim J. Analysis of acoustic noise in MRI. *Magnetic Resonance Imaging*, 15:815–822, 1997.

[14] Kangarlu A, Schellock F, and Chakeres D. 8.0-Tesla MR system: temperature changes associated with radiofrequency-induced heating of a head phantom. *Journal of Magnetic Resonance Imaging*, 17:220–226, 2003.

[15] Shellock FG. Magnetic resonance safety update 2002: implants and devices. *Journal of Magnetic Resonance Imaging*, 16(5):485–496, 2002.

[16] ICNIRP. Guidelines for limiting exposure to time-varing electric, magnetic and electromagnetic fields (up to 300 ghz). *Health Physics*, 74(4):494–522, 1998.

[17] IEEE. *IEEE Standard C95.6-2002, Standard for safety levels with respect to human exposure to electromagnetic fields, 0-3 kHz*. The institue of Electrical and Electronics Engineers, Inc., New York, 2002.

[18] *Criteria for significant risk investigations of magnetic resonance diagnostic devices*. MD: Center for Devies and Radiological Health, US Food and Drug Adminstration, Rockville, USA, 2014.

[19] ICNIRP. Statement on medical magnetic resonance (MR) procedures: protection of patients. *Health Physics*, 87(2):197–216, 2004.

[20] IEC. *IEC Standard 60601-2-33, Medical electrical equipment - particular requirements for the basic safety and essential performance of magnetic resonance equipment for medical diagnosis, 3rd edition*. International Electrotechnical Commission (IEC), Geneva, 2010.

[21] Shellock FG and J.Schaefer D. MR procedures: biologic effects, safety, and patient care. *Radiology*, 232:635–652, 2004.

[22] Kanal E and Schellock F. Policies, guidelines and recommendations for MR imaging safety and patient management: patient monitoring during mr examinations. *Journal of Magnetic Resonance Imaging*, 2:247–248, 1992.

[23] Shellock FG. Radiofrequency energy-induced heating during MR procedures: a review. *Journal of Magnetic Resonance Imaging*, 12:30–36, 2000.

[24] Dempsey MF, Condon B, and Hadley D. Investigation of the factors responsible to burns during MRI. *Journal of Magnetic Resonance Imaging*, 13:627–631, 2001.

[25] Dempsey MF, Condon B, and Hadley DM. MRI safety review. *Seminars in Ultrasound CT and MRI*, 23(5):392–401, 2002.

[26] Nyenhuis JA, Park SM, Kamondetdacha R, Amjad A, Shellock FG, and Rezai AR. MRI and implanted medical devices: Basic interactions with an emphasis on heating. *IEEE Trans. Device Mater. Reliab.*, 5(3):467–479, 2005.

[27] Luechinger R, Duru F, Scheidegger MB, Boesiger P, and Candinas R. Force and torque effects of a 1.5-Tesla MRI scanner on cardiac pacemaker and ICDs. *Journal of Pacing and Clinical Electrophysiology*, 24(2):199–205, 2001.

[28] Gimbel J. Unexpected asystole during 3T magnetic resonance imaging of a pacemaker dependent patient with a ”modern” pacemaker. *Europace*, 11(9):1241–1242, 2009.

[29] Nordbeck P, Ertl G, and Ritter O. Magnetic resonance imaging safety in pacemaker and implantable cardioverter defibrillator patients: How far have we come? *European Heart Journal*, 36(24):1505–1511, 2015.

[30] Davis L, Kaufman L, and Margulis R. Potential hazards in NMR imaging: heating effects of changing magnetic fields and RF fields on small metallic implants. *American Journal of Roentgenology*, 137(4):857–860, 1981.

[31] Online M. Medical procedure for med-el ci system.

[32] Luechinger R, Zeijlemaker VA, Pedersen EM, Mortensen P, Falk E, Duru F, Candinas R, and Boesiger P. In vivo heating of pacemaker leads during magnetic resonance imaging. *European Heart Journal*, 26(4):376–383, 2005.

[33] Mattei E, Triventi M, Calcagnini G, Censi F, Kainz W, Mendoza G, Bassen HI, and Bartolini P. Complexity of MRI induced heating on metallic leads: Experimental measurements of 374 configurations. *BioMedical Engineering OnLine*, 7(1):11, 2008.

[34] Henderson JM, Tkach J, Phillips M, Baker K, Shellock FG, and Rezai A. Permanent neurological deficit related to magnetic resonance imaging in a patient with implanted deep brain stimulation electrodes for parkinson's disease: Case report. *Neurosurgery*, 57(5):E1063–E1063, 2005.

[35] Spiegel J, Fuss G, Backens M, Reith W, Margnus T, Becker G, Moringlane JR, and Dillmann U. Transient dystonia following magnetic resonance imaging a patient with deep brain stimulation electrodes for the treatment of Parkinson disease: Case report. *Journal of Neurosurgery*, 99(4):772 – 774, 2003.

[36] Baker KB, Tkach JA, Phillips M, and Rezai AR. Variability in RF induced heating of a deep brain stimulation implant across MR systems. *Journal of Magnetic Resonance Imaging*, 24(6):1236–1242, 2006.

[37] Nordbeck P, Weiss I, Ehses P, Ritter O, Warmuth M, Fidler F, Herold V, Jakob PM, Ladd ME, Quick HH, and Bauer WR. Measuring RF-induced currents inside implants: Impact of device configuration on MRI safety of cardiac pacemaker leads. *Magnetic Resonance in Medicine*, 61(3):570–578, 2009.

[38] Wilkoff BL, Albert T, Lazebnik M, Park SM, Edmonson J, Herberg B, Golnitz J, Wixon S, Peltier J, Yoon H, Willey S, and Safriel Y. Safe magnetic resonance imaging scanning of patients with cardiac rhythm devices: a role for computer modeling. *Heart Rhythm*, 10(12):1815–1821, 2013.

[39] Gold MR, Sommer T, Schwitter J, Al Fagih A, Albert T, Merkely B, Peterson M, Ciuffo A, Lee S, Landborg L, Cerkvenik J, and Kanal E. Full-body MRI in patients with an implantable cardioverter-defibrillator: Primary results of a randomized study. *Journal of the American College of Cardiology*, 65(24):2581–2588, 2015.

[40] Gimbel JR. Randomized trials of pacemaker and lead system for safe scanning at 1.5 Tesla. *Heart Rhythm*, 2013.

[41] Online M. https://www.medel.com/in/cochlear-implants-mri-safety/.

[42] FDA. FDA approval of medtronic activa tremor control system., 1997.

[43] Zeng FG. Trends in cochlear implants. *Trends Amplif*, 8(1):1–34, 2004.

[44] Hand JW. Modelling the interaction of electromagnetic fields (10 MHz–10 GHz) with the human body: methods and applications. *Physics in Medicine and Biology*, 53(16):R243–R286, 2008.

[45] Beard BB, Kainz W, Onishi T, Iyama T, Watanabe S, Fujiwara O, Wang J, Bit-Babik G, Faraone A, Wiart J, Christ A, Kuster N, Lee AK, Kroeze H, Siegbahn M, Keshvari J, Abrishamkar H, Simon W, Manteuffel D, and Nikoloski N. Comparisons of Computed Mobile Phone Induced SAR in the SAM Phantom to That in Anatomically Correct Models of the Human Head. *IEEE Transactions on Electromagnetic Compatibility*, 48(2):397–407, 2006.

[46] Zastrow E, Yao A, and Kuster N. Practical considerations in experimental evaluations of RF-induced heating of leaded implants Experimental characterization of implant RF-induced heating. *In Proceedings of the* 32^{th} *URSI General Assembly and Scientific Symposium*, Montreal, Candada, August 16-26, 2017.

[47] Yeung CJ and Atalar E. A green's function approach to local RF heating in interventional MRI. *Medical physics*, 28(5):826–832, 2001.

[48] Córcoles J, Zastrow E, and Kuster N. Convex optimization of MRI exposure for mitigation of RF-heating from active medical implants. *Physics in Medicine and Biology*, 60(18):7293–7308, 2015.

[49] Park SM, Kamondetdacha R, and Nyenhuis JA. Calculation of MRI-induced heating of an implanted medical lead wire with an electric field transfer function. *Journal of Magnetic Resonance Imaging*, 26:1278–1285, 2007.

[50] Taflove A and Hagness SC. *Computational electrodynamics: the finite-difference time-domain method*. Artech House, 2005.

[51] Murbach M, Yao A, Zastrow E, Kainz W, and Kuster N. Electromagnetic MRI Safety with and without Implantable Metallic Devices: A Review. submitted to *Journal of Magnetic Resonance in Imaging*, 2019.

[52] Kelly W, Paglen P, and Pearson J. Ferromagnetism of intraocular foreign body causes unilateral blindness after mr study. *AJNR*, pages 243–245, 1986.

[53] Brown T, Goldstein B, and Little J. Severe burns resulting from magnetic resonance imaging with cardiopulmonary moitoring: Risks and relevant safety precautions. *Am J Phys Med Rehabil*, 72:166–167, 1993.

[54] Klucznik R, Carrier D, and Pyka R. Placement of ferromagnetic intracerebral aneurysm clip in a magnetic field with fatal outcome. *Radiology*, pages 855–856, 1993.

[55] Zrinzo L, Yoshida F, Hariz MI, Thornton J, Foltynie T, Yousry TA, and Limousin P. Clinical safety of brain magnetic resonance imaing with implanted deep brain stimulation hardware:large case series and review of the literature. *World Neurosurgery*, 76(1/2):164–172, 2011.

[56] Dujovny M, Kossovsky N, and Kossowsky R. Aneurysm clip motion during magnetic resonance imaging: In vivo experimental study with metallurgical factor analysis. *Neurosurgery*, 17:547–550, 1985.

[57] Sommer T, Vahlhaus C, Lauck G, Smekal AV, Reinke M, Hofer U, Block W, Träber F, Schneider C, Gieseke J, Jung W, and Schild H. MR imaging and cardiac pacemakers: in vitro evaluation and in vivo studies in 51 patients at 0.5 T. *Radiology*, 215(3):869–879, 2000.

[58] Buchli R, Boesinger P, and Meier D. Heating effects of metallic implants by MRI examinations. *Magnetic Resonance in Medicine*, 7:255–261, 1988.

[59] Chou CK, McDougall JA, and Chan KW. RF heating of implanted spinal fusion stimulator during magnetic resonance imaging. *IEEE Transactions on Biomedical Engineering*, 44(5):367–373, 1997.

[60] Majdani O, Rau T, Gotz F, Zimmerling M, Lenarz M, Lenarz T, and Leinung M. Artifacts caused by cochlear implants with non-removable magnets in 3T MRI: phantom and cadaveric studies. *European Archives of Oto-Rhino-Laryngology*, 266(12):1885–1890, 2009.

[61] Murbach M, Neufeld E, Capstick M, Kainz W, Brunner D, Samaras T, Pruessmann KP, and Kuster N. Thermal tissue damage model analyzed for different whole-body SAR and scan durations for standard MR body coils. *Magnetic Resonance in Medicine*, 71(1):421–431, 2013.

[62] Murbach M, Neufeld E, Zastrow E, Corcoles J, and Kuster N. Virtual population-based assessment of the impact of 3 Tesla radiofrequency shimming and thermoregulation on safety and B1+ uniformity. *Magnetic Resonance in Medicine*, 76:986–997, 2016.

[63] *ASTM Standard F 2182-2002a, Standard test method for measurement of radio frequency induced heating near passive implants during magnetic resonance imaging*. Number December. ASTM International, 2002.

[64] Radiology A. https://appliedradiology.com/articles/siemens-obtains-first-ce-approval-for-ultra-high-field-7t-mr-scanner.

[65] van der Graaf AWM, Bhagirath P, and Götte MJW. MRI and cardiac implantable electronic devices; current status and required safety conditions. *Netherlands Heart Journal*, 22(6):269–276, 2014.

[66] Bencsik M, Bowtell R, and Bowley R. Electric fields induced in the human body by time-varying magnetic field gradients in MRI: numerical calculations and correlation analysis. *Physics in Medicine and Biology*, 52:2337–2353, 2007.

[67] Murbach M, Neufeld E, Kainz W, Pruessmann KP, and Kuster N. Whole-body and local RF absorption in human models as a function of anatomy and position within 1.5 T MR body coil. *Magnetic Resonance in Medicine*, 845:839–845, 2014.

[68] Marshall J, Martin T, Downie J, and Malisza K. A comprehensive analysis of mri research risks: In support of full disclosure. *The Canadian Journal of Neurological Sciences*, 34(1):11–17, 2007.

[69] Murbach M, Zastrow E, Neufeld E, Cabot E, Kainz W, and Kuster N. Heating and Safety Concerns of the Radio-Frequency Field in MRI. *Current Radiology Reports*, 3(12):45, 2015.

[70] Condon B and Hadley D. Potential mr hazard to patients with metallic heart valves: The lenz effct. *Journal of Magnetic Resonance Imaging*, 12:171–176, 2000.

[71] Robertson N, Diaz-Gomez M, and Condon B. Estimation of torque on mechanical heart valves due to mri including an estimation of the lenz effect uding a computational model. *Physics in Medicine and Biology*, pages 3793–3807, 2000.

[72] Strach K, Naehle C, Muhlsteffen A, Hinz M, Bernstein A, Thomas D, Linhart M, Meyer C, Bitaraf S, Schild H, and Sommer T. Low-field magnetic resonance imaging: increased safety for pacemaker patients? *Europace*, 12:952–960, 2010.

[73] Cohen J, Costa H, and Russo R. Determining the risks of magnetic resonance imaging at 1.5 tesla for patients with pacemakers and implantable cardioverter defibrillators. *American Journal of Cardiology*, 110:1631–1636, 2012.

[74] Boilson BA, Wokhlu A, Acker NG, Felmlee JP, Watson RE, Julsrud PR, Friedman PA, Cha YM, Rea RF, L.Hayes D, and Shen WK. Safety of magnetic resonance imaging in patients with permanent

pacemakers: A collaborative clinical approach. *Journal of Interventional Cardiac Electrophysiology*, 33(1):59–67, 2012.

[75] Teissl C, Kremser MC, Hochmair ES, and Hochmair-Desoyer IJ. Magnetic resonance imaging and cochlear implants: compatibility and safety aspects. *Journal of Magnetic Resonance Imaging*, 9:26–38, 1999.

[76] Risi F, Saldanha A, Leigh R, and Gibson P. Magnetic resonance imaging safety of nucleus 24 cochlear implants at 3.0 t. *International Congress Series*, 1273:394–398, 2004.

[77] Dempsey MF and Condon B. Thermal injuries associated with MRI. *Clinical Radiology*, 56(6):457–465, 2001.

[78] Roguin A, Zviman MM, Meininger GR, Rodrigues ER, Dickfeld TM, Bluemke DA, Lardo A, Berger RD, Calkins H, and Halperin HR. Modern pacemaker and implantable cardioverter/defibrillator systems can be magnetic resonance imaging safe. *Circulation*, 110(5):475–482, 2004.

[79] Achenbach S, Moshage W, Diem B, Bieberle T, Schibgilla V, and Bachmann K. Effects of magnetic resonance imaging on cardiac pacemakers and electrodes. *American Heart Journal*, 134(3):467–473, 1997.

[80] Graf H, Steidle G, and Schick F. Heating of metallic implants and instruments induced by gradient switching in a 1.5-tesla whole-body unit. *Journal of Magnetic Resonance Imaging*, 26:1328–1333, 2007.

[81] Cabot E, Zastrow E, and Kuster N. Safety assessment of aimds under mri exposure: Tier3 vs. tier4 evaluation of local rf-induced heating. In *International Symposium on Electromagnetic Compatibility,Tokyo*, pages 237–240, 2014.

[82] Schueler BA, Parrish TB, Lin JC, Hammer BE, Pangrle BJ, Ritenour ER, Kucharczyk J, and Truwit CL. Mri compatibility and visibility assessment of implantable medical devices. *Journal of Magnetic Resonance Imaging*, 9(4):596–603, 1999.

[83] Zastrow E, Capstick M, and Kuster N. Experimental systems for rf-heating characterization of medical implants during mri. *In Proceedings of* 24^{th} *International Society for Magnetic Resonance in Medicine*, 2016.

[84] Liorni I, Neufeld E, Kühn S, Murbach M, Zastrow E, Kainz W, and Kuster N. Novel mechanistic model and computational approximation for electromagnetic safety evaluations of electrically short implants. *Physics in Mecicine and Biology*, 63:1–14, 2018.

[85] Sapareto S and Dewey W. Thermal dose determination in cancer therapy. *International Journal of Radiation Oncology, Biology, Physics*, 10:787–800, 1984.

[86] Yao A, Zastrow E, Neufeld E, Cabanes-Sempere M, and Kuster N. Novel test field diversity method for RF transfer function validation required for demonstrating MRI safety of active implantable medical devices. submitted to *Magnetic Resonance in Medicine*, 2019.

[87] Cabot E, Lloyd T, Christ A, Kainz W, Douglas M, Stenzel G, Wedan S, and Kuster N. Evaluation of the RF heating of a generic deep brain stimulator exposed in 1.5T magnetic resonance scanners. *Bioelectromagnetics*, 34(2):104–113, 2013.

[88] Calcagnini G, Triventi M, Censi F, Mattei E, Bartolini P, Kainz W, and H.I B. In vitro investigation of pacemaker lead heating induced by magnetic resonance imaging: role of implant geometry. *Journal of Magnetic Resonance Imaging*, 4(28):879–886, 2008.

[89] Mattei E, Gentili G, Censi F, Triventi M, and Calcagnini G. Impact of capped and uncapped abandoned leads on the heating of an MR-conditional pacemaker implant. *Magnetic Resonance in Medicine*, 73:390–400, 2015.

[90] Zastrow E, Cabot E, Christ A, and Kuster N. Experimental phantoms for the assessment of medical implant leads induced SAR under a linear-phase incident field condition. *2011 30th URSI General Assembly and Scientific Symposium, URSIGASS 2011*, pages 2–5, 2011.

[91] Brink W, Gulani V, and Webb A. Clinical applications of dual-channel transmit MRI: A review. *Journal of Magnetic Resonance Imaging*, 42(4):855–869, 2015.

[92] de Heer P, Brink W, Kooij B, and Webb A. Increasing signal homogeneity and image quality in abdominal imaging at 3T with very high permittivity materials. *Magnetic Resonance in Medicine*, 68(4):1317–1324, 2012.

[93] Brink W, Remis R, and Webb A. A theoretical approach based on electromagnetic scattering for analysing dielectric shimming in high-field MRI. *Magnetic Resonance in Medicine*, 75(5):2185–2194, 2016.

[94] Kraus JD and Carver KR. *Electromagnetics*. New York: a.o: McGraw-Hill, 1973.

[95] Pokovic K, Schmid T, Frohlich J, and Kuster N. Novel probes and evaluation procedures to assess field magnitude and polarization. *IEEE Transactions on Electromagnetic Compatibility*, 2000.

[96] Yao A, Zastrow E, and Kuster N. Data-driven experimental evaluation method for the safety assessment of implants with respect to RF-induced heating during MRI. *Radio Science*, 53, 2018.

[97] Neufeld E, Kuehn S, Szekely G, and Kuster N. Measurement, simulation, and uncertainty assessment of implant heating during MRI. *Physics in medicine and biology*, 54(13):4151–4169, 2009.

[98] Yao A, Zastrow E, and Kuster N. Data-driven experimental evaluation method for the safety assessment of implants with respect to RF-induced heating during MRI. *Radio Science*, 53(6):700–709, 2018.

[99] Gauden AJ, Phal PM, and Drummond KJ. MRI safety: nephrogenic systemic fibrosis and other risks. *Journal of Clinical Neuroscience*, 17(9):1097–1104, 2010.

[100] Shellock FG and Shellock VJ. Vascular access ports and catheters: ex vivo testing of ferromagnetism, heating, and artifacts associated with MR imaging. *Magnetic Resonance Imaging*, 14(4):443–447, 1996.

[101] Rezai AR, Finelli D, Nyenhuis JA, Hrdlicka G, Tkach J, Sharan A, Rugieri P, Stypulkowski PH, and Shellock FG. Neurostimulation systems for deep brain stimulation: In vitro evaluation of magnetic resonance imaging-related heating at 1.5 Tesla. *Journal of Magnetic Resonance Imaging*, 15(3):241–250, 2002.

[102] Ruggera PS, Witters DM, Maltzahn GV, and Bassen HI. In vitro assessment of tissue heating near metallic medical implants by exposure to pulsed radio frequency diathermy. *Physics in medicine and biology*, 48(17):2919–2928, 2003.

[103] Baker KB, Tkach JA, Nyenhuis JA, Phillips M, Shellock FG, Gonzalez-Martinez J, and Rezai AR. Evaluation of specific absorption rate as a dosimeter of MRI-related implant heating. *Journal of Magnetic Resonance Imaging*, 20(2):315–320, 2004.

[104] Muranaka H, Horiguchi T, Usui S, Ueda Y, Nakamura O, and Ikeda F. Dependence of RF heating on SAR and implant position in a 1.5T MR system. *Magnetic Resonance in Medical Sciences*, 6(4):199–209, 2007.

[105] Lucano E, Yao A, Zastrow E, Liberti M, and Kuster N. Test field diversification method for the safety assessment of RF-induced heating of medical implants during MRI at 64 MHz. *In Proceedings of the 29th Annual International Conference of the IEEE EMBS*, 2016.

[106] Liu Y, Chen J, Shellock FG, and Kainz W. Computational and experimental studies of an orthopedic implant: MRI-related heating at 1.5-T/64-MHz and 3-T/128-MHz. *Journal of Magnetic Resonance Imaging*, 37(2):491–497, 2013.

[107] Collins CM, Liu W, Wang J, Gruetter R, Vaughan TJ, Ugurbil K, and Smith MB. Temperature and SAR calculations for a human head within volume and surface coils at 64 and 300 MHz. *Journal of Magnetic Resonance Imaging*, 19(5):650–656, 2004.

[108] Yao A, Zastrow E, Cabot E, Lloyd B, Schneider B, Kainz W, and Kuster N. Anatomical model uncertainty for RF safety evaluation of AIMD under MRI exposure. *Bioelctromagnetics (published online ahead of print)*, 2019.

[109] Ackerman MJ. The visible human project. *Proceedings of the IEEE*, 86(3):504–511, 1998.

[110] Kim CH, Choi SH, Jeong JH, Lee C, and Chung MS. HDRK-Man: a whole-body voxel model based on high-resolution color slice images

of a Korean adult male cadaver. *Physics in Medicine and Biology*, 53(15):4093–4106, 2008.

[111] Petoussi-Henss N, Zankl M, Fill U, and Regulla D. The GSF family of voxel phantoms. *Physics in Medicine and Biology*, 47(1):89–106, 2002.

[112] Lee C, Lee J, and Lee C. Korean adult male voxel model KORMAN segmented from magnetic resonance images. *Medical Physics*, 31(5):1017, 2004.

[113] Dimbylow P. Development of the female voxel phantom, NAOMI, and its application to calculations of induced current densities and electric fields from applied low frequency magnetic and electric fields. *Physics in Medicine and Biology*, 50(6):1047–1070, 2005.

[114] Zhang B, Ma J, Liu L, and Cheng J. CNMAN: a Chinese adult male voxel phantom constructed from color photographs of a visible anatomical data set. *Radiation Protection Dosimetry*, 124(2):130–136, 2007.

[115] Sato K, Noguchi H, Emoto Y, Koga S, and Saito K. Development of a japanese adult female voxel phantom. *Journal of Nuclear Science and Technology*, 46(9):907–913, 2009.

[116] Sato K, Noguchi H, Emoto Y, Koga S, and Saito K. Japanese adult male voxel phantom constructed on the basis of CT images. *Radiation Protection Dosimetry*, 123(3):337–344, 2007.

[117] Christ A, Kainz W, Hahn EG, Honegger K, Zefferer M, Neufeld E, Rascher W, Janka R, Bautz W, Chen J, Kiefer B, Schmitt P, Hollenbach HP, Shen J, Oberle M, Szczerba D, Kam A, Guag JW, and Kuster N. The Virtual Family—development of surface-based anatomical models of two adults and two children for dosimetric simulations. *Physics in Medicine and Biology*, 55(2):N23–N38, 2010.

[118] Brink WM and Webb AG. High permittivity pads reduce specific absorption rate, improve B1 homogeneity, and increase contrast-to-noise ratio for functional cardiac MRI at 3 T. *Magnetic Resonance in Medicine*, 71(4):1632–1640, 2014.

[119] Gosselin MC, Kuhn S, and Kuster N. Experimental and numerical assessment of low-frequency current distributions from UMTS and GSM mobile phones. *Physics in Medicine and Biology*, 58(23):8339–8357, 2013.

[120] Fiocchi S, Liorni I, Parazzini M, Ravazzani, and Fiocc. Assessment of foetal exposure to the homogeneous magnetic field harmonic spectrum generated by electricity transmission and distribution networks. *International Journal of Environmental Research and Public Health*, 12(4):3667–3690, 2015.

[121] Christ A, Guldimann R, Buhlmann B, Zefferer M, Bakker JF, van Rhoon GC, and Kuster N. Exposure of the human body to professional and domestic induction cooktops compared to the basic restrictions. *Bioelectromagnetics*, 33(8):695–705, 2012.

[122] Meng Y, Hadimani RL, Crowther LJ, Xu Z, Qu J, and Jiles DC. Deep brain transcranial magnetic stimulation using variable ”halo coil” system. *Journal of Applied Physics*, 117(17), 2015.

[123] Vanessa G, Parazzini M, Serena F, Ilaria L, and Paolo R. Deep Transcranial Magnetic Stimulation: Modeling of Different Coil Configurations. *IEEE Transactions on Biomedical Engineering*, 63(7):1543–1550, 2016.

[124] Neufeld E. A new planning tool for hyperthermic cancer treatment. *ERCIM News*, 69(3132), 2007.

[125] Li D, Zheng J, Liu Y, Pan C, Kainz W, Yang F, Wu W, and Chen J. An efficient approach to estimate MRI RF field induced in vivo heating for small medical implants. *IEEE Transactions on Electromagnetic Compatibility*, 57(4):643–650, 2015.

[126] Noureddine Y, Bitz AK, Ladd ME, Thürling M, Ladd SC, Schaefers G, and Kraff O. Experience with magnetic resonance imaging of human subjects with passive implants and tattoos at 7 T: a retrospective study. *Magnetic Resonance Materials in Physics, Biology and Medicine*, 28(6):577–590, 2015.

[127] Graessl A, Renz W, Hezel F, Dieringer MA, Winter L, Oezerdem C, Rieger J, Kellman P, Santoro D, Lindel TD, Frauenrath T, Pfeiffer H,

and Niendorf T. Modular 32-channel transceiver coil array for cardiac MRI at 7.0T. *Magnetic Resonance in Medicine*, 72(1):276–290, 2014.

[128] Hoffmann J, Shajan G, Scheffler K, and Pohmann R. Numerical and experimental evaluation of RF shimming in the human brain at 9.4 T using a dual-row transmit array. *Magma (New York, N.Y.)*, 27(5):373–386, 2014.

[129] Johst S, Maderwald S, Fischer A, Quick HH, Ladd ME, and Orzada S. Investigation of the saturation pulse artifact in non-enhanced MR angiography of the lower extremity arteries at 7 Tesla. *PLoS ONE*, 10(3):1–16, 2015.

[130] Neufeld E, Fuetterer M, Murbach M, and Kuster N. Rapid method for thermal dose-based safety supervision during MR scans. *Bioelectromagnetics*, 36:398–407, 2015.

[131] Gosselin MC, Neufeld E, Moser H, Huber E, Farcito S, Gerber L, Jedensjö M, Hilber I, Gennaro FD, Lloyd B, Cherubini E, Szczerba D, Kainz W, and Kuster N. Development of a new generation of high-resolution anatomical models for medical device evaluation: the Virtual Population 3.0. *Physics in Medicine and Biology*, 59(18):5287–5303, 2014.

[132] Cherubini E, Chavannes N, and Kuster N. Realistic skeleton based deformation of high-resolution anatomical human models for electromagnetic simulations. In *The 31st Annual Meeting of the Bioelectromagnetic Society*, 2009.

[133] Lloyd B, Cherubini E, Farcito S, Neufeld E, Baumgartner C, and Kuster N. Covering population variability: Morphing of computation anatomical models. In *International Workshop on Simulation and Synthesis in Medical Imaging*, pages 13–22. Springer, 2016.

[134] Capstick M, McRobbie D, Hand J, Christ A, Kuehn S, Mild KH, Cabot E, Li Y, Melzer A, Papadaki A, Pruessmann KP, Quest R, Rea M, Ryf S, Oberle M, and Kuster N. An investigation into occupational exposure to electromagnetic fields for personal working with

and around medical magnetic resonance imaging equipment. Technical report, IT'IS Foundation for Research on Information Technologies in Society, 2008.

[135] Siemens. https://usa.healthcare.siemens.com/magnetic-resonance-imaging/0-35-to-1-5t-mri-scanner/magnetom-espree/features.

[136] Lucano E, Liberti M, Mendoza GG, Lloyd T, Iacono M, Apollonio F, Wedan S, Kainz W, and Angelone LM. Assessing the electromagnetic fields generated by a radiofrequency MRI body coil at 64 MHz: defeaturing versus accuracy. *IEEE Transactions on Biomedical Engineering*, 63(8):1591–1601, 2016.

[137] Hasgall P, Neufeld E, Gosselin MC, Klingenböck A, and Kuster N. IT'IS database for thermal and electromagnetic parameters of biological tissues, 2015.

[138] IEEE. *IEEE Standard C95.3 Recommended Practice for Measurements and Computations of Radio Frequency Electromagnetic Fields With Respect to Human Exposure to Such Fields, 100 kHz–300 GHz.* The Institute of Electrical and Electronics Engineers, Inc., New York, 1991.

[139] Duchon C. Lanczos filtering in one and two dimensions. *Journal of Applied Meteorology*, 18:1016–1022, 1979.

[140] Pisa S, Cavagnaro M, and Lin JC. The influence of averaging schemes and exposure duration on the correlation between temperature elevation and RF power obsorption metrics in MRI scans. *IEEE Microwave Magzine*, 2016.

[141] IT'IS. https://itis.swiss/virtual-population/explib/overview/.

[142] Yao A, Zastrow E, and Kuster N. Standardized, validated and effective safety assessment of patients with medical implants under MRI exposure using a comprehensive data library combined with an analytics toolset. *In Proceedings of* 27^{th} *International Society for Magnetic Resonance in Medicine (ISMRM) Annual Meeting*, 2019.

[143] https://europe.medtronic.com/content/dam/medtronic-com/xd-en/hcp/documents/surescan

[144] Homann H, Graesslin I, Eggers H, Nehrke K, Vernickel P, Katscher U, Doessel O, and Boernert P. Local SAR management by RF shimming: a simulation study with multiple human body models. *Magnetic Resonance Materials in Physics, Biology and Medicine*, 25(3):193–204, 2012.

[145] Yao A, Zastrow E, Neufeld E, and Kuster N. Efficient and reliable assessment of the maximum local tissue temperature increase at the electrodes of medical implants under MRI exposure. *Bioelctromagnetics*, 40(6):422–433, 2019.

[146] Nadobny J, Szimtenings M, Diehl D, Stetter E, Brinker G, and Wust P. Evaluation of MR-induced hot spots for different temporal SAR modes using a time-dependent temperature gradient treatment. *IEEE Transactions on Biomedical Engineering*, 54(10):1837–1850, 2007.

[147] Wang Z, Lin JC, Mao W, Liu W, Smith MB, and Collins C. SAR and temperature: simulations and comparison to regulatory limits for MRI. *Journal of Magnetic Resonance Imaging*, 26(2):437–441, 2007.

[148] Bernardi P, Cavagnaro M, Pisa S, and Piuzzi E. Specific absorption rate and temperature elevation in a subject exposed in the far-field of radio-frequency sources operating in the 10-900 MHz range. *IEEE Transactions on Biomedical Engineering*, 50(3):295–304, 2003.

[149] Riu PJ and Foster KR. Heating of tissue by near-field exposure to a dipole: A model analysis. *IEEE Transactions on Biomedical Engineering*, 46(8):911–917, 1999.

[150] Pisa S, Calcagnini G, Cavagnaro M, Piuzzi E, Mattei E, and Bernardi P. A study of the interaction between implanted pacemakers and the radiofrequency field produced by magnetic resonance imaging apparatus. *IEEE Transactions on Electromagnetic Compatibility*, 50(1):35–42, 2008.

[151] Mattei E, Calcagnini G, Censi F, Triventi M, and Bartolini P. Role of the lead structure in MRI-induced heating: In vitro measurements on 30 commercial pacemaker/defibrillator leads. *Magnetic Resonance in Medicine*, 67(4):925–935, 2011.

[152] Ho HS. Safety of metallic implants in magnetic resonance imaging. *Journal of Magnetic Resonance Imaging*, 14:472–477, 2001.

[153] Feng S, Qiang R, Kainz W, and Chen J. A technique to evaluate mri-induced electric fields at the ends of practical implanted lead. *IEEE Transactions on Microwave Theory and Techniques*, 63(1):305–313, 2015.

[154] Pennes HH. Analy of tissue and arterial blood temperatures in the resting human forearm. *Journal of Applied Physiology*, 1:93–122, 1948.

[155] Wesley L. Solutions of the bio-heat transfer equation. *Physics in Medicine and Biology*, 33:785–792, 1988.

[156] Gao B, Langer S, and Corry PM. Applications of the time-dependent green's function and fourier transforms of the solution of the bioheat equation. *Int. J. Hyperthermia*, 11:267–285, 1995.

[157] Yeung CJ, Susil RC, and Atalar E. Rf heating due to conductive wire during mri depends on the phase distribution of the transmit field. *Magnetic Resonance in Medicine*, 2002.

[158] IT'IS. https://itis.swiss/virtual-population/virtual-population/overview/.

[159] ZMT. https://zmt.swiss/validation-hw/mits-systems/mits1-5/.

[160] ZMT. https://zmt.swiss/validation-hw/mits-systems/mits3-0/.

[161] Courant R, Friendrichs K, and Lewy H. On the partial difference equations of mathematical physics. *IBM Journal of Research and Development*, 11(2):215–234, 1928.

[162] Nitz WR, Oppelt a, Renz W, Manke C, Lenhart M, and Link J. On the heating of linear conductive structures as guide wires and catheters in interventional MRI. *Journal of magnetic resonance imaging : JMRI*, 13(1):105–14, 2001.

[163] Ladd M, Quick H, Boesinger P, and McKinnon G. Rf heating of actively visualized catheters and guidewires. In *In Proceedings of the ISMRM, Sydney.*, 1998.

[164] Taylor C, B.N. & Kuyatt. Guidelines for evaluating and expressing the uncertainty of nist measurement results. techreport,. Technical report, National Institute of Standards and Technology, Washington, DC, USA, 1994.

Curriculum Vitae

Personal Information

• **Name**	Aiping Yao
• **Date of birth**	August 20th, 1988
• **Nationality**	China
• **email**	yao@itis.swiss

Education

- Ph.D (2015-2019)
  ETH Zurich, Switzerland
  Thesis topic: Novel methods and instrumentations for scientifically sound assessment of MR safety of medical implants.
  GPA: 5.1/6

- Master of Electronic and Communication Engineering (2010-2013)
  Chinese academy of science, China
  Thesis topic: Design and application of low-frequency, low-noise, and low-power medical chip.
  GPA: 3.2/4 (Ranking 3/69)

- Bachelor of Biomedical Engineering (2006-2010)
  Central South University, China
  Thesis topic: Nine-axis motion information monitoring system based on body sensor network.
  GPA: 3.4/4 (Ranking 3/60)

Working Experience

- **Macronix (Su Zhou) Co., Limited (2013-2014)**
  Senior Engineering
  Responsibility: Designing high voltage circuit block in flash memory chip.